Understanding the Electronic Structure and Electron Transfer Kinetics of Titanium Dioxide Photoanodes and Analyzing Parameters Affecting Flatband Potentials in Metal Oxides

By
Milan Patel

Senior Honors Thesis
Department of Chemistry
University of North Carolina at Chapel Hill

April 9th 2021

Approved:

_____

Jillian Dempsey, Thesis Advisor
Anna Curtis, Reader
Michel Gagne, Reader

Acknowledgements

I would like to start by thanking everyone in the Dempsey group for creating such a welcoming and inclusive environment. Everyone has continued to be supportive both inside and outside of the lab, even though much of my time in the group was hindered by the pandemic. Whenever I step into the lab, I feel comfort in knowing that anyone there would be willing to help me when I needed assistance. I also want to thank Dr. Jillian Dempsey for being an amazing research advisor and PI. Jillian continued to push me towards my full potential and always believed in my abilities, and in taking me into her lab she has truly shaped my future plans and aspirations. Most importantly, I'd like to thank Michael Mortelliti, who has been an amazing mentor to me over the past two years. Michael has been an instrumental part of my research and it would not have come to fruition without him. His continued support and guidance have helped me persevere through my undergraduate research career, and I could not have asked for a better mentor. I'd also like to thank my family and friends for all their support over the past several years and for continuing to push me to be the best I can be.

This material is based upon work supported by the Alliance for Molecular PhotoElectrode Design for Solar Fuels (AMPED), an Energy Frontier Research Center (EFRC) funded by the US Department of Energy, Office of Science, Office of Basic Energy Sciences under Award Number DE-SC0001011.

This project was supported by the Sarah Steele Danhoff Undergraduate Research Fund administered by Honors Carolina.

Table of Contents

Understanding the Electronic Structure and Electron Transfer Kinetics of Titanium Dioxide Photoanodes for Applications in Photoelectrosynthesis Cells

1.1 Introduction

As global energy consumption continues to grow and the threats of climate change urge the transition towards renewable energy sources, solar energy has emerged as a promising energy source. Every day, our Earth receives enough sunlight to power human activities for an entire year.[1] However, our current energy systems necessitate a way to store solar energy for it to displace current methods of power generation. Dye-sensitized photoelectrosynthesis cells (DSPECs) offer a way of converting sunlight into chemical energy through the synthesis of solar fuels, which act as a medium for storing solar energy. DSPECs are designed to mimic the natural process of photosynthesis by oxidizing water at a photoanode to produce O_2 and reducing either protons or carbon dioxide at a photocathode to produce fuels like H_2 or methanol.[2] The photoanode is often composed of a metal oxide semiconductor deposited onto a transparent conducting oxide (TCO). The metal oxide is functionalized with a chromophore-catalyst assembly, in which the chromophore absorbs light to drive subsequent electron injection into the metal oxide and the catalyst interacts with the oxidized chromophore to drive water oxidation.[2] Despite the vast amount of research done on the topic thus far, many aspects of DSPECs need to be optimized before they can be implemented on a significant scale.

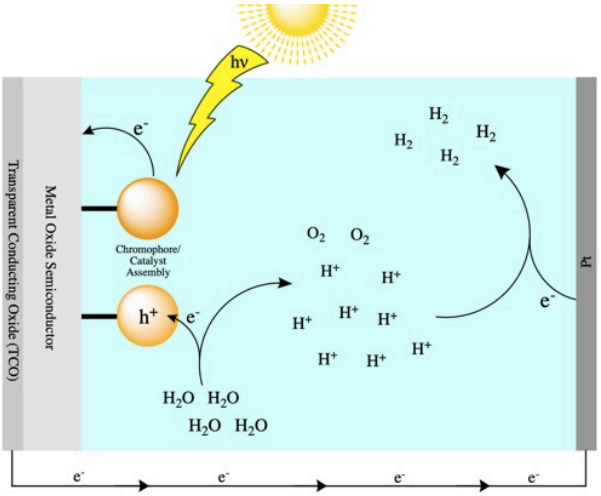

Example schematic for a DSPEC using a photoanode for hydrogen evolution.

A promising metal oxide semiconductor for DSPECs is rutile titanium dioxide (TiO_2).[3] TiO_2 exists primarily in either the rutile or anatase crystal phases, though the anatase phase has been more extensively studied than rutile. In metal oxide photoanodes like those made of TiO_2, one efficiency-limiting process is back-electron transfer (BET). BET is the process in which

electrons injected into the metal oxide semiconductor from the dye are not collected by the TCO but rather return to the oxidized dye, catalyst, or other oxidized species in solution, preventing the buildup of redox equivalents needed to drive water oxidation. One recent development shown to increase DSPEC efficiency and minimize BET is the use of core-shell nanomaterials, where the metal oxide materials are coated with a thin layer of another metal oxide for use as a photoanode.[2,4] Interestingly, even a thin TiO_2 shell deposited onto a TiO_2 core through a chemical bath treatment with $TiCl_4$ results in improved device efficiency and slower BET.[5] Despite the increased popularity of this technique, the mechanisms by which the rate of BET is decreased and the efficiency is increased are still debated.[6,7]

Through the analysis of rutile TiO_2 nanorods by electrochemical, photoelectrochemical, and spectroscopic methods, we shed light on the electronic structure of rutile TiO_2 and factors that impact charge recombination and its potential use in DSPECs. Anatase is similarly studied as a point of comparison for rutile TiO_2 nanomaterials. Through multiple electrochemical techniques, we demonstrate that nanoparticulate films of rutile TiO_2 possess a population of monoenergetic deep trap states, a collection of electronic states that fall between the conduction and valence bands of the semiconductor that are independent from the exponential distribution of shallow trap states tailing from the conduction band. Furthermore, core-shell materials with rutile TiO_2 cores were synthesized and studied to probe the effects of metal oxide shells on the electronic structure of rutile TiO_2 and its deep trap states. Finally, photoelectrochemical impedance spectroscopy was performed to gain an understanding of the BET rate constants of rutile TiO_2 and how these rates are affected by metal oxide shells and by the presence of deep trap states.

1.2 Methods

1.2.1. Synthesis of Rutile TiO_2 Nanorods

Rutile TiO_2 nanorods were synthesized by an aqueous reaction with titanium(IV) tetrachloride ($TiCl_4$). $TiCl_4$ (Sigma Aldrich, 99.9%) was added dropwise to an Erlenmeyer flask containing H_2O cooled by an ice bath while under constant stirring, creating a 2M $TiCl_4$ solution. The solution was then diluted to 0.5M $TiCl_4$ in H_2O and stirred at room temperature in the dark for 7 days. The solution was left to settle for 3 hours and the supernatant was decanted. The white solid precipitate was dispersed in H_2O, centrifuged, and then the supernatant was removed. The

precipitate was then dispersed in ethanol, sonicated in an ice bath, and dried with a rotary evaporator. This process was repeated once more with ethanol. The powder was then dispersed in MilliQ H_2O to achieve a 10 wt% TiO_2 solution. While rapidly stirring, hydroxypropylcellulose (Sigma-Aldrich, MW ~ 80,000 Da, M_n ~ 10,000, powder, 20 mesh particle size) was added to achieve 10 wt% polymer and form the rutile TiO_2 paste. Analysis by transmission electron microscopy (TEM) showed the nanoparticles had an average length of 60 ± 23 nm averaged over 352 measurements. To prepare the photoanodes, the rutile TiO_2 paste was doctor-bladed onto fluorine-doped tin oxide (FTO) coated glass plates using Scotch tape as a spacer. The samples were sintered in a box oven at 100˚C for 10 minutes (150˚C/hr ramp up) followed by 500˚C for 1 hour (225˚C/hr ramp up). The film thickness for rutile TiO_2 slides was 5.0 ± 0.5 μm. The rutile crystalline phase was confirmed using Raman spectroscopy and powder X-ray diffraction.

1.2.2. Atomic Layer Deposition

Atomic layer deposition (ALD) was used to coat rutile TiO_2 nanocrystals with either titanium oxide, zinc oxide, aluminum oxide, or zirconium oxide shells using an Ultratech/Cambridge NanoTech Savannah S200 system. Gas flows and timings were controlled with a LabVIEW sequencer, and molecular precursors were housed in stainless steel cylinders attached to the ALD. Ultrahigh purity N_2 (Airgas, 99.999%) was used as the carrier gas, ultrapure DI H_2O was used as the oxygen precursor, and tetrakis(dimethylamido)titanium TDMA-Ti was used as the titanium precursor. The TDMA-Ti was heated at 75˚C for one hour prior to running ALD experiments, and the reactor chamber was held at 150˚C. For titanium oxide growth, the following ALD recipe was used: 10 min purge at 20 sccm N_2, [0.5 s pulse TDMAT, 30 s exposure, 60 s purge of N_2 at 20 sccm, 0.02 s pulse H_2O, 30 s exposure, 60 s purge of N_2 at 20 sccm] x n cycles. Following ALD, samples were sintered in a box oven at 500˚C for 1 hour (225˚C/hr ramp up). Samples will be named herein as $rTiO_2/nTiO_x$ where n denotes the number of ALD cycles for that sample. Using a similar procedure, other shell materials were also deposited onto rutile TiO_2. Zirconium dioxide (ZrO_2) shells were deposited using TDMA-Zr precursor preheated at 75˚C for one hour. Zinc oxide (ZnO) shells were deposited using diethyl zinc $Zn(Et)_2$ precursor and required no preheating. Aluminum oxide (Al_2O_3) shells were deposited using trimethyl aluminum $Al(Me)_3$ precursor and required no preheating.

1.2.3. Electrochemical Experiment Setup

Cyclic voltammetry, chronoamperometry, and spectroelectrochemistry were performed using a Pine Instruments WaveDriver 10 Potentiostat. Electrochemical impedance spectroscopy (EIS) was performed using a Gamry Instruments Reference 600 Potentiostat/Galvanostat/ZRA. The working electrode consisted of the prepared rutile TiO_2 on FTO-glass with an exposed sample area of 0.12 cm^2. The reference was a Ag/AgCl (3M NaCl, CH Instruments) electrode and the counter electrode was a platinum wire. The supporting electrolyte was a 0.1M $HClO_4$ aqueous solution. The solution was sparged with Ar (Airgas, industrial grade) prior to performing measurements. Cyclic voltammetry, chronoamperometry, and EIS were performed in the dark. For spectroelectrochemical experiments, an Agilent Cary 60 UV-vis spectrophotometer was used to measure absorbance in a 1-cm path length quartz cuvette and the exposed sample area was 1 cm^2.

1.2.4. Photoelectrochemical Experiment Setup

Photoelectrochemical impedance spectroscopy (PEIS) was performed using a Gamry Instruments Reference 600 Potentiostat/Galvanostat/ZRA. The light source was a 514 nm LED (Lumencor SPECTRA X light engine). Prior to PEIS experiments, the rutile TiO_2 on FTO slides were soaked in methanol containing $[Ru(2\text{-}2'\text{-bipyridine})_2(4,4'\text{-}(PO_3H_2)_2\text{-}2,2'\text{-bipyridine})]^{2+}$ (RuP) to dye-load the sample. The working electrode consisted of the prepared slide with an exposed sample area of 0.8 cm^2 and copper tape connecting the FTO to the electrical lead. The reference was a Ag/AgCl (3M NaCl, CH Instruments) electrode and the counter electrode was a platinum wire. For galvanostatic experiments, the solution was a pH 4.7 acetate buffer with 0.1M $NaClO_4$ supporting electrolyte and 3mM hydroquinone added as a quencher. For potentiostatic experiments, the solution was a 0.1M $HClO_4$ aqueous electrolyte. The solution was sparged with Ar (Airgas, industrial grade) prior to performing measurements.

1.2.5. Diffuse Reflectance Spectroscopy

Diffuse reflectance spectra of the metal oxide films were acquired on an Agilent Cary 5000 UV-Vis-NIR spectrophotometer with the external diffuse reflectance accessory (DRA). Slides were placed in the center position of the external DRA and positioned at a 10˚ angle to incident light. Spectra were recorded from 350-650 nm, and background scans of FTO-glass were subtracted out from sample scans.

1.3 Results and Discussion

1.3.1. Synthesis and Characterization of Rutile TiO_2

Rutile TiO_2 was synthesized by hydrolyzing $TiCl_4$ in an excess of water and letting the solution to stir for 7 days, allowing for rutile TiO_2 nanostructures to form. The resulting particles were isolated and then mixed with water and hydroxypropylcellulose to form a paste. This paste was doctor-bladed onto FTO-glass sheets and heat treated to create the rutile TiO_2 nanoparticle thin films. The morphology of synthesized rutile TiO_2 nanoparticles was studied using TEM. TEM images are shown in Figure 1 and depict the TiO_2 as having a nanorod structure. The distribution of nanorod lengths is shown in Figure 1 as well, and the average nanorod length was 60 ± 23 nm.

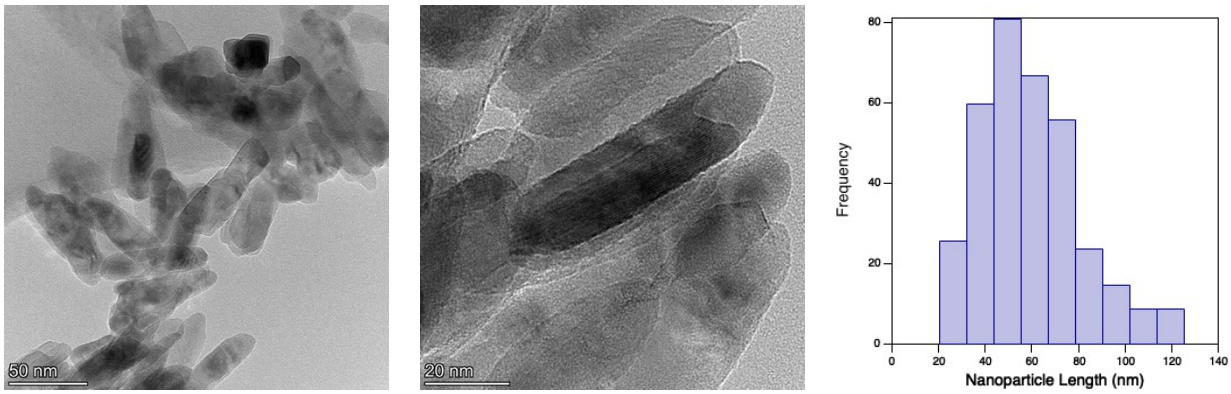

Figure 1. TEM images of the synthesized rutile TiO_2 nanorods, and a histogram showing the distribution of nanoparticle lengths with an average length of 60 ± 23 nm averaged over 352 measurements.

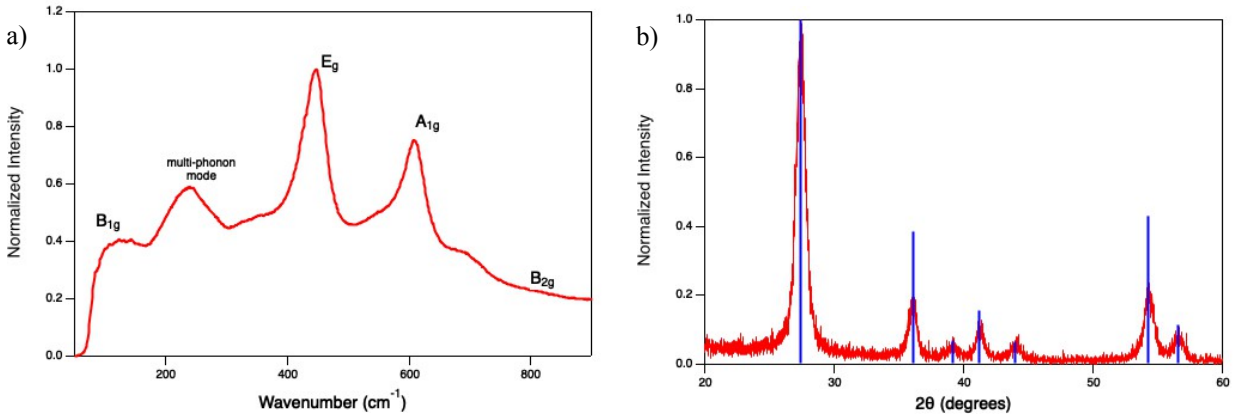

Figure 2. (a) Raman spectrum of the rutile TiO_2 nanorods with the rutile vibrational modes assigned, and (b) a powder XRD spectrum of the rutile TiO_2 nanorods with the powder diffraction file values shown with the blue lines.

To confirm the crystalline phases of the samples, both Raman spectroscopy and powder X-ray diffraction (XRD) were used. The Raman spectrum in Figure 2a has distinct peaks for the major vibrational modes of rutile TiO_2 and show no signs of other phases like anatase. Similarly, the XRD spectrum in Figure 2b has clear peaks matching closely with the powder diffraction file (PDF) of rutile TiO_2.

1.3.2. Quantification of Deep Trap States in Rutile TiO_2

Cyclic voltammetry was performed on rutile TiO_2 nanorod films (Figure 3a). The main feature of the cathodic trace is the increasing current corresponding to the reduction of an exponential distribution of trap states extending from the conduction band edge. This feature is consistent with previous observations for both anatase and rutile TiO_2 nanomaterials.[8] The presence of an increase in the density of states is indicated by the bump in the cathodic sweep of the cyclic voltammogram occurring around –50 mV vs Ag/AgCl. This corresponds to deep trap states, a collection of electronic states that fall between the conduction and valence bands of the semiconductor that are independent from the exponential distribution of shallow trap states tailing from the conduction band. The deep trap state potential is consistent between multiple repetitions of cyclic voltammograms and across multiple samples. Chronoamperometry was also performed on rutile TiO_2 nanorod films. The current–time curves produced from the chronoamperometry experiment were integrated and used to calculate the capacitance of the film at different potentials. The resulting capacitance data is shown in figure 3b and shows the electronic states for rutile TiO_2. This distribution of states was fit to two functions, an exponential representative of the exponential distribution of shallow trap states tailing below the conduction band of TiO_2, and a Gaussian distribution which models the monoenergetic collection of deep trap states in rutile TiO_2. As seen in Figure 3b, the sum of these two distributions fit the data well. In addition, the Gaussian is centered at –70 mV vs Ag/AgCl, in close agreement with the location of the deep trap states in the cyclic voltammogram. For comparison, the cyclic voltammogram and capacitance from chronoamperometry for anatase TiO_2 nanoparticles are shown in Figure 4. There are no apparent deep trap states from the cyclic voltammogram in Figure 4a, and the capacitance data in Figure 4b fits well to an exponential curve. From this, it is apparent that the deep trap states are unique to the rutile form of TiO_2.

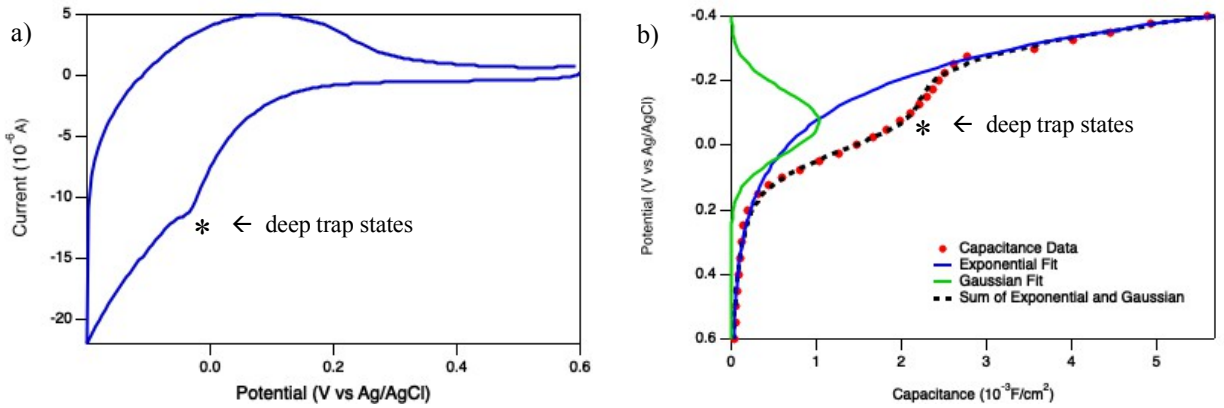

Figure 3. (a) Cyclic voltammogram of rutile TiO_2 nanorods performed in 0.1M $HClO_4$ at a scan rate of 20 mV/s with an exposed surface area of 0.12 cm^2, and (b) capacitance of rutile TiO_2 collected from a chronoamperometry experiment performed in 0.1M $HClO_4$ with the data fit to the sum of an exponential and a Gaussian curve.

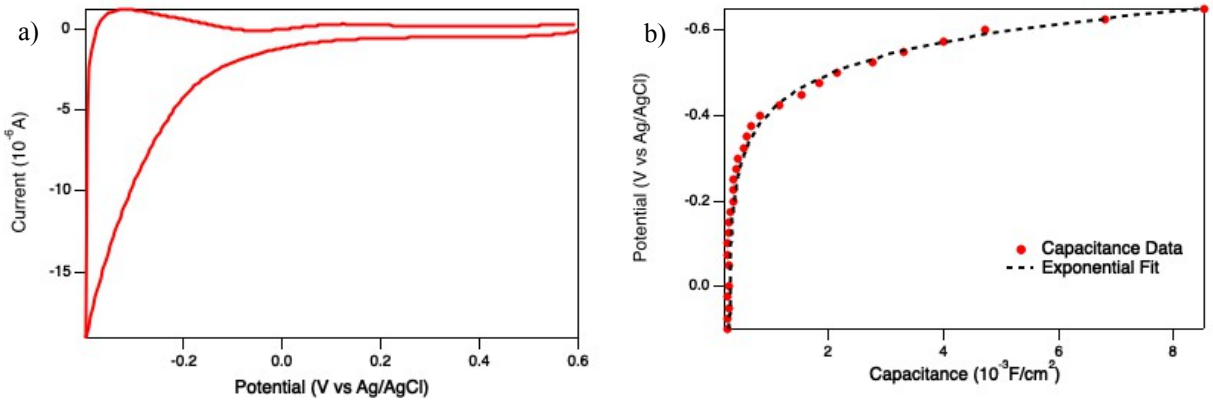

Figure 4. (a) Cyclic voltammogram of anatase TiO_2 nanoparticles performed in 0.1M $HClO_4$ at a scan rate of 20 mV/s with an exposed surface area of 0.12 cm^2, and (b) capacitance of anatase TiO_2 collected from a chronoamperometry experiment performed in 0.1M $HClO_4$ with the data fit to an exponential curve.

Electrochemical impedance spectroscopy (EIS) was also used to study rutile TiO_2 nanorod films. EIS is an AC technique, where the applied current (in galvanostatic mode) or applied voltage (in potentiostatic mode) is modulated at a set frequency and the impedance response is measured. This technique is further explained in section 1.3.3. EIS data was collected under potentiostatic mode at multiple potentials, and the resulting data was fit to the model circuit shown in Figure 5a. The circuit consists of a solution resistance component and two RC circuits, representing the electrolyte-TiO_2 interface and the TiO_2-FTO interface. Constant phase elements (CPEs) are being used in place of capacitors to better account for non-ideal capacitance caused by inhomogeneities on the surface of metal oxide electrodes.[9] From the circuit fitting, the capacitance was calculated

at each potential that a measurement was made and is plotted in figure 5b. From the EIS data, the deep trap states appear at a potential of –100 mV vs Ag/AgCl.

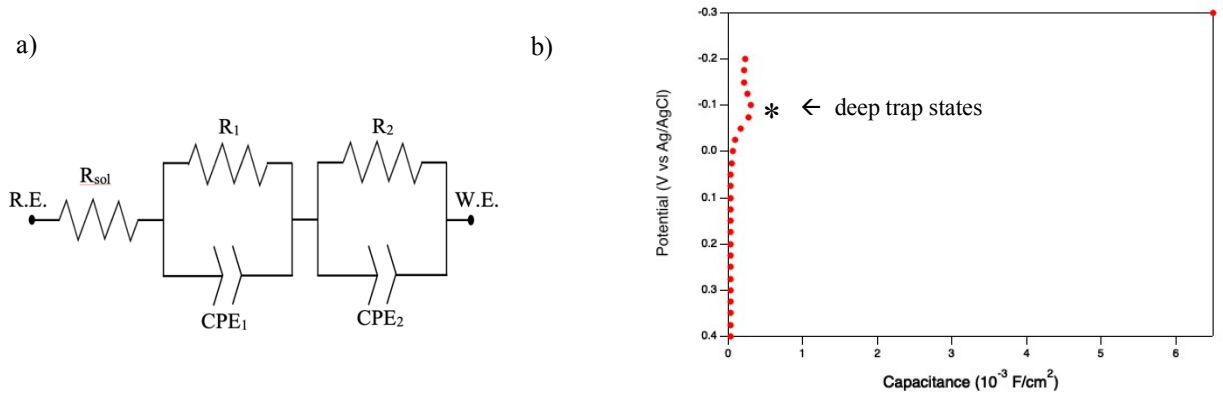

Figure 5. (a) A double Randles circuit in which R_{sol} is the solution resistance, R_1 and R_2 are the charge transfer resistances at the electrolyte-TiO_2 and TiO_2-FTO interfaces, respectively, CPE_1 and CPE_2 are the non-ideal capacitances at the electrolyte-TiO_2 and TiO_2-FTO interfaces, respectively, R.E. is the reference electrode, and W.E. is the working electrode, (b) capacitance of rutile TiO_2 collected from an EIS experiment performed in 0.1M $HClO_4$ and a potential perturbation of 10 mV over a frequency range from 100 kHz to 0.1 Hz.

Collectively, these potentiostatic (chronoamperometry), potentiodynamic (cyclic voltammetry), and alternating potential (EIS) techniques all confirm the presence of deep trap states in rutile TiO2 nanorod thin films. Moreover, the energetics of these deep trap states are consistently quantified as lying between –50 and –100 mV vs Ag/AgCl.

Spectroelectrochemical experiments were performed to help elucidate the electronic state distribution in rutile TiO_2 samples. In a spectroelectrochemical experiment, the rutile TiO_2 electrode was held at a certain potential and the change in absorbance relative to the baseline absorbance (an unbiased rutile TiO_2 electrode) was recorded. The absorbance data for this experiment is shown in Figure 6a. The broad absorption increase seen across the visible region could correspond to electrons populating the trap states, which can be excited into the conduction band with lower energy light. The absorption bleach below 450 nm is likely due to the decreased fundamental absorption as conduction band states are being filled at more negative potentials. As shown in figure 6b, the absorbance curves are normalizable, suggesting that only one type of reduction is at play during the experiment (e.g. a Ti^{4+} to Ti^{3+} reduction). The absorption curves can be modeled to a single exponential function[6]:

$$A(\lambda, E) = a(\lambda)e^{-bE} \quad (eq\ 1)$$

where E is the applied potential, λ is the wavelength, and b is a solvent-dependent constant. The fits are shown in Figure 6a with black dashed lines.

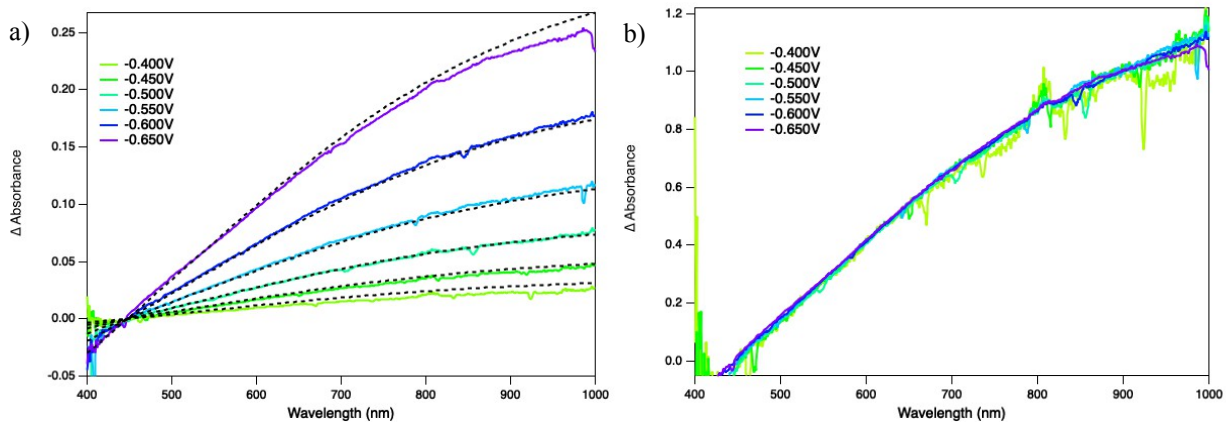

Figure 6. (a) Spectroelectrochemical data on the change in absorbance of rutile TiO_2 nanorod films as the applied potential increases negatively, experiment performed in 0.1M $HClO_4$ with an exposed surface area of 1 cm^2, slide held at each potential to equilibrate for 3 minutes before absorbance measurements were taken, curve fits shown in black dashed lines, (b) data from figure a normalized at 900 nm.

Being able to fit the absorbance change to a single exponential suggests a single reduction event, despite two distinct states being identified through the cyclic voltammetry, chronoamperometry, and EIS experiments described above. There are several possible ways to reconcile these conflicting findings. It could be possible that electrons in the deep trap states are in rapid thermal equilibrium with the electronic states in the exponential conduction band tail, so the two states show up as one absorption change in the spectroelectrochemistry experiment. It is also possible that the reduction of the deep trap states is spectroscopically silent. Another explanation is that absorption changes brought on by reduction of conduction band tail states are much larger than absorption changes from reducing deep trap states, so only one change is noticed in the data. There is no clear and definitive answer as to which of these, if any, explain the reason why only one electronic distribution appears to be present from the spectroelectrochemical data.

To help explain what physical features of the rutile TiO_2 nanorods might be causing the trap state observed above, TiO_2, ZrO_2, Al_2O_3, and ZnO shell materials were used to coat the rutile nanorods using ALD. For metal oxides, trap states are often the result of disruptions in the extended lattice of the material which could be related to vacancies in the lattice or inhomogeneities where

the lattice terminates at the surface. The application of the ALD shells provides relevant information about whether these deep trap states are related to defects on the surface of the nanorod or to some other factor, such as bulk/core defects or grain boundaries. Figure 7 shows the cyclic voltammograms and capacitance data from chronoamperometry for three different core-shell materials: $rTiO_2/3Al_2O_3$, $rTiO_2/5ZnO$, and $rTiO_2/3ZrO_2$, where the number preceding the shell material represents the number of ALD cycles used to deposit the metal oxide shell onto the rutile TiO_2 nanorods.

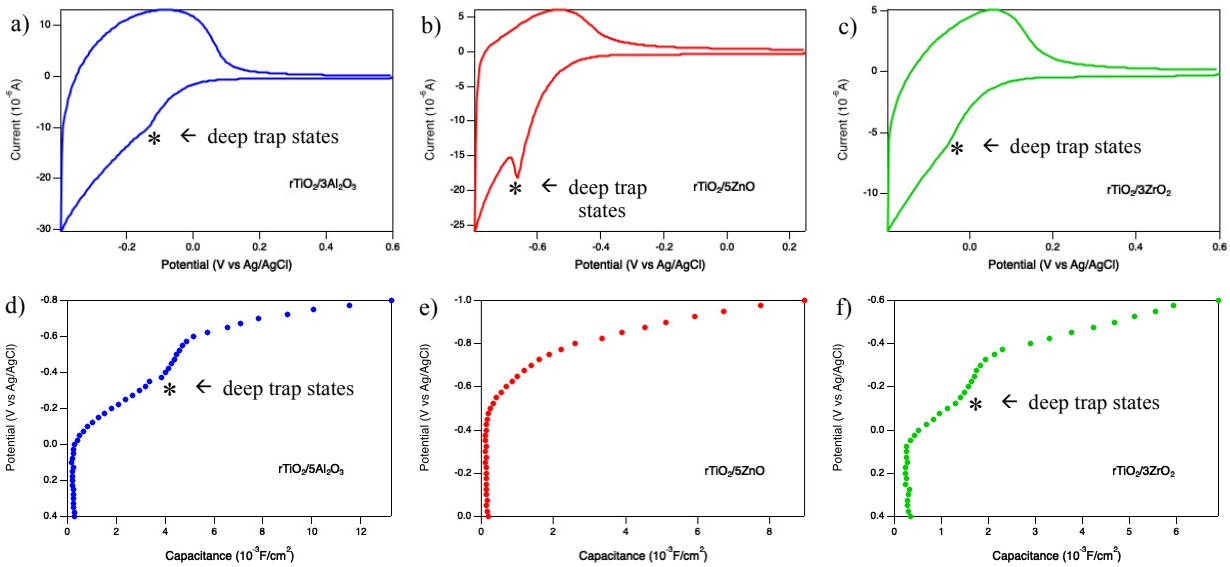

Figure 7. Cyclic voltammograms (a, b, c) of different core-shell materials taken at scan rate of 20 mV/s and with an exposed sample surface area of 0.12 cm^2, and capacitance data (d, e, f) from chronoamperometry experiments; $rTiO_2/3Al_2O_3$ (a, d) and $rTiO_2/3ZrO_2$ (c, f) data collected in 0.1M $HClO_4$, while $rTiO_2/5ZnO$ (b, e) data collected in pH 7 phosphate buffer with 0.1M $NaClO_4$ supporting electrolyte.

From the data in Figure 7, the deep trap states are still present in each of the samples, with visible bumps in the cathodic scans of each cyclic voltammogram. The capacitance data also shows a feature representative of the trap states with the exception of $rTiO_2/5ZnO$ in Figure 7e. It is likely that such a feature would be visible had the data been extended to more negative potentials, since the potential at which the deep trap states appear is generally seen more negative in the capacitance data from chronoamperometry compared to that of cyclic voltammetry. It is important to note that, due to the instability of ZnO in acidic conditions, electrochemical experiments for $rTiO_2/5ZnO$ were performed in pH 7 solutions, so electrochemical features show up at more negative potentials compared to experiments in pH 1 solutions.

Collectively, these core-shell experiments indicate that surface treatment of the rutile TiO_2 nanorods does not passivate the deep trap states, as would be expected if the trap states were associated with defects or inhomogeneities on the surface of the particles. Rather, it is more likely that the deep trap states are located at the grain boundaries[10] between rutile TiO_2 nanorods in contact with each other in the film, as these could not be passivated by an ALD coating.

1.3.3. $rTiO_2/nTiO_x$ Core-Shell Material Impacts on Electronic Structure

While the core-shell materials above did not passivate the trap states, the data in Figure 7 shows that they did impact the electronic structure of the TiO_2 nanorods. To more thoroughly study the effects of shell deposition on core material electronic structures, titanium oxide was deposited onto rutile TiO_2 nanorods using ALD to create samples herein referred to as $rTiO_2/nTiO_x$, where n refers to the number of ALD cycles. The $rTiO_2/nTiO_x$ samples serve as parallels to $TiCl_4$-treated TiO_2 previously used to improve device performance and decrease the rate of BET. By using ALD to create $rTiO_2/nTiO_x$ samples, the thickness of the shells can be modulated. Diffuse reflectance spectroscopy was performed on the core shell materials, and Tauc analysis was performed on the absorption spectra. For Tauc analysis, $(\alpha E)^n$ is plotted versus E to create a Tauc plot, where $\alpha = \frac{2.303 * Absorbance}{film\ thickness}$, E is the energy of the absorbance wavelength in eV, and n is 2 and ½ for direct and indirect band gap materials, respectively. Tauc plots are shown in Figure 8a.

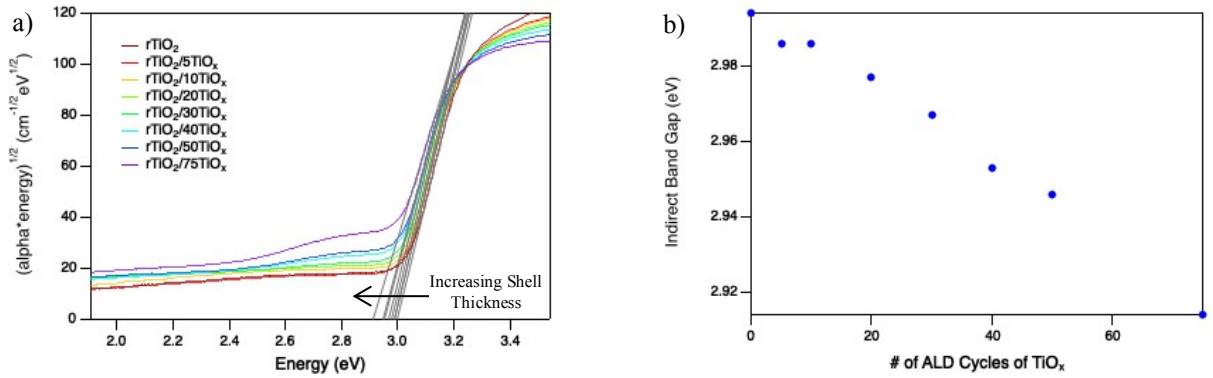

Figure 8. (a) Tauc plots from absorbance of $rTiO_2/nTiO_x$ films collected with diffuse reflectance spectroscopy, and the fits of the linear regions overlaid, (b) the calculated indirect band gaps for $rTiO_2/nTiO_x$ materials as a function of shell thickness.

Extrapolating the linear region of the Tauc plot to the x-intercept provides the band gap of the material. Figure 8b shows the indirect band gaps of the $rTiO_2/nTiO_x$ materials as a function of the

number of ALD cycles, corresponding to the thickness of the TiO_x shells. It is evident from the graph that there is a linear decrease in the band gap of the rutile TiO_2 nanoparticles as the shell thickness of the core-shell material increases. This suggests a change in the position of the conduction band edge and/or valence band edge. Cyclic voltammetry was also performed on the $rTiO_2/nTiO_x$ samples. From the overlaid cyclic voltammograms shown in Figure 9a, it is evident that the deep trap state population is shifting from more negative to more positive potentials as the shell thickness increases.

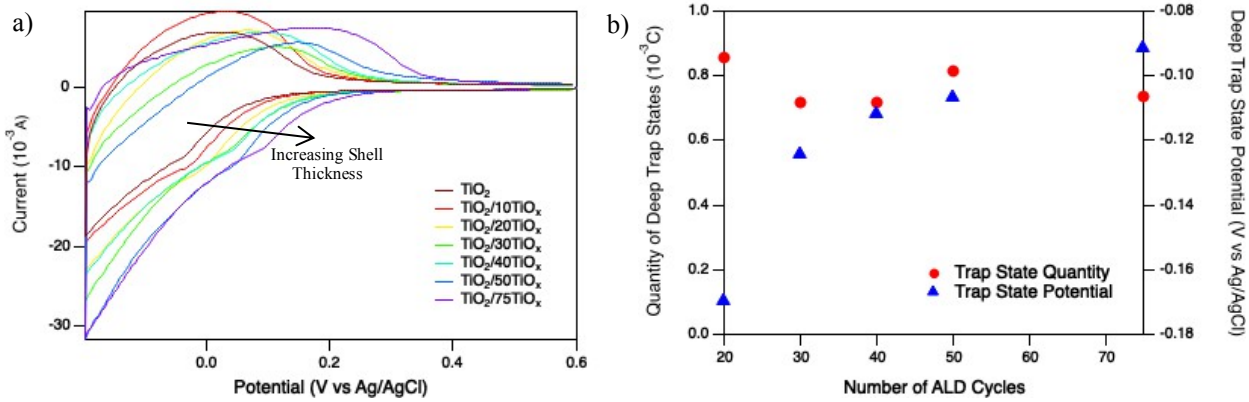

Figure 9. (a) Cyclic voltammograms of $rTiO_2/nTiO_x$ core-shell materials in 0.1M $HClO_4$ at a scan rate of 20 mV/s and with an exposed surface area of 0.12 cm^2, (b) capacitance data from chronoamperometry was fitted to a single exponential and a Gaussian, as done in Figure 3b, where the midpoint of the Gaussian gives the potential of the deep trap states shown above as blue triangles, and the area under the Gaussian gives the quantity of deep trap states shown above as red circles.

Chronoamperometry was also performed on the $rTiO_2/nTiO_x$ samples, from which the capacitance can be determined. The capacitance data showed an exponential increase with decreasing potential, as well as a characteristic bump for the deep trap states, like that seen for bare rutile TiO_2 in Figure 3b. The capacitance data was therefore also fit to the sum of a single exponential and a Gaussian distribution. The Gaussian distribution represents the distribution of deep trap states, so from the Gaussian fitting parameters, the potential at which the deep trap states reside was determined for each $rTiO_2/nTiO_x$ sample. In addition, the quantity of these deep trap states was calculated by determining the area under the Gaussian curve for each sample. The quantity and potential of the deep trap states from fitting the capacitance is shown in Figure 9b. The quantity of deep trap states seems to be consistent across multiple shell thicknesses, whereas the potential at which the deep trap states lie shifts positively as the shell thickness increases. These

data indicate that the addition of a titanium oxide shell onto the rutile TiO_2 nanorods shifts the potential at which the deep trap states are found but does not change the trap state quantity.

1.3.4. Using PEIS to Study the Electron Transfer Kinetics of Rutile TiO_2

Photoelectrochemical impedance spectroscopy (PEIS) was used to study rutile TiO_2 nanorod films and core-shell materials, with anatase TiO_2 also studied for comparison. PEIS is a technique in which either an alternating current (galvanostatic mode) or an alternating potential (potentiostatic mode) is applied and the resulting impedance is measured while the system is exposed to a light source.

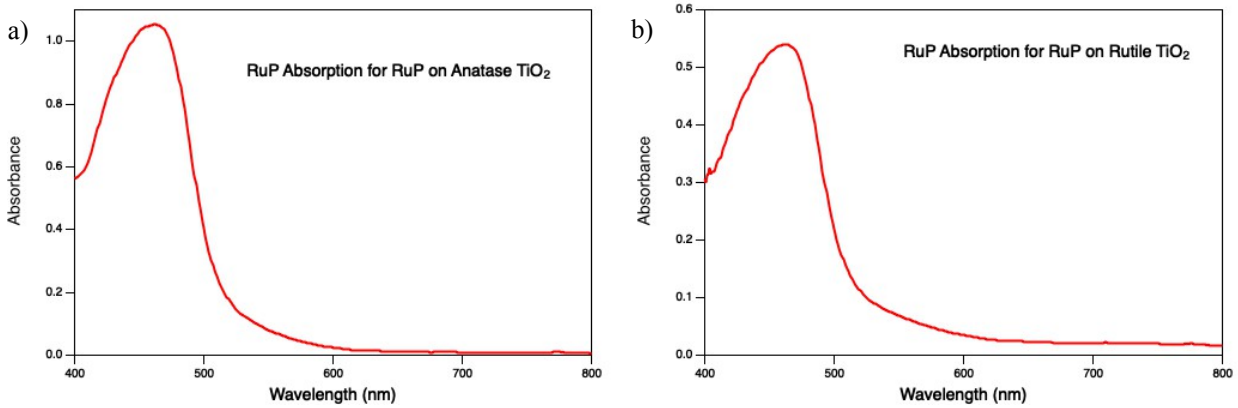

Figure 10. Averaged absorption spectra for RuP loaded onto (a) anatase (6 spectra averaged) and (b) rutile (8 spectra averaged) TiO_2 photoanodes, with the absorbance of the TiO_2 and FTO background-corrected.

Samples studied with PEIS were dye-loaded with RuP. Figure 10 shows the absorbance profiles for RuP dye-loaded onto anatase and rutile TiO_2 photoanodes. The surface coverages for RuP were $7.85 * 10^{-8}$ and $4.02 * 10^{-8}\, mol/cm^2$ for anatase and rutile TiO_2, respectively. Anatase TiO_2 has better dye-loading capacity because the nanoparticles are smaller than those of rutile, so there is a larger surface area in the mesoporous films for the dye to adhere. A 514 nm LED light source was used for the experiments. The 514 nm light is sufficiently energetic to excite the metal-to-ligand charge transfer in RuP, leading to electron injection into the TiO_2 conduction band, but not energetic enough to excite electrons from the TiO_2 valence band into the conduction band. Figure 11 shows an example of data resulting from a galvanostatic PEIS experiment under open circuit potential. Figure 11a shows the Nyquist plot, which plots the imaginary component

of the impedance versus the real component. Figure 11b shows the Bode plot, which plots the impedance (in red) and the phase angle (in blue) as a function of the perturbation frequency.

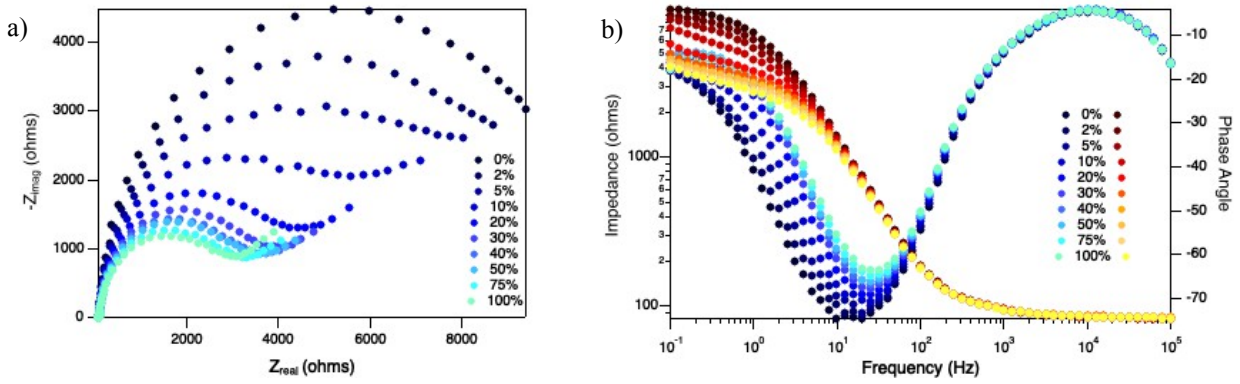

Figure 11. Nyquist plot (a) and Bode plot (b) from a PEIS experiment on rutile TiO_2 nanorods with a RuP dye in pH 4.7 acetate buffer with 0.1M $NaClO_4$ supporting electrolyte and 3mM hydroquinone, with varying light intensity from a 514 nm LED.

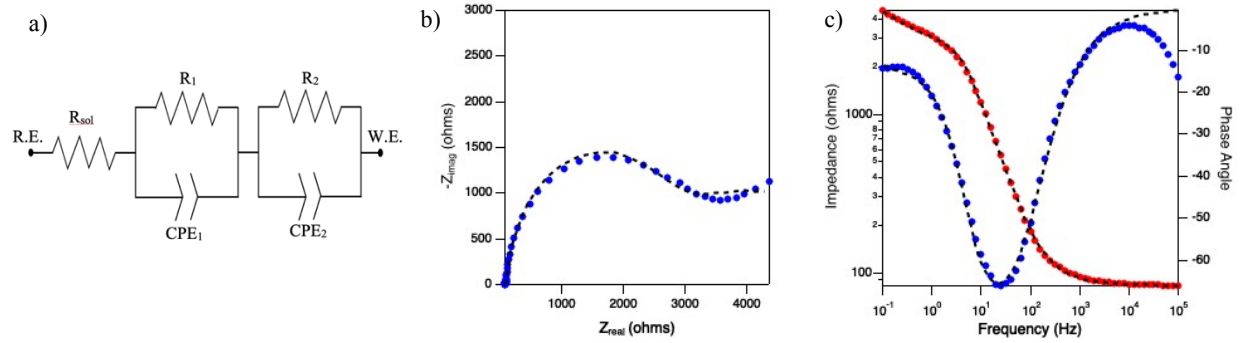

Figure 12. (a) A double Randles circuit in which R_{sol} is the solution resistance, R_1 and R_2 are the charge transfer resistances at the electrolyte-TiO_2 and TiO_2-FTO interfaces, respectively, CPE_1 and CPE_2 are the non-ideal capacitances at the electrolyte-TiO_2 and TiO_2-FTO interfaces, respectively, R.E. is the reference electrode, and W.E. is the working electrode, and a representative Nyquist (b) and Bode (c) plot at 50% light with double Randles circuit fit shown with dashed black line.

The Nyquist and Bode plots can be simultaneously fit to a circuit model in order to extract electrical parameters involved in the system. The circuit used to fit the data is shown in Figure 12a, and examples of the fitting are shown in Figures 12b and 12c. The rate constant for BET is calculated using the values from the circuit fitting. The rate constant is expressed by equation 2:[11]

$$k_{BET} = \frac{1}{R_1 C_1} \qquad C_1 = \frac{(Y_o * R)^{1/\alpha}}{R} \qquad (eq\ 2)$$

where R_1 and C_1 are the resistance and capacitance across the rutile TiO_2-electrolyte interface, and the capacitance is calculated using the fitting parameters for CPEs, Y_0 and α. Using galvanostatic PEIS, the BET rate constants for rutile and anatase TiO_2 were calculated under different light intensity conditions. Increasing the incident light intensity shifts the open circuit potential of the slides negatively due to more electrons being injected into the TiO_2 from the photoexcited RuP. The BET rate constants plotted versus open-circuit potential and versus injected electron concentration are shown in Figure 13. Anatase TiO_2 likely achieves higher injected electron concentrations and more negative open circuit potentials for the same light intensities due to higher dye surface coverage as calculated before. The rate constants for the rutile TiO_2 nanorods at a given open-circuit potential or injected electron concentration are higher than those for anatase TiO_2 nanoparticles, suggesting that rutile TiO_2 would be less efficient as a photoanode. It is difficult to tell from this data alone if this difference in rate constants is related to the fact that the deep trap states are present in rutile TiO_2 nanorods but not anatase TiO_2 nanoparticles.

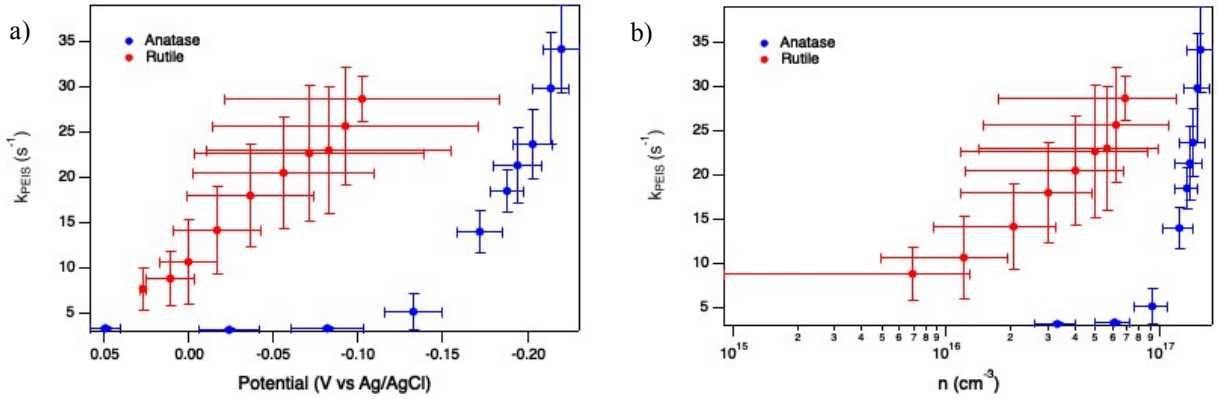

Figure 13. The BET rate constants for anatase (blue) and rutile (red) TiO_2 plotted versus the open-circuit potential (a) and injected electron concentration (b), with the associated error from averaging parameters calculated from repeated PEIS experiments.

The BET rate constants were also calculated for $rTiO_2/nTiO_x$ samples to determine the effects of shell materials on BET. The BET rate constants for rutile TiO_2 and $rTiO_2/30TiO_x$ are shown in Figure 14 plotted against the open circuit potential (14a) and the injected electron concentration (14b). This data shows that back-electron transfer proceeds more slowly when a titanium oxide shell is applied to the rutile TiO_2 nanorods. This concurs with previous studies showing improved efficiency for core-shell materials, since BET is a process that hinders device efficiency.

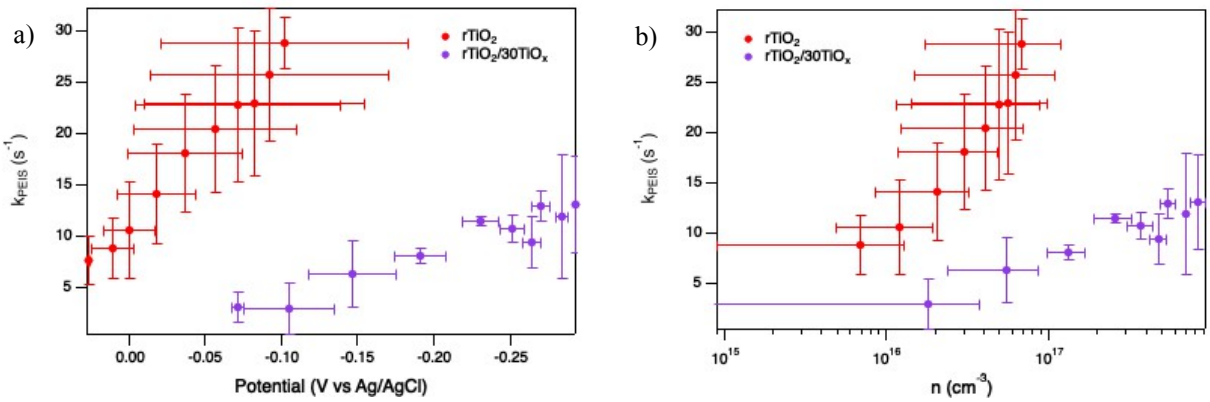

Figure 14. The BET rate constants for anatase (blue) and rutile (red) TiO_2 plotted versus the open-circuit potential (a) and injected electron concentration (b), with the associated error from averaging parameters calculated from repeated PEIS experiments.

1.4 Conclusion

In this project we have demonstrated the presence of a monoenergetic collection of deep trap states in rutile TiO_2 nanorods through a variety of electrochemical techniques and have determined their location to be between –50 and –100 mV vs Ag/AgCl. The deep trap states cannot be passivated by the addition of metal oxide shells, suggesting that the trap states are likely related to electronic states at the grain boundaries in nanorod films. The electronic position of the deep trap states shifted positively with titanium oxide shell deposition, and the band gap decreased as the shell thickness increased, indicating that shell materials alter the electronic structures of metal oxide nanomaterials. The addition of titanium oxide shells also reduced the rate of BET in rutile TiO_2 photoanodes, concurring with data showing improved efficiency for core-shell materials.

1.5 References

(1) Ardo, S.; Meyer, G. J. Photodriven Heterogeneous Charge Transfer with Transition-Metal Compounds Anchored to TiO2 Semiconductor Surfaces. *Chem. Soc. Rev.* **2009**, *38* (1), 115–164.

(2) Ashford, D. L.; Gish, M. K.; Vannucci, A. K.; Brennaman, M. K.; Templeton, J. L.; Papanikolas, J. M.; Meyer, T. J. Molecular Chromophore-Catalyst Assemblies for Solar Fuel Applications. *Chem. Rev.* **2015**, *115* (23), 13006–13049.

(3) Swierk, J. R.; Regan, K. P.; Jiang, J.; Brudvig, G. W.; Schmuttenmaer, C. A. Rutile TiO2

as an Anode Material for Water-Splitting Dye-Sensitized Photoelectrochemical Cells. *ACS Energy Lett.* **2016**, *1* (3), 603–606.

(4) Alibabaei, L.; Sherman, B. D.; Norris, M. R.; Brennaman, M. K.; Meyer, T. J. Visible Photoelectrochemical Water Splitting into H2 and O2 in a Dye-Sensitized Photoelectrosynthesis Cell. *Proc. Natl. Acad. Sci. U. S. A.* **2015**, *112* (19), 5899–5902.

(5) Ahmed, S.; Du Pasquier, A.; Asefa, T.; Birnie, D. P. Improving Microstructured TiO2 Photoanodes for Dye Sensitized Solar Cells by Simple Surface Treatment. *Adv. Energy Mater.* **2011**, *1* (5), 879–887.

(6) James, E. M.; Barr, T. J.; Meyer, G. J. Evidence for an Electronic State at the Interface between the SnO2 Core and the TiO2 Shell in Mesoporous SnO2/TiO2 Thin Films. *ACS Appl. Energy Mater.* **2018**, *1* (2), 859–867.

(7) James, E.; Bennett, M.; Bangle, R. E.; Meyer, G. J. Electron Localization and Transport in SnO2/TiO2 Mesoporous Thin Films: Evidence for a SnO2/SnxTi1-XO2/TiO2 Structure. *Langmuir* **2019**, *35* (39), 12694–12703.

(8) Bisquert, J.; Fabregat-Santiago, F.; Mora-Seró, I.; Garcia-Belmonte, G.; Barea, E. M.; Palomares, E. A Review of Recent Results on Electrochemical Determination of the Density of Electronic States of Nanostructured Metal-Oxide Semiconductors and Organic Hole Conductors. *Inorganica Chim. Acta* **2008**, *361*, 684–698.

(9) Bredar, A. R. C.; Chown, A. L.; Burton, A. R.; Farnum, B. H. Electrochemical Impedance Spectroscopy of Metal Oxide Electrodes for Energy Applications. *ACS Appl. Energy Mater.* **2020**, *3* (1), 66–98.

(10) Berger, T.; Lana-Villarreal, T.; Monllor-Satoca, D.; Gómez, R. An Electrochemical Study on the Nature of Trap States in Nanocrystalline Rutile Thin Films. *J. Phys. Chem. C* **2007**, *111* (27), 9936–9942.

(11) Xu, P.; Gray, C. L.; Xiao, L.; Mallouk, T. E. Charge Recombination with Fractional Reaction Orders in Water-Splitting Dye-Sensitized Photoelectrochemical Cells. *J. Am. Chem. Soc.* **2018**, *140* (37), 11647–11654.

Meta-Analysis of Flatband Potentials for TiO_2, SnO_2, and ZnO in Aqueous Solution: Determining Factors Causing Variation in Reported Flatband Potentials

2.1 Introduction

Metal oxide semiconductors have a wide variety of current and potential future uses, including applications in catalysis and energy conversion systems. As discussed in Chapter 1, metal oxide semiconductors can be used in devices like dye-sensitized photoelectrosynthesis cells (DSPECs) as photoanodes and supports for chromophore-catalyst assemblies for solar fuel generation. One key parameter used to assess metal oxides for their potential application as photoelectrodes is the flatband potential.[1] Flatband potentials are used in a variety of ways in analyzing semiconductors, including analyzing the efficiency of photo-driven processes, calculating kinetic parameters, demarcating the accumulation and depletion zones, and estimating the band edges of new materials.[1,2] For these reasons, it is important to be able to accurately determine the flatband potential for a semiconductor.

From an electrochemical perspective, the flatband potential is the potential one would have to apply to a semiconductor-conductor or semiconductor-electrolyte interface such that there is no potential drop between the surface and bulk of the semiconductor.[3] In the absence of a potential bias, when a metal oxide semiconductor is put into contact with a conducting metal or electrolyte, charges flow across the interface due to a difference between the Fermi level of the metal oxide and the reduction potential of the electrolyte solution.[4] For an n-type metal oxide, electrons flow from the material with a higher electronic energy level to the material with a lower energy level until the two materials are in equilibrium. If electrons have transferred out of the n-type metal oxide, a depletion region is formed near the surface of the metal oxide, and the conduction and valence bands at the surface bend upwards in electrochemical potential relative to the bulk material. Conversely, if electrons flow into the metal oxide, an accumulation region is formed, and the conduction and valence bands bend downwards in response.[3,4,5] The degree of band-bending depends on the electrolyte in contact with the metal oxide. If the system were biased to the flatband potential, the band bending induced by interactions with the electrolyte redox couple would reduce to zero and the potentials of the bands at the surface would be equal to the bulk material.

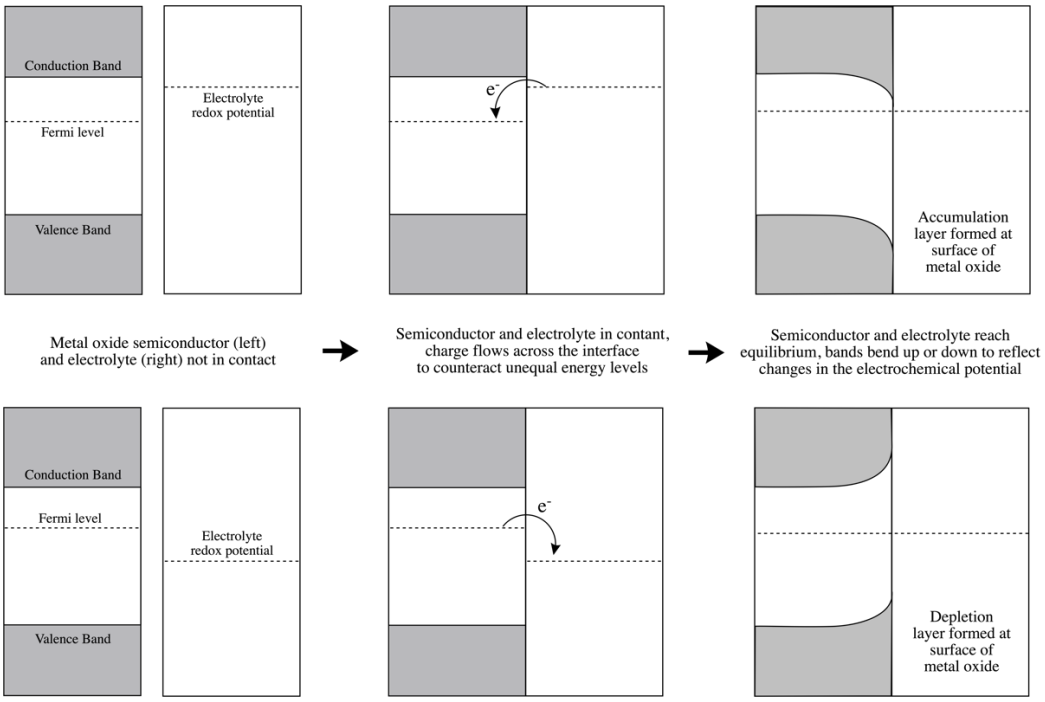

Schematic demonstrating the processes causing metal oxide bands to bend downward (top) and upward (bottom) for an n-type metal oxide in contact with an electrolyte solution in the absence of an external bias.

Flatband potentials for metal oxides are typically determined from experiments rather than from theory.[2] There are many ways to experimentally determine the flatband potential; the Mott-Schottky method is most common. The analysis is based off the Mott-Schottky equation, which for an n-type semiconductor, is written as:

$$\frac{1}{{C_{SC}}^2} = \frac{2}{\varepsilon\varepsilon_0 e N_D}\left(U - U_{FB} - \frac{k_B T}{e}\right)$$

where C_{sc} is the capacitance of the space charge layer per unit area, ε is the dielectric constant for the semiconductor, ε_0 is the permittivity of free space, e is the fundamental charge of an electron, N_D is the donor density, k_B is Boltzmann's constant, T is temperature, U is the applied potential, and U_{FB} is the flat-band potential.[1,3,6] From the equation, graphing C_{SC}^{-2} versus the applied potential should produce a line in the depletion region with an x-intercept equal to $U_{FB} - k_B T/e$, although the latter term is often disregarded as it is usually smaller than the error in the measurement, so the x-intercept can be approximated as the flat-band potential.[3] The donor density, or concentration of donors in the semiconductor, can also be extracted from these graphs from the slope of the line. Capacitance data is often collected through electrochemical impedance spectroscopy (EIS). EIS is a process in which a small perturbation with a set frequency is added

to an applied potential and the resulting current is measured.[7] EIS allows for resistive and capacitive charge transfers to be measured individually from one another when the data is set to a representative circuit diagram modeling the system, so the capacitance of a semiconductor-electrolyte junction can be determined.[7] The Mott-Schottky equation relies on the assumption that the Helmholtz layer capacitance is much larger than the space charge layer capacitance, which is often true.[3] Other issues that could arise include non-linearity and frequency dispersion. The Mott-Schottky plots may be non-linear or capacitance could be hard to measure if there are many defects on the surface of the semiconductor, whether intrinsic to the semiconductor or created by the experimenter.[3] This makes it difficult to find a linear region of the plot, which is needed to extract a flat-band potential. Frequency dispersion occurs when the Mott-Schottky plots taken at different perturbation frequencies in EIS are not equal. If the linear regions of these plots converge to the same x-intercept, then the flat-band potential can be extracted from the data, but if they converge to different x-intercepts, the flat-band potential is unclear from the data. Other methods for determining flatband potential include photocurrent onset potential[3], Gärtner-Butler analysis[1], chopped illumination[1], open-circuit potential at high illumination[1,3], the slurry method[8,9,10,11], cyclic voltammetry[3], and differential stress measurements[3,12].

Despite being a vital metric for semiconductors in photoelectrode applications, flatband potential values for common metal oxides show wide variability in the literature.[2] In this analysis, we compare flatband potential values in the literature from various publications for three common n-type metal oxide semiconductors: titanium dioxide (TiO_2), tin (IV) oxide (SnO_2), and zinc oxide (ZnO). The purpose of conducting this meta-analysis is to demonstrate the variation of values for flatband potential measurements and to assess the extent at which different variables in both metal oxide structure and measurement conditions could be contributing to such variation.

2.2 Methods

Flatband potentials for different metal oxides were collected from 502 articles from 156 different academic journals published in years from 1960 to 2020. In total, 505 values were collected for TiO_2, 97 values for SnO_2, and 223 values for ZnO. For each collected value, related experimental information was recorded including synthetic method, nanostructure morphology, substrate, pH of solution, electrolyte species and concentration, reference electrode, counter electrode, nanostructure dimensions, and the technique used to determine the flatband potential.

Statistical analyses were performed to determine what factors influenced the flatband potential of a metal oxide sample. All flatband potential values used in statistical analysis herein were measured in aqueous solutions. When comparing flatband potential versus pH, potential values were referenced to NHE. For all other analyses, potential values were referenced to RHE where $E_{FB}(vs\ RHE) = E_{FB}(vs\ NHE) + 0.059(pH)$. To determine whether there was a statistically significant difference between flatband potentials between categorical data sets, t-tests (for two categories) and ANOVA tests (for more than two categories) were used. If either test calculated $p < 0.05$, the variable was considered to significantly effect flatband potential. To determine whether flatband potentials trended with continuous variables (like particle length) in a statistically significant way, least-squares linear regressions were calculated and the 95% confidence intervals for the slopes of the regressions were used. If the confidence interval for the slope excluded zero, the trend was considered significant. For data displayed in histograms, all histograms have a bin-width of 0.1V with bins centered at $(0 \pm 0.1k)$ V for any integer k.

2.3 Results and Discussion

2.3.1. General Characteristics

Figure 1 shows histograms for the flatband potentials collected for the three different metal oxides. The mean flatband potential values are 0.088V vs RHE for TiO_2, 0.342V vs RHE for SnO_2, and 0.203V vs RHE for ZnO. The distributions for each metal oxide spread over a range of almost 2V, indicating an unusually large variation of flatband potential values for metal oxides in the literature. This could be in-part attributed to misuse of the Mott-Schottky method for flatband potential determination, as many of the assumptions made in the derivation of the Mott-Schottky equation are violated by nanomaterial metal oxides currently being synthesized and studied.[1] The Gaussian fits on the histograms show that the flatband potential values are normally distributed.

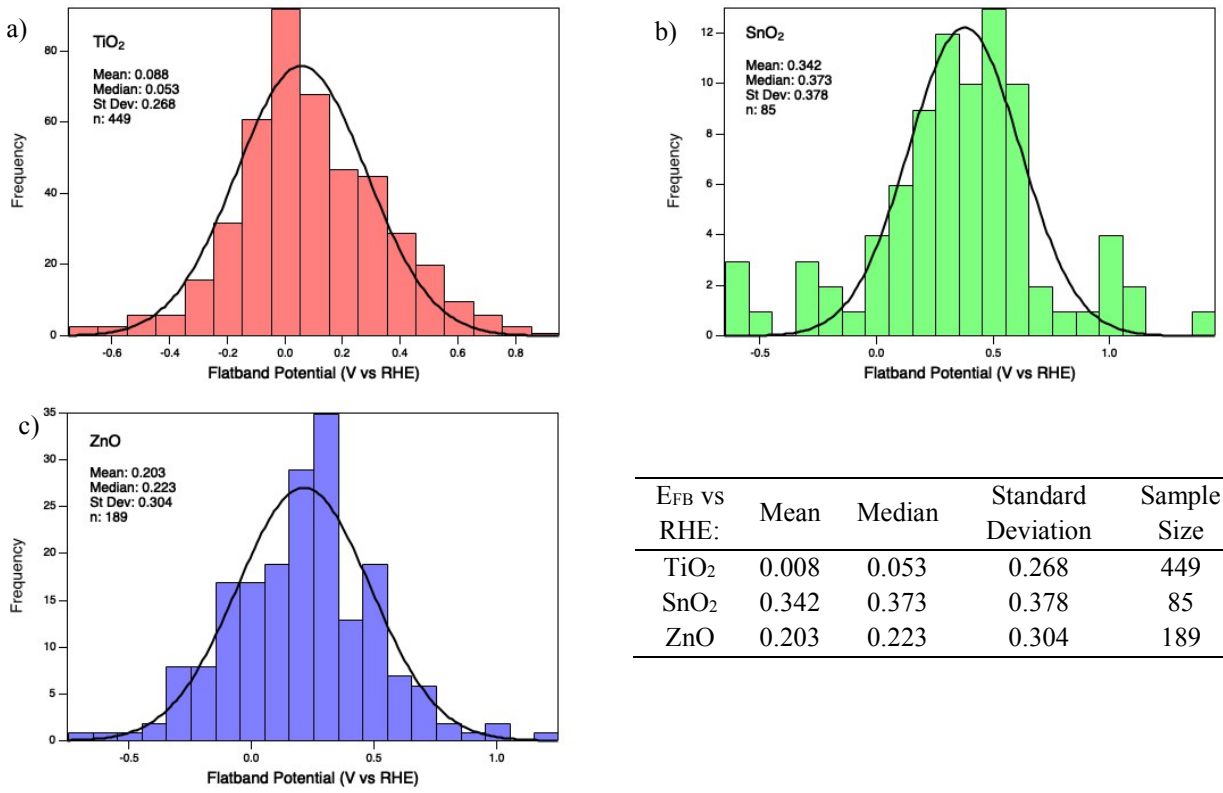

E_{FB} vs RHE:	Mean	Median	Standard Deviation	Sample Size
TiO_2	0.008	0.053	0.268	449
SnO_2	0.342	0.373	0.378	85
ZnO	0.203	0.223	0.304	189

Figure 1. Histograms showing the flatband potential distribution for TiO_2 (a), SnO_2 (b), and ZnO (c), where flatband potentials are vs RHE, and figures are superimposed with Gaussian distributions.

It is expected that the flatband potential of metal oxides would change with the pH of the solution if potentials were referenced to NHE. This is because oxygens on the surface of the metal oxide form hydroxyl groups whose charges are dependent on the pH of the solution. The effects of pH are illustrated in Figure 2, which shows the flatband potentials vs NHE plotted versus the pH of the solution in which the flatband potential was measured for the three metal oxides. The slope of the linear regression for TiO_2 is -0.060 ± 0.006 V/pH, matching the expected Nernstian dependence of –0.059 V/pH. The data for SnO_2 also matches this with a slope of -0.050 ± 0.027 V/pH. Surprisingly, the slope for the ZnO data has a confidence interval that narrowly misses the expected value, with a slope of -0.043 ± 0.015 V/pH.

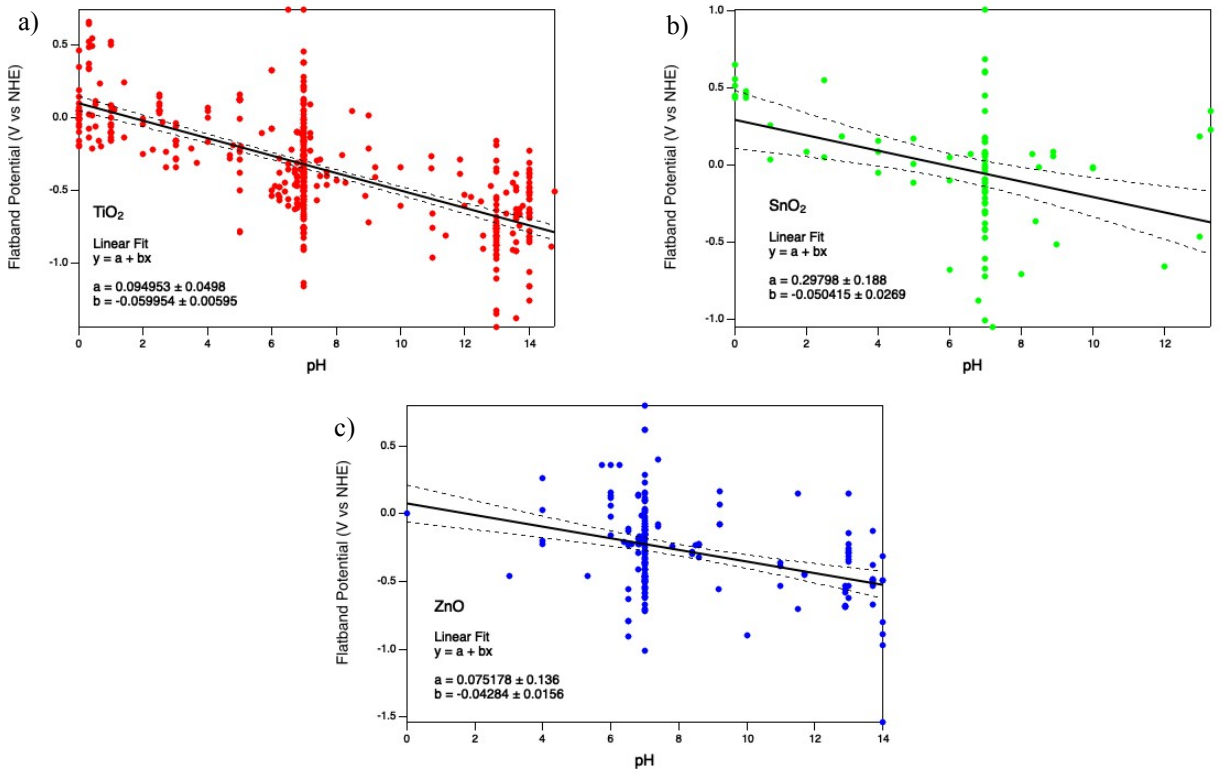

Figure 2. Flatband potentials vs NHE plotted against pH for TiO_2 (a), SnO_2 (b), and ZnO (c), with linear fits and 95% confidence intervals superimposed.

To investigate the reason why flatband potential did not change with pH as expected for ZnO, the data points in Figure 2c were separated by many categories to see what could be causing the deviation from the expected trend. Upon separating the data into the common morphologies for ZnO nanomaterials—nanowires, nanoparticles, single crystals, and thin films—a potential explanation arose. Figure 3a shows the flatband potential vs NHE versus pH for ZnO thin films. The figure shows that the flatband potentials for ZnO thin films seem to have no dependence on the pH of the solution. If we remove the thin film data points from the ZnO data set, the resulting data is shown in Figure 3b. With the thin film data points removed, the slope for the remaining data set is –0.067 ± 0.021 V/pH, containing the expected Nernstian dependence of –0.059V/pH. One potential reason that ZnO thin films may lack a pH dependence is related to the main crystalline form of ZnO, wurtzite.[13] The crystal structure of wurtzite lacks an inversion center, so when a wurtzite crystal is cut perpendicular to the main axis, two polar surfaces are formed. One is the (0001) crystal facet, which is capped with all Zn atoms, and the other is the $(000\bar{1})$ facet, capped with all O atoms. ZnO thin film growth favors the polar (0001) and $(000\bar{1})$ facets on the

surface over other non-polar crystal facets.[13] A dependence of flatband potential on pH to -30 mV/pH has been observed for the $(000\bar{1})$ facet before, which is significantly less than the expected -59 mV/pH.[14] This difference was attributed to the change in Helmholtz capacitance brought on by the polarity of the surface.[14] The polarity of the surface for ZnO thin films could explain the reduced dependence of flatband potential on pH for ZnO thin films observed in Figure 3a.

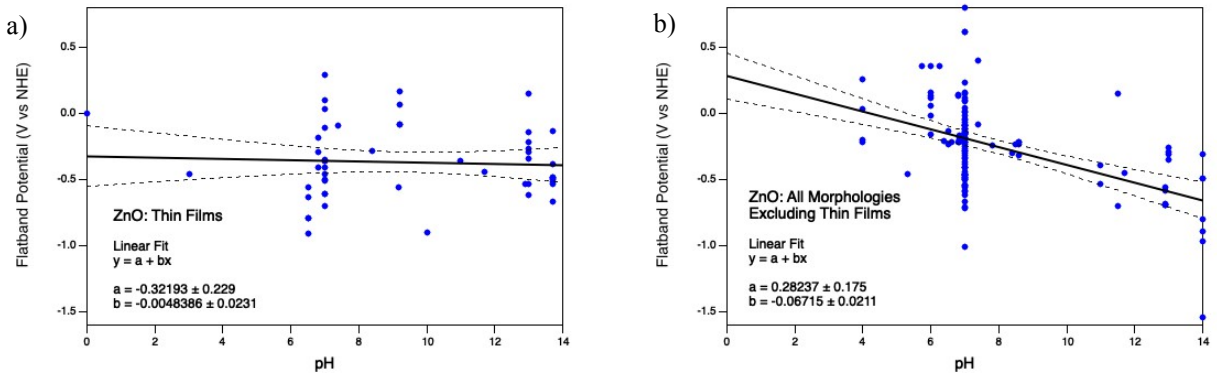

Figure 3. Flatband potential (vs NHE) plotted against pH for ZnO thin films (a) and all other morphologies for ZnO (b), with linear fits and 95% confidence intervals superimposed.

2.3.2. Crystalline Phase Effects

Metal oxides can often take on multiple crystalline structures, and the crystallinity of the metal oxide can influence its physical and chemical properties. TiO_2 has three common crystalline phases: the tetragonal rutile and anatase phases and the orthorhombic brookite phase. Rutile is the most thermodynamically stable phase, while anatase and brookite are considered to be metastable. Rutile and anatase are far more common that brookite in the literature. Figure 4a shows the overlaid histograms of the flatband potential values for different crystalline phases of TiO_2. The overlaid Gaussian fits show that the data is mostly normally distributed. The exception is anatase TiO_2 which has a bimodal distribution for reasons discussed in the next section. The mean flatband potential values are 0.050V vs RHE for rutile TiO_2, 0.163V vs RHE for anatase TiO_2, and –0.048V vs RHE for brookite TiO_2. The difference between these mean flatband potentials is statistically significant (ANOVA test, $p=1.43\times10^{-6}$). Many TiO_2 samples have a mix of crystalline phases. Flatband potentials for mixed anatase-rutile TiO_2 samples are shown in Figure 4b. The data suggests that the flatband potential increases as the percent rutile increases and the percent anatase decreases, though this analysis is hindered by a small sample size. The data also suggests that the

flatband potentials for mixed samples is not a simple weighted average of the flatband potentials of that for rutile and anatase, since the y-intercepts (100% rutile and 100% anatase) do not correspond to the flatband potentials expected for pure rutile or pure anatase TiO_2.

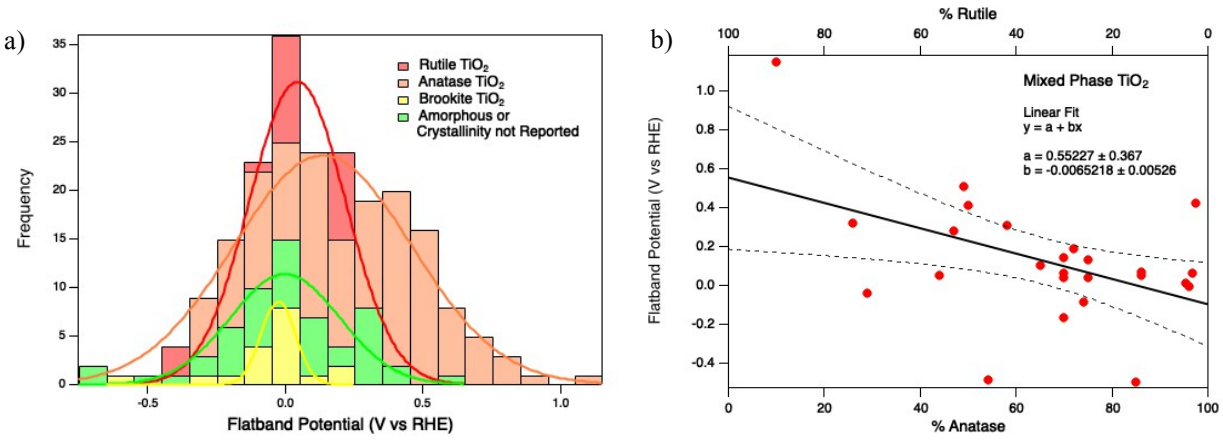

E_{FB} vs RHE:	Mean	Median	Standard Deviation	Sample Size
Rutile TiO_2	0.050	0.041	0.191	140
Anatase TiO_2	0.163	0.137	0.170	186
Brookite TiO_2	–0.048	–0.012	0.170	18

Figure 4. (a) Overlaid distributions of flatband potentials vs RHE for different crystalline phases of TiO_2 with Gaussian distributions superimposed, and (b) flatband potentials vs RHE for anatase-rutile mixed phase TiO_2 samples.

SnO_2 has one main crystalline form, the tetragonal phase rutile. Rutile SnO_2 is also referred to as cassiterite in the literature. Because there is only one major form of crystalline SnO_2, the effects of crystallinity on SnO_2 flatband potentials were not explored. ZnO has two main crystalline phases: the hexagonal form wurtzite and the cubic form zincblende. Wurtzite is the more thermodynamically stable form and thus more common. No flatband potentials for pure zincblende ZnO were found in this analysis, so the effects of crystalline structure on ZnO flatband potentials were not explored.

2.3.3. Morphology Effects

Metal oxide nanomaterials come in a variety of different morphologies, and this section investigates the impact of morphology on the flatband potential for different metal oxides. Morphology does not cause a statistically significant difference in flatband potential values for

rutile TiO_2 (ANOVA test, p=0.378), SnO_2 (ANOVA test, p=0.929), and ZnO (ANOVA test, p=0.406).

For anatase TiO_2, the most common morphologies were nanotubes, nanoparticles, thin films, and single crystals. Figure 5a shows the flatband potentials vs RHE for different anatase TiO_2 morphologies, with Gaussian fits overlaid demonstrating that the data is normally distributed. It is clear that morphology is playing a significant role in the flatband potential for anatase TiO_2 (ANOVA test, $p=2.02\times10^{-18}$). As evident in Figure 5b, flatband potentials for nanotubes are quite distinct from those of all other morphologies (t-test, $p=5.26\times10^{-22}$), with the mean flatband potential as 0.408V vs RHE for nanotubes and 0.017V vs RHE for all other morphologies. If we look only at the nanoparticles, thin films, and single crystals, the differences in flatband potential values are not significant (ANOVA test, p=0.259). The distinct separation between nanotube flatband potential values and values for other morphologies explains the bimodal distribution noted for anatase TiO_2 seen in Figure 4a.

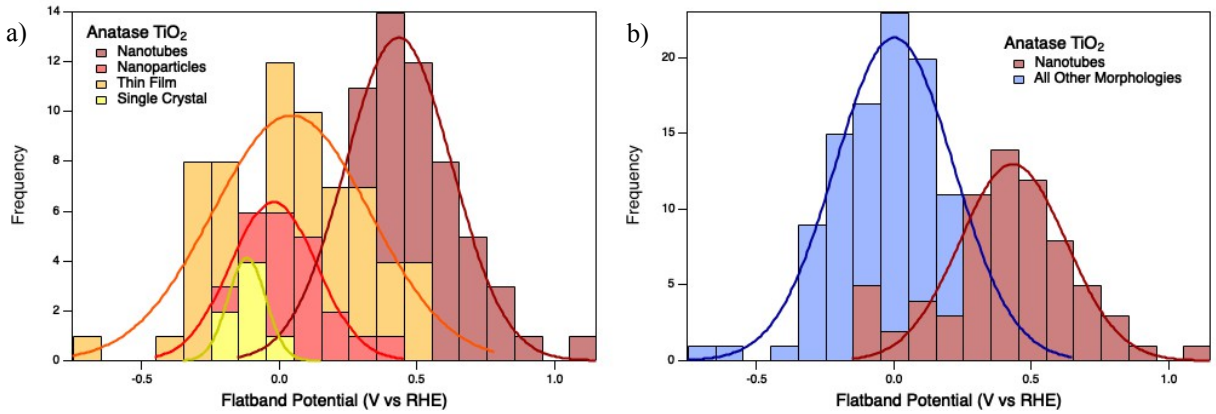

E_{FB} vs RHE:	Mean	Median	Standard Deviation	Sample Size
Nanotubes	0.408	0.415	0.245	69
Nanoparticles	0.018	0.018	0.155	24
Thin Films	0.036	0.017	0.257	67
Single Crystal	–0.133	–0.122	0.044	7

Figure 5. (a) Overlaid histograms of flatband potentials vs RHE for different anatase TiO_2 morphologies with Gaussian fits superimposed, and (b) histograms showing nanotubes in red and all non-nanotube morphologies in blue with Gaussian fits superimposed.

The reason why anatase nanotubes experience a large (~0.4V) positive shift in flatband potential relative to other anatase samples is not clear, though it is likely related to the unique

geometry of nanotubes. Unlike the other geometries, nanotubes possess long and narrow pores which could be constricting robust electrolyte diffusion between the bulk electrolyte and the surface of the nanotubes. The disruption of proper and evenly distributed current flow between electrodes in solution and the TiO_2 nanotubes might hinder the measurement of the true flatband potential. Another potential consequence of the nanotube morphology is that the width of the depletion layer could become large relative to the wall thickness of the nanotubes, which would impact the measurement of the flatband potential if the depletion layer width exceeds the width of the nanotube walls. The nanotube flatband potential values for anatase TiO_2 could be skewing data if these values are not real but rather an artifact of the measurement. To assess this, the flatband potential values for different crystallinities of TiO_2 are explored once again.

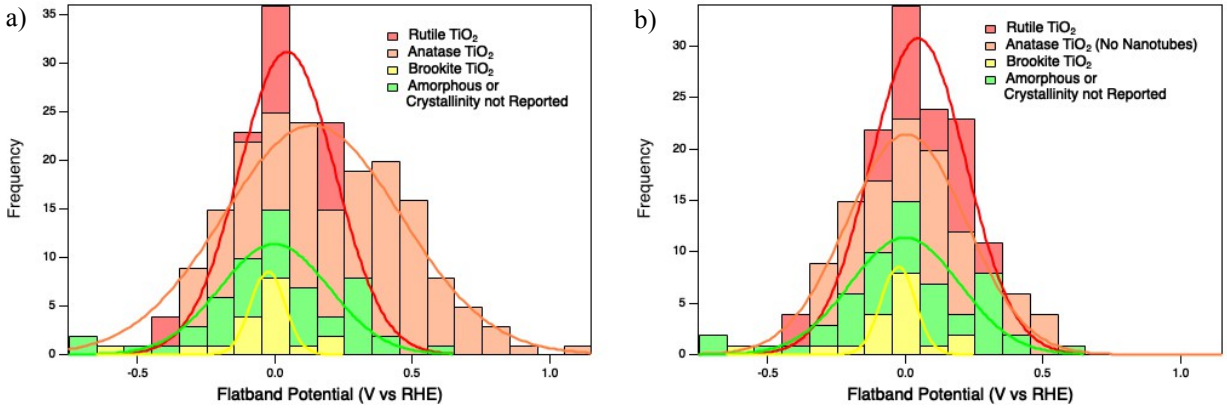

Figure 6. Overlaid histograms for the flatband potentials vs RHE of the different crystalline phases of TiO_2 with (a) and without (b) anatase nanotube data points, with Gaussian fits superimposed.

Figure 6 shows the comparison between anatase, rutile, and brookite TiO_2 both with (a) and without (b) anatase nanotube data points. From the figures, it is apparent that the anatase TiO_2 flatband potential values are very similar to the other crystalline phases when the nanotubes are removed. The mean values for flatband potentials are now 0.049V vs RHE for rutile, 0.018V vs RHE for anatase, and –0.048V vs RHE for brookite, and these means are not significantly different from each other (ANOVA test, $p=0.1719$). This is in stark contrast to the commonly-made statement that the flatband potentials, and similarly the conduction band edges, for rutile and anatase TiO_2 are offset by approximately 0.2 eV. The broad range of potential values also cautions against making sweeping generalizations about the relative band placements for rutile and anatase TiO_2 as they seem to be highly variable between samples.

For metal oxide single crystals, there are multiple studies suggesting that the crystal facet being used affects the flatband potential.[15,16,17] For measurements taken in aqueous solutions, the interactions of water on the surface could be the driving force for changes in flatband potential. For anatase TiO_2, it was proposed that the (001) surface dissociatively adsorbed water, making the surface more acidic and attracting less protons, shifting the flatband potential more negative relative to the (101) surface which molecularly adsorbed water.[18] In this analysis, there were only sufficient data points to study the effects of crystal facets for rutile TiO_2 and no other metal oxide.

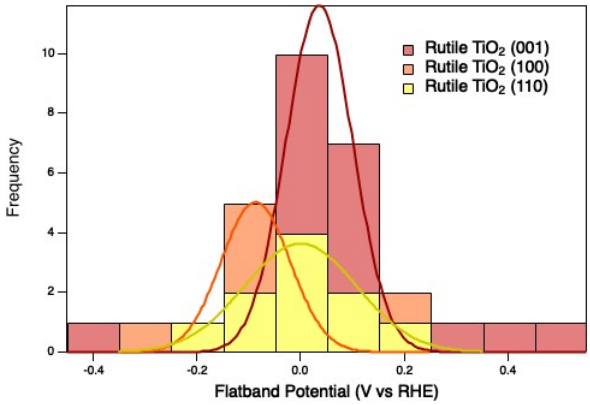

E_{FB} vs RHE:	Mean	Median	Standard Deviation	Sample Size
(001)	0.060	0.037	0.170	24
(100)	–0.051	–0.086	0.150	12
(110)	–0.009	–0.027	0.125	10

Figure 7. Overlaid histograms for the flatband potential values vs RHE for the (001), (100), and (110) crystal facets of single crystal rutile TiO_2 materials, with overlaid Gaussian fits.

Figure 7 shows the flatband potential values for different crystal facets of rutile TiO_2 with overlaid Gaussian fits demonstrating that the values are mostly normally distributed. The mean flatband potentials are 0.060V vs RHE, –0.051V vs RHE, and –0.009V vs RHE for the (001), (100), and (110) facets, respectively. Though the crystal facet does appear to affect the flatband potential for rutile TiO_2 single crystals, the results are not statistically significant (ANOVA test, p=0.1268). A larger sample size would be needed to determine the effects of crystal facet on flatband potential.

2.3.4. Synthetic Technique Effects

Metal oxides can be synthesized by many different techniques. Rutile TiO_2 was commonly synthesized by the hydrothermal method, sputtering, anodic oxidation, and many other techniques, but the technique used to synthesize the rutile TiO_2 nanomaterials did not have a statistically significant impact on the flatband potential of the material (ANOVA test, p=0.0618). SnO_2 was commonly synthesized using techniques like spray pyrolysis, the hydrothermal method, anodic

oxidation, and the sol-gel method, though the method for synthesis did not impact the flatband potential (ANOVA test, p=0.940). ZnO was often synthesized by electrodeposition, the hydrothermal method, the sol-gel method, thermal decomposition, chemical vapor deposition, and several other methods. The ZnO flatband potential was also not significantly impacted by the synthetic method (ANOVA test, p=0.338).

Anatase TiO_2 was commonly synthesized by anodic oxidation, the hydrothermal method, the sol-gel method, and sputtering. It was found that the method of synthesis did significantly impact the flatband potential (ANOVA test, $p=1.20x10^{-18}$). Figure 8 shows the distribution of flatband potentials for different synthesis techniques for anatase TiO_2.

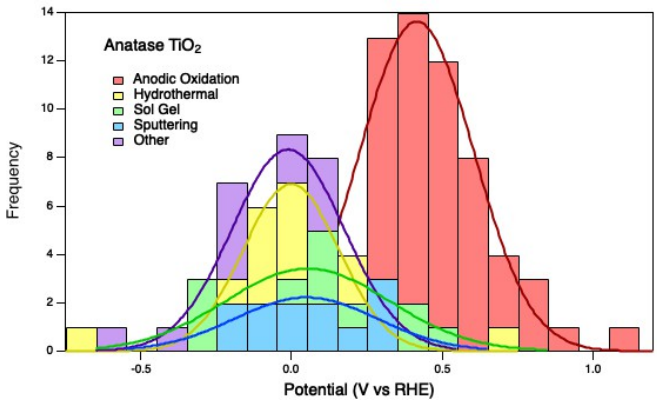

E_{FB} vs RHE:	Mean	Median	Standard Deviation	Sample Size
Anodic Oxidation	0.404	0.415	0.236	70
Hydrothermal	0.021	0.018	0.241	30
Sol Gel	0.055	0.069	0.243	22
Sputtering	0.055	0.027	0.192	12

Figure 8. Overlaid histograms of the flatband potentials vs RHE for anatase TiO_2 synthesized by different methods, with overlaid Gaussian fits.

The distinction between anodic oxidation and other synthetic techniques likely lies in the fact that anatase TiO_2 nanotubes are almost exclusively made via anodic oxidation. Of the 70 flatband potential values for anatase TiO_2 synthesized by anodic oxidation, 67 were nanotubes. As seen in Figure 6 and discussed above, anatase TiO_2 nanotubes have a distinct flatband potential. If we remove the nanotube data points from the sample, synthetic technique no longer impacts the flatband potential for anatase TiO_2 (ANOVA test, p=0.406).

2.3.5. Substrate Effects

Nanomaterial metal oxides are often synthesized on or deposited onto conductive substrates for electrochemical studies or uses in potential applications. Common substrates are transparent conducting oxides (TCOs), which are conductive materials that are optically clear in

the visible regions. The more widely used TCOs are fluorine-doped tin oxide (FTO) and indium tin oxide (ITO), often used as a thin layer on top of a glass sheet. Sometimes, metals are used as conductive substrates as well. The substrate used did not have a significant impact on the flatband potential for rutile TiO_2 (ANOVA test, p=0.346), SnO_2 (ANOVA test, p=0.186), and ZnO (ANOVA test, p=0.292). For anatase TiO_2, there was a significant impact on the flatband potential base on the substrate used (ANOVA test, $p=1.308 \times 10^{-16}$).

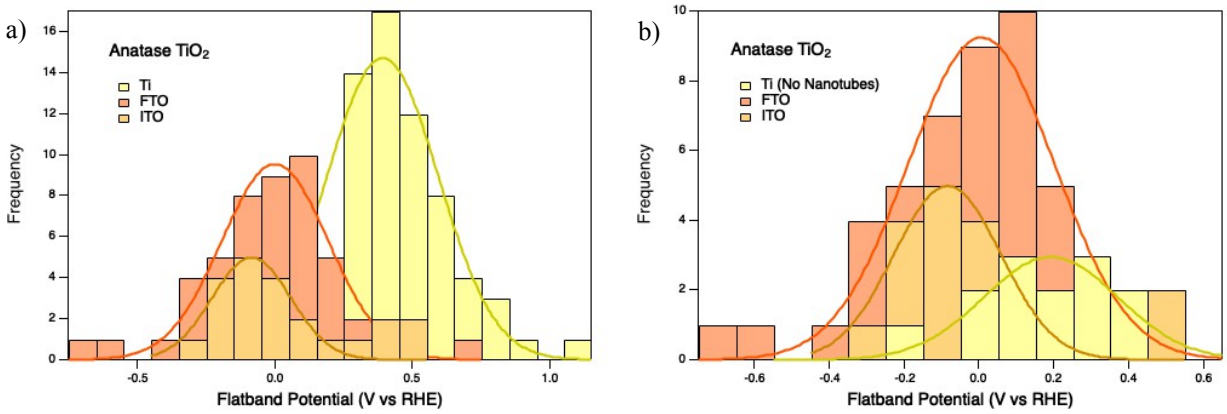

E_{FB} vs RHE:	Mean	Median	Standard Deviation	Sample Size
FTO	0.005	0.000	0.259	50
ITO	0.046	–0.020	0.239	22
Ti	0.374	0.375	0.243	81
Ti (no nanotubes)	0.163	0.176	0.171	13

Figure 9. Flatband potential values vs RHE for anatase TiO_2 on different substrates with (a) and without (b) nanotube data points, with overlaid Gaussian fits.

As shown in Figure 9a, anatase TiO_2 nanomaterials on Ti substrates appear to have a much more positive flatband potential. Anatase TiO_2 nanotubes are almost exclusively grown on Ti substrates, so the more positive flatband potential for anatase TiO_2 nanotubes is likely contributing to the positively shifted values for anatase on Ti substrates. Figure 9b shows the histograms with the nanotube data points removed. The difference in mean values for flatband potentials of anatase TiO_2 on different substrates is still significant (ANOVA test, p=0.0367), with the significant difference being between the mean value for anatase TiO_2 on FTO, –0.008V vs RHE, and on Ti, 0.163V vs RHE (t-test, p=0.0215). Interestingly, no significant difference was seen for rutile TiO_2 on Ti, SnO_2 on Sn, and ZnO on Zn. It is therefore unclear whether the significant difference in flatband potential for anatase TiO_2 nanoparticles is an artifact of anatase TiO_2 nanotubes being

almost exclusively studied on Ti substrates or if the change is related to the structure of the nanotubes compared to other morphologies. Because the shift in flatband potential is much larger for anatase TiO_2 nanotubes compared to the shift caused by using a Ti substrate for non-nanotube morphologies, that structure of nanotubes is likely a major contributing factor.

2.3.6. Nanomaterial Dimension Effects

The effects of the dimensions of metal oxide nanomaterials on the flatband potentials of those materials was studied for multiple different morphologies. For rutile TiO_2, anatase TiO_2, SnO_2, and ZnO, there was no statistically significant trends between flatband potentials and thin film thickness, nanoparticle diameter, nanorod/nanowire length and width, and nanotube length. The trend between nanorod/nanowire/nanotube length and flatband potential is shown in Figure 10, clearly demonstrating how the length of these nanomaterials does not impact flatband potential. For some of these analyses however, the sample size was small and confidence intervals were large, so factors that might actually impact flatband potential may not be producing statistically significant results.

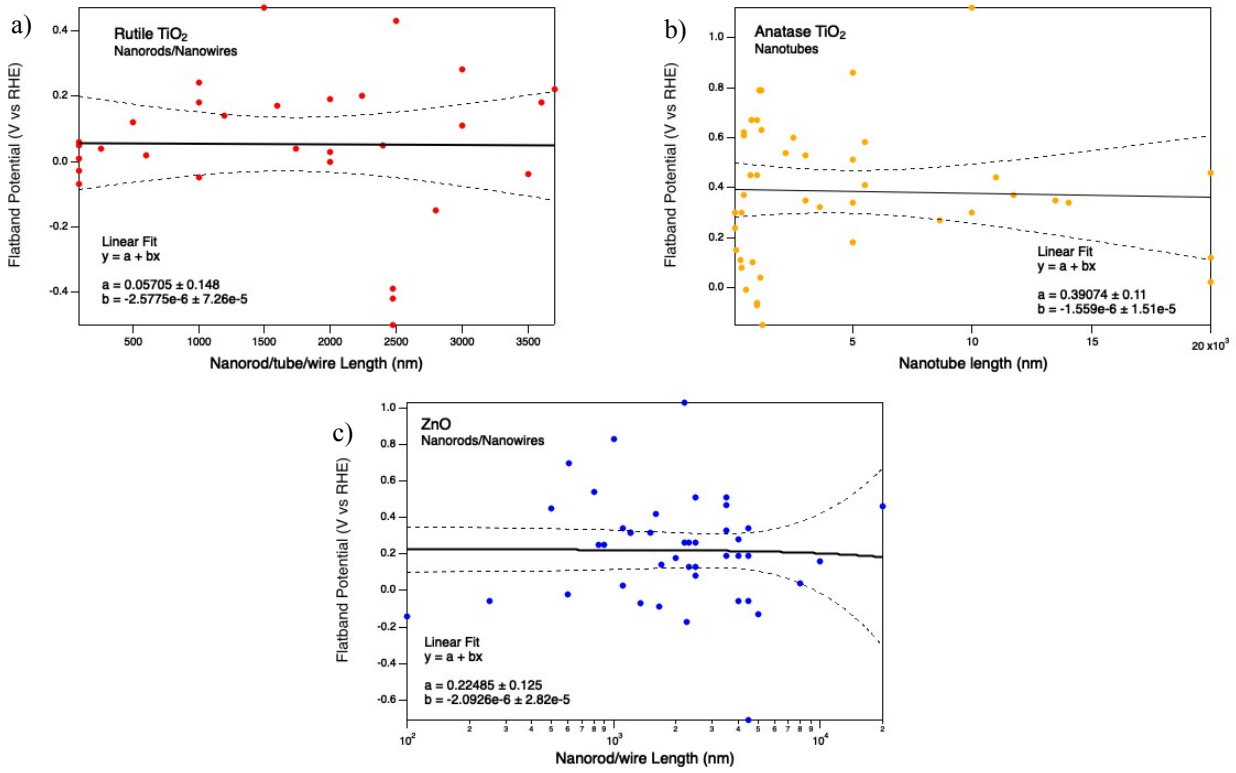

Figure 10. Flatband potential values vs RHE plotted against the length of the nanostructures for rutile TiO_2 (a), anatase TiO_2 (b), and ZnO (c), with linear fits and 95% confidence bands overlaid.

For anatase TiO_2 nanotubes, there is a significant increase in the flatband potential as the width of the nanotubes increased, as shown in Figure 11a. The wall thickness for the anatase TiO_2 nanotubes does not appear to impact the flatband potential (Figure 11c). However, an increase in the flatband potential is correlated to an increase in the nanotube pore diameter (Figure 11b), though not statistically significant.

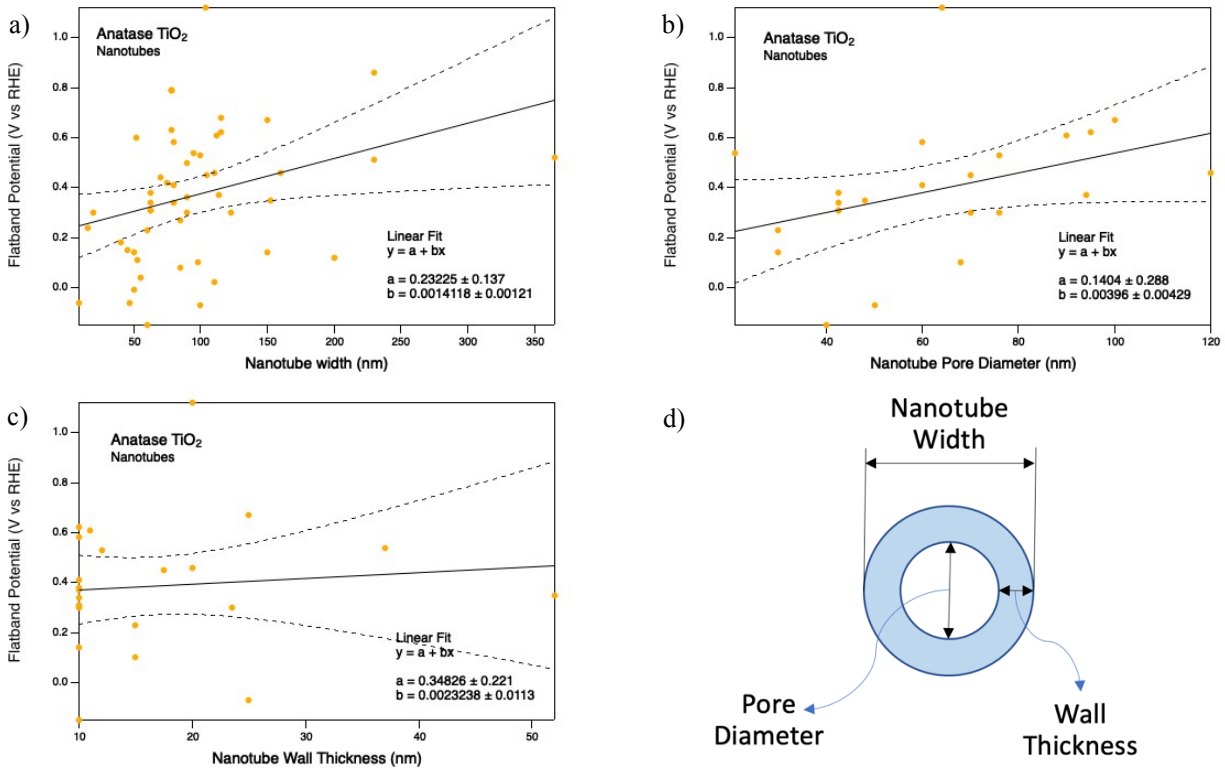

Figure 11. Flatband potential vs RHE for anatase TiO_2 nanotubes compared to the nanotube width (a), pore diameter (b), and wall thickness (c), with linear fits and 95% confidence bands overlaid, and the dimensional parameters described in (d) showing a cross section of a nanotube.

The independence of flatband potential on the nanotube wall thickness suggests that the exceedingly positive flatband potential values for anatase TiO_2 nanotubes are not the result of the depletion layer exceeding the nanotube wall thickness, as previously proposed. Increasing the nanotube width would also increase the pore diameter for any given wall thickness, so it is unsurprising that Figures 11a and 11b show similar positive trends. However, it is unclear why increasing the diameter of the nanotube would shift the flatband potential positively.

2.3.7. Electrolyte Cation Effects

Flatband potential measurements are often made with the metal oxide in contact with a conducting electrolyte solution. Common cations used in electrolytes were K^+, Na^+, and Li^+. The cation used did not have a significant impact on the flatband potential values for rutile TiO_2 (t-test, p=0.0727), anatase TiO_2 (ANOVA test, p=0.1868), and SnO_2 (t-test, p=0.4575), but did significantly impact ZnO flatband potentials (t-test, p=0.0414), as seen in Figure 12c. The mean flatband potential value for ZnO in solutions containing K^+ was 0.088V vs RHE, while the mean for solutions with Na^+ was 0.210V vs RHE. Similarly, the concentration of cations did not correlate to changes in flatband potential for anatase TiO_2, rutile TiO_2, and SnO_2, but did impact the flatband potential of ZnO. A negative correlation was found between Na^+ concentration and flatband potential for ZnO (Figure 12b). There is also a negative correlation between K^+ concentration and the flatband potential for ZnO, though it is not statistically significant (Figure 12a).

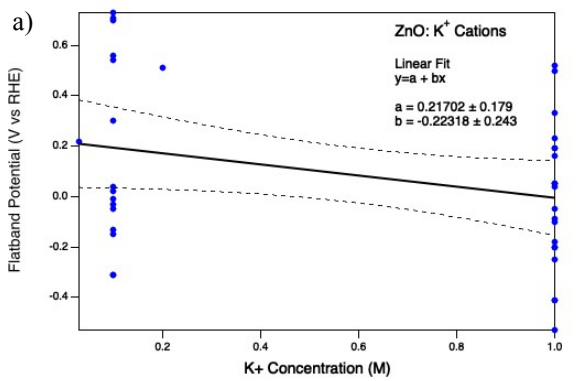

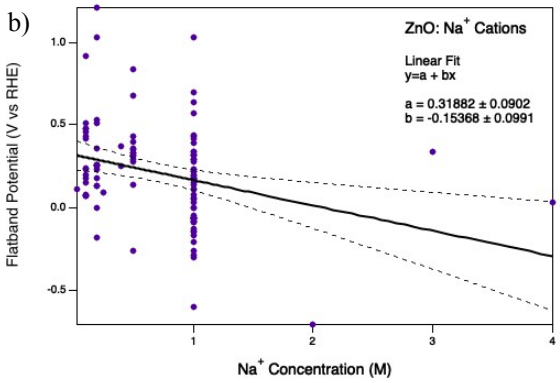

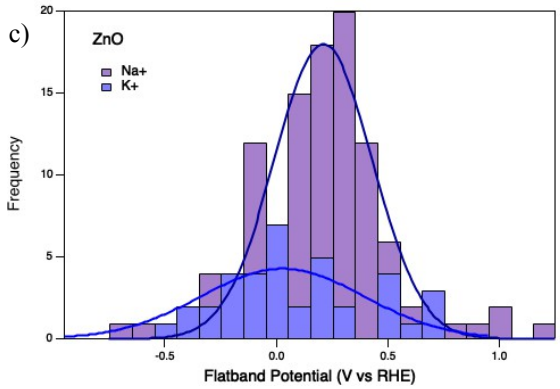

E_{FB} vs RHE:	Mean	Median	Standard Deviation	Sample Size
Na^+	0.210	0.221	0.301	107
K^+	0.088	0.036	0.337	37

Figure 12. Flatband potential vs RHE for anatase TiO_2 nanotubes versus the concentration of sodium cations in the electrolyte, with linear fit and 95% confidence bands overlaid.

Changes in flatband potential due to changes in both the type and concentration of non-proton cations in the electrolyte have been seen for TiO_2 before.[19,20] However, this change has only been observed in non-aqueous solvents. For non-aqueous solvents, an increase in cation concentration has shown positive shifts in the flatband potential due to adsorption and intercalation of the cation with the metal oxide.[19,20] This is analogous to how increased proton concentration (lower pH) in aqueous solvents shifts the flatband potential positively as well. In aqueous solvents, the proton concentration dominates the change in flatband potential, so the electrolyte cation has no effect.[3,20] This agrees with the lack of a significant trend between cation type and concentration and flatband potential for rutile TiO_2, anatase TiO_2, and SnO_2, as these data were collected in aqueous solvents. The ZnO data in Figure 12, collected in aqueous solvents, contradicts these trends, with the flatband potential shifting negatively as cation concentration increases. While the reason for this is trend is unknown, one possible explanation is that a larger concentration of cations in the double layer could shield protons in the bulk from electrostatic attraction to the surface, effectively decreasing the amount of proton adsorption and therefore shifting the flatband potential negatively. Since ZnO is unstable in acidic conditions, most flatband potential measurements were made in basic solutions, where proton concentrations are much smaller than cation concentrations, supporting this theory. However, this does not fully explain why similar trends are not seen for SnO_2 and TiO_2.

2.4 Conclusion

Flatband potential values for TiO_2, SnO_2, and ZnO in the literature showed average values of 0.088V, 0.342V, and 0.203V vs RHE, respectively, with wide ranges of up to 2V. Due to the large spread of values for these metal oxides, assigning a single flatband potential value to a metal oxide would be a problematic generalization. Flatband potential values for the metal oxides shifted –59 mV/pH with the exception of ZnO thin film flatband potentials, which showed an apparent lack of dependence on solution pH. The flatband potentials for anatase TiO_2 nanotubes were shifted ~ 0.4V positive of other anatase TiO_2 morphologies, though it remains unclear whether this shift reflects a true difference in flatband potentials or is an artifact of inappropriate measurements. Without the nanotube data points, anatase TiO_2 and rutile TiO_2 did not have a significant difference in mean flatband potential values, in contrast to what is often assumed for these two crystalline phases. Flatband potentials for ZnO appeared to shift negatively with increasing cation

concentration, though previous literature precedence with other metal oxides suggests that flatband potential should not be affected by non-proton cations in aqueous solutions. The findings of these analyses demonstrate the need to recognize the sensitivity of flatband potentials to multiple factors and the spread of flatband potential values that exist even between similar nanomaterials.

2.5 References

(1) Hankin, A.; Bedoya-Lora, F. E.; Alexander, J. C.; Regoutz, A.; Kelsall, G. H. Flat Band Potential Determination: Avoiding the Pitfalls. *J. Mater. Chem. A* **2019**, *7* (45), 26162–26176.

(2) Hankin, A.; Alexander, J. C.; Kelsall, G. H. Constraints to the Flat Band Potential of Hematite Photo-Electrodes. *Phys. Chem. Chem. Phys.* **2014**, *16* (30), 16176–16186.

(3) *Semiconductor Electrodes*; Finklea, H. O., Ed.; Elsevier: Amsterdam, 1988.

(4) Nozik, A. J.; Memming, R. Physical Chemistry of Semiconductor-Liquid Interfaces. *J. Phys. Chem.* **1996**, *100* (31), 13061–13078.

(5) Zhang, Z.; Yates, J. T. Band Bending in Semiconductors: Chemical and Physical Consequences at Surfaces and Interfaces. *Chem. Rev.* **2012**, *112* (10), 5520–5551.

(6) Gelderman, K.; Lee, L.; Donne, S. W. Flat-Band Potential of a Semiconductor: Using the Mott-Schottky Equation. *J. Chem. Educ.* **2007**, *84* (4), 685–688.

(7) Bredar, A. R. C.; Chown, A. L.; Burton, A. R.; Farnum, B. H. Electrochemical Impedance Spectroscopy of Metal Oxide Electrodes for Energy Applications. *ACS Appl. Energy Mater.* **2020**, *3* (1), 66–98.

(8) Macyk, W.; Burgeth, G.; Kisch, H. Photoelectrochemical Properties of Platinum (IV) Chloride Surface Modified TiO2. *Photochem. Photobiol. Sci.* **2003**, *2* (3), 322–328.

(9) Di Paola, A.; Bellardita, M.; Ceccato, R.; Palmisano, L.; Parrino, F. Highly Active Photocatalytic TiO2 Powders Obtained by Thermohydrolysis of TiCl4 in Water. *J. Phys. Chem. C* **2009**, *113* (34), 15166–15174.

(10) Ward, M. D.; White, J. R.; Bard, A. J. Electrochemical Investigation of the Energetics of Particulate Titanium Dioxide Photocatalysts. The Methyl Viologen-Acetate System. *J. Am. Chem. Soc.* **1983**, *105*, 27–31.

(11) White, J. R.; Bard, A. J. Electrochemical Investigation of Photocatalysis at CdS Suspensions in the Presence of Methylviologen. *J. Phys. Chem.* **1985**, *89* (10), 1947–1954.

(12) Handley, L. J.; Bard, A. J. Semiconductor Electrodes XXIII. The Determination of Flatband Potentials from Differential Stress Measurements with Attached Piezoelectric Detectors. *J. Electrochem. Soc.* **1980**, *127* (2), 338–343.

(13) Claeyssens, F.; Freeman, C. L.; Allan, N. L.; Sun, Y.; Ashfold, M. N. R.; Harding, J. H. Growth of ZnO Thin Films - Experiment and Theory. *J. Mater. Chem.* **2005**, *15* (1), 139–148.

(14) Pettinger, B.; Schöppel, H.-R.; Yokoyama, T.; Gerischer, H. Tunnelling Processes at Highly Doped ZnO-Electrodes in Aqueous Electrolytes Part II: Electron Exchange with the Valence Band. *Berichte der Bunsengesellschaft/Physical Chem. Chem. Phys.* **1974**, *78* (10), 1024–1030.

(15) Kavan, L.; Grätzel, M.; Gilbert, S. E.; Klemenz, C.; Scheel, H. J. Electrochemical and Photoelectrochemical Investigation of Single-Crystal Anatase. *J. Am. Chem. Soc.* **1996**, *118* (28), 6716–6723.

(16) Hengerer, R.; Kavan, L.; Krtil, P.; Grätzel, M. Orientation Dependence of Charge-Transfer Processes on TiO2 (Anatase) Single Crystals. *J. Electrochem. Soc.* **2000**, *147* (4), 1467–1472.

(17) Lu, Y.; Choi, D.; Nelson, J.; Yang, O.-B.; Parkinson, B. A. Adsorption, Desorption, and Sensitization of Low-Index Anatase and Rutile Surfaces by the Ruthenium Complex Dye N3. *J. Electrochem. Soc.* **2006**, *153* (8), E131–E137.

(18) Liu, G.; Yang, H. G.; Pan, J.; Yang, Y. Q.; Lu, G. Q. M.; Cheng, H. M. Titanium Dioxide Crystals with Tailored Facets. *Chem. Rev.* **2014**, *114* (19), 9559–9612.

(19) Redmond, G.; Fitzmaurice, D. Spectroscopic Determination of Flatband Potentials for Polycrystalline TiO2 Electrodes in Nonaqueous Solvents. *J. Phys. Chem.* **1993**, *97* (7), 1426–1430.

(20) ODonnell, R. M.; Sampaio, R. N.; Barr, T. J.; Meyer, G. J. Electric Fields and Charge Screening in Dye Sensitized Mesoporous Nanocrystalline TiO2 Thin Films. *J. Phys. Chem. C* **2014**, *118* (30), 16976–16986.

Flatband Potential Literature Data References

A. J. Nozik, in A. Heller (ed.), Semiconductor Liquid-Junction Solar Cells, Proceedings Vol. 77-3, The Electrochemical Society, NJ, 1977, 272-289.

Acevedo-Peña, P.; Carrera-Crespo, J. E.; González, F.; González, I. Effect of Heat Treatment on the Crystal Phase Composition, Semiconducting Properties and Photoelectrocatalytic Color Removal Efficiency of TiO2 Nanotubes Arrays. *Electrochim. Acta* **2014**, *140*, 564–571.

Adam, R. E.; Pirhashemi, M.; Elhag, S.; Liu, X.; Habibi-Yangjeh, A.; Willander, M.; Nur, O. ZnO/Ag/Ag2WO4 Photo-Electrodes with Plasmonic Behavior for Enhanced Photoelectrochemical Water Oxidation. *RSC Adv.* **2019**, *9* (15), 8271–8279.

Ahmad, A.; Yerlikaya, G.; Zia-ur-Rehman; Paksoy, H.; Kardaş, G. Enhanced Photoelectrochemical Water Splitting Using Gadolinium Doped Titanium Dioxide Nanorod Array Photoanodes. *Int. J. Hydrogen Energy* **2020**, *45* (4), 2709–2719.

Ahmed, A. Y.; Kandiel, T. A.; Oekermann, T.; Günnemann, C.; Bahnemann, D. Mechanistic Investigations of Photoelectrochemical Water and Methanol Oxidation on Well-Defined TiO2 Anatase (101) and Rutile (110) Surfaces. *ACS Appl. Energy Mater.* **2019**, *2* (7), 5308–5318.

Ahmed, A. Y.; Oekermann, T.; Lindner, P.; Bahnemann, D. Comparison of the Photoelectrochemical Oxidation of Methanol on Rutile TiO2 (001) and (100) Single Crystal Faces Studied by Intensity Modulated Photocurrent Spectroscopy. *Phys. Chem. Chem. Phys.* **2012**, *14* (8), 2774–2783.

Ahn, K.-S.; Yan, Y.; Lee, S.-H.; Deutsch, T.; Turner, J.; Tracy, C. E.; Perkins, C. L.; Al-Jassim, M. Photoelectrochemical Properties of N-Incorporated ZnO Films Deposited by Reactive RF Magnetron Sputtering. *J. Electrochem. Soc.* **2007**, *154* (9), B956–B959.

Ali, H.; Brahimi, R.; Outemzabet, R.; Bellal, B.; Trari, M. Comparative Analysis of Structural and Photoelectrochemical Properties of Pure and Sb Doped SnO2 Functional Electrode. *Thin Solid Films* **2018**, *649*, 225–231.

Aljohani, T. A.; Almutairi, A. K. High Photoconversion Efficiency Obtained from Novel TiO2 Photoanodes. *Int. J. Electrochem. Sci.* **2016**, *11* (8), 6848–6861.

Allagui, A.; Alawadhi, H.; Alkaaby, M.; Gaidi, M.; Mostafa, K.; Abdulaziz, Y. Mott-Schottky Analysis of Flower-like ZnO Microstructures with Constant Phase Element Behavior. *Phys. Status Solidi Appl. Mater. Sci.* **2016**, *213* (1), 139–145.

Amano, F.; Mukohara, H.; Sato, H.; Ohno, T. Photoelectrochemical Water Vapor Splitting Using an Ionomer-Coated Rutile TiO2 Thin Layer on Titanium Microfiber Felt as an Oxygen-Evolving Photoanode. *Sustain. Energy Fuels* **2019**, *3* (8), 2048–2055.

Ambade, S. B.; Ambade, R. B.; Lee, W.; Mane, R. S.; Yoon, S. C.; Lee, S.-H. Development of Highly Transparent Seedless ZnO Nanorods Engineered for Inverted Polymer Solar Cells. *Nanoscale* **2014**, *6* (20), 12130–12141.

An, X.; Hu, C.; Liu, H.; Qu, J. Hierarchical Nanotubular Anatase/Rutile/TiO2(B) Heterophase Junction with Oxygen Vacancies for Enhanced Photocatalytic H2 Production. *Langmuir* **2018**, *34* (5), 1883–1889.

An, X.; Hu, C.; Liu, H.; Qu, J. Oxygen Vacancy Mediated Construction of Anatase/Brookite Heterophase Junctions for High-Efficiency Photocatalytic Hydrogen Evolution. *J. Mater. Chem. A* **2017**, *5* (47), 24989–24994.

Anuratha, K. S.; Lakshminarasimhan, N. Role of Synthesis Medium of TiO2 Nanoparticles in Enhancing the Open Circuit Voltage and Efficiency in Dye-Sensitized Solar Cell. *J. Solid State Electrochem.* **2014**, *18* (12), 3407–3414.

Aponsu, G. M. L. P.; Wijayarathna, T. R. C. K.; Perera, I. K.; Perera, V. P. S.; Siriwardhana, A. C. P. K. The Enhancement of Photovoltaic Parameters in Dye-Sensitized Solar Cells of Nano-Crystalline SnO2 by Incorporating with Large SrTiO3 Particles. *Spectrochim. Acta - Part A Mol. Biomol. Spectrosc.* **2013**, *109*, 37–41.

Aquino, J. M.; Silva, J. P.; Rocha-Filho, R. C.; Biaggio, S. R.; Bocchi, N. Comparison between Microwave and Muffle Annealing of Self-Organized TiO2 Nanotubes into Crystalline Anatase. *Mater. Lett.* **2016**, *167*, 209–212.

Aragon, A. G.; Kierulf-Vieira, W.; Łęcki, T.; Zarębska, K.; Widera-Kalinowska, J.; Skompska, M. Synthesis and Application of N-Doped TiO2/CdS/Poly(1,8-Diaminocarbazole) Composite for Photocatalytic Degradation of 4-Chlorophenol under Visible Light. *Electrochim. Acta* **2019**, *314*, 73–80.

Aslam, M.; Qamar, M. T.; Ali, S.; Rehman, A. U.; Soomro, M. T.; Ahmed, I.; Ismail, I. M. I.; Hameed, A. Evaluation of SnO2 for Sunlight Photocatalytic Decontamination of Water. *J. Environ. Manage.* **2018**, *217*, 805–814.

Bahadur, L.; Pandey, J. P. Photoelectrochemical Studies of Sprayed Thin Film N-ZnO/Acetonitrile Based Photocell Sensitized by Rhodamine B. *Indian J. Chem. Technol.* **1994**, *1* (1), 53–59.

Bahadur, L.; Rao, T. N. Photoelectrochemical Investigations on Particulate ZnO Thin Film Electrodes in Non-Aqueous Solvents. *J. Photochem. Photobiol. A Chem.* **1995**, *91* (3), 233–240.

Bahadur, L.; Roy, L. Spectral Sensitization of a Sprayed ZnO Thin Film Electrode by a New Synthetic Dye (2-Imidazolin-5-One) in Acetonitrile Medium. *Semicond. Sci. Technol.* **1995**, *10* (3), 358–364.

Bai, S.; Fu, H.; Zhao, Y.; Tian, K.; Luo, R.; Li, D.; Chen, A. On the Construction of Hollow Nanofibers of ZnO-SnO2 Heterojunctions to Enhance the NO2 Sensing Properties. *Sensors Actuators, B Chem.* **2018**, *266*, 692–702.

Baka, O.; Azizi, A.; Velumani, S.; Schmerber, G.; Dinia, A. Effect of Al Concentrations on the Electrodeposition and Properties of Transparent Al-Doped ZnO Thin Films. *J. Mater. Sci. Mater. Electron.* **2014**, *25* (4), 1761–1769.

Baka, O.; Khelladi, M. R.; Azizi, A. Effect of Al Doping on the Properties of Electrodeposited ZnO Nanostructures. *J. New Technol. Mater.* **2014**, *4* (1), 62–67.

Bakr, Z. H.; Wali, Q.; Ismail, J.; Elumalai, N. K.; Uddin, A.; Jose, R. Synergistic Combination of Electronic and Electrical Properties of SnO2 and TiO2 in a Single SnO2-TiO2 Composite Nanofiber for Dye-Sensitized Solar Cells. *Electrochim. Acta* **2018**, *263*, 524–532.

Bakr, Z. H.; Wali, Q.; Yang, S.; Yousefsadeh, M.; Padmasree, K. P.; Ismail, J.; Ab Rahim, M. H.; Yusoff, M. M.; Jose, R. Characteristics of ZnO-SnO 2 Composite Nanofibers as a Photoanode in Dye-Sensitized Solar Cells. *Ind. Eng. Chem. Res.* **2019**, *58* (2), 643–653.

Ballestas-Barrientos, A.; Li, X.; Yick, S.; Yuen, A.; Masters, A. F.; Maschmeyer, T. Interactions of Plasmonic Silver Nanoparticles with High Energy Sites on Multi-Faceted Rutile TiO2 Photoanodes. *ChemCatChem* **2020**, *12* (2), 469–477.

Bandara, J.; Pradeep, U. W. Tuning of the Flat-Band Potentials of Nanocrystalline TiO2 and SnO2 Particles with an Outer-Shell MgO Layer. *Thin Solid Films* **2008**, *517* (2), 952–956.

Bandara, J.; Pradeep, U. W. Variation of Flatband Potential of Oxide Nanocrystalline Particles with Core-Shell Structured Semiconductor-MgO Composites. *Sri Lankan J. Phys.* **2006**, *7*, 23–28.

Bandara, J.; Ranasinghe, R. A. S. S. The Effect of MgO Coating on Photocatalytic Activity of SnO2 for the Degradation of Chlorophenol and Textile Colorants; the Correlation between the Photocatalytic Activity and the Negative Shift of Flatband Potential of SnO2. *Appl. Catal. A Gen.* **2007**, *319*, 58–63.

Bandara, J.; Udawatta, C. P. K.; Rajapakse, C. S. K. Highly Stable CuO Incorporated TiO2 Catalyst for Photocatalytic Hydrogen Production from H2O. *Photochem. Photobiol. Sci.* **2005**, *4* (11), 857–861.

Baran, E.; Baz, Z.; Esen, R.; Yazici Devrim, B. TiO2-NT Electrodes Modified with Ag and Diamond like Carbon (DLC) for Hydrogen Production by Alkaline Water Electrolysis. *Appl. Surf. Sci.* **2017**, *420*, 416–428.

Baran, E.; Yazici, B. Fabrication of TiO2-NTs and TiO2-NTs Covered Honeycomb Lattice and Investigation of Carrier Densities in I-/I3- Electrolyte by Electrochemical Impedance Spectroscopy. *Appl. Surf. Sci.* **2015**, *357*, 2206–2216.

Belhadi, A.; Nadjem, I.; Zaidat, S.; Boudjemaa, A.; Trari, M. Hydrogen Evolution Under Visible Light Over the Heterojunction P-CuO/ZnO Prepared by Impregnation Method. *Int. J. Energy Res.* **2015**, *39*, 1909–1916.

Ben Naceur, J.; Ouertani, R.; Chakhari, W.; Chtourou, R. Photo-Electrochemical Properties of Sb 2 S 3 /TiO 2 Heterostructures Integrally Synthesis by Hydrothermal Method. *J. Mater. Sci. Mater. Electron.* **2019**, *30* (6), 5631–5639.

Bengas, R.; Lahmar, H.; Redha, K. M.; Mentar, L.; Azizi, A.; Schmerber, G.; Dinia, A. Electrochemical Synthesis of N-Type ZnS Layers on p-Cu2O/n-ZnO Heterojunctions with Different Deposition Temperatures. *RSC Adv.* **2019**, *9* (50), 29056–29069.

Benlarbi, M.; Farre, C.; Chaix, C.; Lawrence, M. F.; Blum, L. J.; Lysenko, V.; Marquette, C. A. Semiconducting Properties of Thin Films with Embedded Nanoparticles. *Synth. Met.* **2010**, *160* (23–24), 2675–2680.

Berghe, R. A. L.; Gomes, W. P. A Comparative Study of Electron Injection into ZnO, CdS and CdSe Single Crystal Anodes. *Berichte der Bunsengesellschaft für Phys. Chemie* **1972**, *76* (6), 481–485.

Bicelli, L. P.; Pedeferri, P.; Razzini, G. Anodically Oxidized Titanium Films to Be Used as Electrodes in Photoelectrolysis Solar Cells. *Int. J. Hydrogen Energy* **1986**, *11* (10), 647–651.

Biesmans, G.; Van Der Auweraer, M.; Cathry, C.; Meerschaut, D.; De Schryver, F. C.; Storck, W.; Willig, F. Photosensitized Electron Injection from Xanthene Dyes Incorporated in Langmuir-Blodgett Films into SnO2 Electrodes. *J. Phys. Chem.* **1991**, *95* (9), 3771–3779.

Biswas, I.; Majumder, M.; Roy, P.; Mukherjee, D.; Chakraborty, A. K. Nanostructured ZnO Thin Film with Improved Optical and Electrochemical Properties Prepared by Hydrothermal Electrochemical Deposition Technique. *Micro Nano Lett.* **2016**, *11* (7), 351–355.

Bloh, J. Z.; Dillert, R.; Bahnemann, D. W. Ruthenium-Modified Zinc Oxide, a Highly Active Vis-Photocatalyst: The Nature and Reactivity of Photoactive Centres. *Phys. Chem. Chem. Phys.* **2014**, *16* (12), 5833–5845.

Bohe, A. E.; Vilche, J. R.; Jüttner, K.; Lorenz, W. J.; Kautek, W.; Paatasch, W. An Electrochemical Impedance Spectroscopy Study of Passive Zinc and Low Alloyed Zinc Electrodes in Alkaline and Neutral Aqueous Solutions. *Corros. Sci.* **1991**, *32* (5–6), 621–633.

Bohe, A. E.; Vilche, J. R.; Jüttner, K.; Lorenz, W. J.; Paatsch, W. Investigations of the Semiconductor Properties of Anodically Formed Passive Layers on Zn and of ZnO Single Crystals in Different Aqueous Electrolytes by EIS. *Electrochim. Acta* **1989**, *34* (10), 1443–1448.

Bolts, J. M.; Wrighton, M. S. Correlation of Photocurrent-Voltage Curves with Flat-Band Potential for Stable Photoelectrodes for the Photoelectrolysis of Water. *J. Phys. Chem.* **1976**, *80* (24), 2641–2645.

Bondarenko, E. A.; Mazanik, A. V.; Streltsov, E. A.; Kulak, A. I.; Korolik, O. V. SnO2/Reduced Graphene Oxide Composite Films for Electrochemical Applications. *Mater. Sci. Eng. B Solid-State Mater. Adv. Technol.* **2015**, *202*, 61–67.

Boschloo, G. K. Photoelectrochemical Study of Thin Anatase TiO2 Films Prepared by Metallorganic Chemical Vapor Deposition. *J. Electrochem. Soc.* **1997**, *144* (4), 1311–1317.

Bu, Y.; Chen, Z. Highly Efficient Photoelectrochemical Anticorrosion for 304 Stainless Steel by C3N4@ZnO Composite with Quasi-Shell-Core Structure. *RSC Adv.* **2014**, *4* (85), 45397–45406.

Butler, M. A.; Abramovich, M.; Decker, F.; Julião, J. F. Subband Gap Response of TiO2 and SrTiO3 Photoelectrodes. *J. Electrochem. Soc.* **1981**, *128* (1), 200–204.

Butler, M. A.; Ginley, D. S. Temperature Dependence of Flatband Potentials at Semiconductor-Electrolyte Interfaces. *Nature* **1978**, *273* (5663), 524–525.

Cai, C.; Xu, Y. F.; Chen, H. Y.; Wang, X. D.; Kuang, D. Bin. Porous ZnO@ZnSe Nanosheet Array for Photoelectrochemical Reduction of CO2. *Electrochim. Acta* **2018**, *274*, 298–305.

Cai, H.; Yang, Q.; Hu, Z.; Duan, Z.; You, Q.; Sun, J.; Xu, N.; Wu, J. Enhanced Photoelectrochemical Activity of Vertically Aligned ZnO-Coated TiO2 Nanotubes. *Appl. Phys. Lett.* **2014**, *104* (5), 053114.

Cai, Y.; Kozhummal, R.; Kübel, C.; Trouillet, V.; Bruns, M.; Gutsch, S.; Zacharias, M.; Yang, Y. Spatial Separation of Photogenerated Electron-Hole Pairs in Solution-Grown ZnO Tandem n-p Core-Shell Nanowire Arrays toward Highly Sensitive Photoelectrochemical Detection of Hydrogen Peroxide. *J. Mater. Chem. A* **2017**, *5* (27), 14397–14405.

Cao, F.; Xiong, J.; Wu, F.; Liu, Q.; Shi, Z.; Yu, Y.; Wang, X.; Li, L. Enhanced Photoelectrochemical Performance from Rationally Designed Anatase/Rutile TiO2 Heterostructures. *ACS Appl. Mater. Interfaces* **2016**, *8* (19), 12239–12245.

Carrasco-Jaim, O. A.; Ceballos-Sanchez, O.; Torres-Martínez, L. M.; Moctezuma, E.; Gómez-Solís, C. Synthesis and Characterization of PbS/ZnO Thin Film for Photocatalytic Hydrogen Production. *J. Photochem. Photobiol. A Chem.* **2017**, *347*, 98–104.

Castro, I. A.; Byzynski, G.; Dawson, M.; Ribeiro, C. Charge Transfer Mechanism of WO3/TiO2 Heterostructure for Photoelectrochemical Water Splitting. *J. Photochem. Photobiol. A Chem.* **2017**, *339*, 95–102.

Cembrero-Coca, P.; Mollar, M.; Singh, K. C.; Marí, B. Effective Electrochemical N-Type Doping of ZnO Thin Films for Optoelectronic Window Applications. ECS *J. Solid State Sci. Technol.* **2013**, *2* (7), Q108–Q112.

Ceraj-Cerić, M.; Metikoš-Huković, M. Photoelectrochemical Properties of Polycrystalline TiO2 Electrodes: Anomalous Photoeffects. *Surf. Technol.* **1985**, *24* (3), 285–292.

Chan, Y. F.; Wang, C. C.; Chen, B. H.; Chen, C. Y. Incorporation of Plasma-Functionalized Carbon Nanocapsules into a Nanocrystalline TiO2 Photoanode for Use in Dye-Sensitized Solar Cells. *Carbon N. Y.* **2011**, *49* (14), 4898–4910.

Chandra Babu, K. S.; Singh, D.; Srivastava, O. N. Investigations on the Mixed Oxide Material TiO2-In 2O3 in Regard to Photoelectrolytic Hydrogen Production. *Semicond. Sci. Technol.* **1990**, *5* (4), 364–368.

Chaudhary, D.; Singh, S.; Vankar, V. D.; Khare, N. ZnO Nanoparticles Decorated Multi-Walled Carbon Nanotubes for Enhanced Photocatalytic and Photoelectrochemical Water Splitting. *J. Photochem. Photobiol. A Chem.* **2018**, *351*, 154–161.

Chen, H.; Zhu, W.; Zhang, Z.; Cai, W.; Zhou, X. Er and Mg Co-Doped TiO2 Nanorod Arrays and Improvement of Photovoltaic Property in Perovskite Solar Cell. *J. Alloys Compd.* **2019**, *771*, 649–657.

Chen, J.; Ruther, R. E.; Tan, Y.; Bishop, L. M.; Hamers, R. J. Molecular Adsorption on ZnO(10$\bar{1}$0) Single-Crystal Surfaces: Morphology and Charge Transfer. *Langmuir* **2012**, *28* (28), 10437–10445.

Chen, W.; Yu, S.; Zhong, Y.; Fan, X. B.; Wu, L. Z.; Zhou, Y. Effect of Electron Transfer on the Photocatalytic Hydrogen Evolution Efficiency of Faceted TiO2/CdSe QDs under Visible Light. *New J. Chem.* **2018**, *42* (7), 4811–4817.

Chen, Y. L.; Chen, Y. H.; Chen, J. W.; Cao, F.; Li, L.; Luo, Z. M.; Leu, I. C.; Pu, Y. C. New Insights into the Electron-Collection Efficiency Improvement of CdS-Sensitized TiO 2 Nanorod Photoelectrodes by Interfacial Seed-Layer Mediation. *ACS Appl. Mater. Interfaces* **2019**, *11* (8), 8126–8137.

Cheng, C.; Sun, Y. Carbon Doped TiO2 Nanowire Arrays with Improved Photoelectrochemical Water Splitting Performance. *Appl. Surf. Sci.* **2012**, *263*, 273–276.

Cheng, X. F.; Leng, W. H.; Liu, D. P.; Xu, Y. M.; Zhang, J. Q.; Cao, C. N. Electrochemical Preparation and Characterization of Surface-Fluorinated TiO2 Nanoporous Film and Its Enhanced Photoelectrochemical and Photocatalytic Properties. *J. Phys. Chem. C* **2008**, *112* (23), 8725–8734.

Cheng, X.; Liu, H.; Chen, Q.; Li, J.; Wang, P. Preparation and Characterization of Palladium Nano-Crystallite Decorated TiO2 Nano-Tubes Photoelectrode and Its Enhanced Photocatalytic Efficiency for Degradation of Diclofenac. *J. Hazard. Mater.* **2013**, *254–255*, 141–148.

Chiu, Y. H.; Chang, K. Der; Hsu, Y. J. Plasmon-Mediated Charge Dynamics and Photoactivity Enhancement for Au-Decorated ZnO Nanocrystals. *J. Mater. Chem. A* **2018**, *6* (10), 4286–4296.

Choi, J.; Song, J. T.; Jang, H. S.; Choi, M. J.; Sim, D. M.; Yim, S.; Lim, H.; Jung, Y. S.; Oh, J. Interfacial Band-Edge Engineered TiO2 Protection Layer on Cu2O Photocathodes for Efficient Water Reduction Reaction. *Electron. Mater. Lett*. **2017**, *13* (1), 57–65.

Choi, M.; Lim, J.; Baek, M.; Choi, W.; Kim, W.; Yong, K. Investigating the Unrevealed Photocatalytic Activity and Stability of Nanostructured Brookite TiO2 Film as an Environmental Photocatalyst. *ACS Appl. Mater. Interfaces* **2017**, *9* (19), 16252–16260.

Chou, J. C.; Yang, M. H.; Liao, J. W.; Lee, C. Y.; Gan, J. Y. Photoexcitation of TiO2 Photoanode in Water Splitting. *Mater. Chem. Phys.* **2014**, *143* (3), 1417–1422.

Choudhary, S.; Solanki, A.; Sharma, D.; Singh, N.; Upadhyay, S.; Shrivastav, R.; Satsangi, V. R.; Dass, S. Photoelectrochemical Water Splitting Using Bilayered ZnO/SrTiO3 Photoelectrodes. *Int. J. Mod. Phys. Conf. Ser.* **2013**, *22*, 545–551.

Chu, L.; Zhang, J.; Wu, Z.; Wang, C.; Sun, Y.; Dong, S.; Sun, J. Solar-Driven Photocatalytic Removal of Organic Pollutants over Direct Z-Scheme Coral-Branch Shape Bi2O3/SnO2 Composites. *Mater. Charact.* **2020**, *159*, 110036.

Clark, W. D. K.; Sutin, N. Spectral Sensitization of N-Type TiO2 Electrodes by Polypyridineruthenium(II) Complexes. *J. Am. Chem. Soc.* **1977**, *99* (14), 4676–4682.

Cooper, G. Mott-Schottky Plots and Flatband Potentials for Single Crystal Rutile Electrodes. *J. Electrochem. Soc.* **1982**, *129* (9), 1973–1977.

Daideche, K.; Azizi, A. Electrodeposition of Tin Oxide Thin Film from Nitric Acid Solution: The Role of PH. *J. Mater. Sci. Mater. Electron.* **2017**, *28* (11), 8051–8060.

Daniele, S.; Battistel, D.; Gerbasi, R.; Benetollo, F.; Battiston, S. Titania-Coated Platinum Thin Films by MOCVD: Electrochemical and Photoelectrochemical Properties. *Chem. Vap. Depos.* **2007**, *13* (11), 644–650.

Danzfuss, B.; Stimming, U. Iron(III)-Titanium(IV)-Oxide Electrodes: Their Structural, Electrochemical, and Photoelectrochemical Properties. *J. Electroanal. Chem.* **1984**, *164*, 89–119.

Dare-Edwards, M. P.; Hamnett, A. A Novel Surface Preparation for Single-Crystal TiO2 and Its Characterisation by Photocurrent-Voltage Measurements. *J. Electroanal. Chem.* **1979**, *105* (2), 283–290.

de Wit, A. R.; Janssen, M. D.; Kelly, J. J. Electrochemical Characterization of Polycrystalline ZnO Layers. *Appl. Surf. Sci.* **1990**, *45* (1), 21–27.

Dewald, J. F. The Charge and Potential Distributions at the Zinc Oxide Electrode. *Bell Syst. Tech. J.* **1960**, *39* (3), 615–639.

Dhandayuthapani, T.; Sivakumar, R.; Ilangovan, R.; Gopalakrishnan, C.; Sanjeeviraja, C.; Jeyadheepan, K. Eco-Friendly Nebulized Spray Deposition of Bifunctional Anatase TiO2 Thin Films Exhibiting Multicolor Switching and Efficient NH3 Gas Sensing at Room Temperature. *Mater. Res. Express* **2019**, *6* (6), 065053.

Di Paola, A.; Bellardita, M.; Ceccato, R.; Palmisano, L.; Parrino, F. Highly Active Photocatalytic TiO2 Powders Obtained by Thermohydrolysis of TiCl4 in Water. *J. Phys. Chem. C* **2009**, *113* (34), 15166–15174.

Diaz-Real, J. A.; Elsaesser, P.; Holm, T.; Mérida, W. Electrochemical Reduction on Nanostructured TiO2 for Enhanced Photoelectrocatalytic Oxidation. *Electrochim. Acta* **2020**, *329*, 135162.

Diby, N. D.; Duan, Y.; Grah, P. A.; Cai, F.; Yuan, Z. Enhanced Photoelectrochemical Performance for Hydrogen Generation via Introducing Ti3+ and Oxygen Vacancies into TiO2 Nanorod Arrays. *J. Mater. Sci. Mater. Electron.* **2018**, *29* (23), 20236–20246.

Dom, R.; Baby, L. R.; Kim, H. G.; Borse, P. H. Enhanced Solar Photoelectrochemical Conversion Efficiency of ZnO:Cu Electrodes for Water-Splitting Application. *Int. J. Photoenergy* **2013**, *2013*, 928321.

Dom, R.; Govindarajan, S.; Joshi, S. V.; Borse, P. H. A Solar-Responsive Zinc Oxide Photoanode for Solar-Photon-Harvester Photoelectrochemical (PEC) Cells. *Nanoscale Adv.* **2020**, Advance Article.

Dom, R.; Kim, H. G.; Borse, P. H. Efficient Hydrogen Generation over (100)-Oriented ZnO Nanostructured Photoanodes under Solar Light. *CrystEngComm* **2014**, *16* (12), 2432–2439.

Dong, S.; Cui, L.; Tian, Y.; Xia, L.; Wu, Y.; Yu, J.; Bagley, D. M.; Sun, J.; Fan, M. A Novel and High-Performance Double Z-Scheme Photocatalyst ZnO-SnO2-Zn2SnO4 for Effective Removal of the Biological Toxicity of Antibiotics. *J. Hazard. Mater.* **2020**, *399*, 123017.

Dong, Z.; Ding, D.; Li, T.; Ning, C. Facile Preparation of Ti3+/Ni Co-Doped TiO2 Nanotubes Photoanode for Efficient Photoelectrochemical Water Splitting. *Appl. Surf. Sci.* **2019**, *480*, 219–228.

Dridi, D.; Bouaziz, L.; Karyaoui, M.; Litaiem, Y.; Chtourou, R. Effect of Silver Doping on Optical and Electrochemical Properties of ZnO Photoanode. *J. Mater. Sci. Mater. Electron.* **2018**, *29* (10), 8267–8278.

Duan, Y.; Fu, N.; Liu, Q.; Fang, Y.; Zhou, X.; Zhang, J.; Lin, Y. Sn-Doped TiO2 Photoanode for Dye-Sensitized Solar Cells. *J. Phys. Chem. C* **2012**, *116* (16), 8888–8893.

Duan, Y.; Fu, N.; Zhang, Q.; Fang, Y.; Zhou, X.; Lin, Y. Influence of Sn Source on the Performance of Dye-Sensitized Solar Cells (Based on Sn-Doped TiO2 Photoanodes: A Strategy for Choosing an Appropriate Doping Source. *Electrochim. Acta* **2013**, *107*, 473–480.

Duan, Y.; Liang, L.; Lv, K.; Li, Q.; Li, M. TiO2 Faceted Nanocrystals on the Nanofibers: Homojunction TiO2 Based Z-Scheme Photocatalyst for Air Purification. *Appl. Surf. Sci.* **2018**, *456*, 817–826.

Duan, Y.; Zheng, J.; Fu, N.; Fang, Y.; Liu, T.; Zhang, Q.; Zhou, X.; Lin, Y.; Pan, F. Enhancing the Performance of Dye-Sensitized Solar Cells: Doping SnO2 Photoanodes with Al to Simultaneously Improve Conduction Band and Electron Lifetime. *J. Mater. Chem. A* **2015**, *3* (6), 3066–3073.

Dukštienė, N.; Sinkevičiūtė, D.; Tatariškinaitė, L. Electrochemical Behavior of SeO2 in Sodium Citrate Solution on a Polycrystalline SnO2 Electrode. *J. Solid State Electrochem.* **2016**, *20* (3), 813–825.

Durán-Álvarez, J. C.; Santiago, A. L.; Ramírez-Ortega, D.; Acevedo-Peña, P.; Castillón, F.; Ramírez-Zamora, R. M.; Zanella, R. Surface Modification of B–TiO2 by Deposition of Au Nanoparticles to Increase Its Photocatalytic Activity under Simulated Sunlight Irradiation. *J. Sol-Gel Sci. Technol.* **2018**, *88* (2), 474–487.

Dursun, S.; Kaya, I. C.; Kalem, V.; Akyildiz, H. UV/Visible Light Active CuCrO2 Nanoparticle-SnO2 Nanofiber p-n Heterostructured Photocatalysts for Photocatalytic Applications. *Dalt. Trans.* **2018**, *47* (41), 14662–14678.

Dutoit, E. C.; Cardon, F.; Gomes, W. P. Electrochemical Properties of the Semiconducting TiO2 (Rutile) Single Crystal Electrode. *Berichte der Bunsengesellschaft/Physical Chem. Chem. Phys.* **1976**, *80* (6), 475–481.

Dutoit, E. C.; Cardon, F.; Gomes, W. P. Electrochemical Reactions Involving Holes at the Illuminated TiO2 (Rutile) Single Crystal Electrode. *Berichte der Bunsengesellschaft/Physical Chem. Chem. Phys.* **1976**, *80* (12), 1285–1288.

Egelhaaf, H. J.; Oelkrug, D. Luminescence and Nonradiative Deactivation of Excited States Involving Oxygen Defect Centers in Polycrystalline ZnO. *J. Cryst. Growth* **1996**, *161*, 190–194.

El-Taib Heakal, F.; Abd-Ellatif, W. R.; Tantawy, N. S.; Taha, A. A. Characterization of Electrodeposited Undoped and Doped Thin ZnO Passive Films on Zinc Metal in Alkaline HCO3−/CO32− Buffer Solution. *RSC Adv.* **2018**, *8* (69), 39321–39333.

Elhag, S.; Khun, K.; Khranovskyy, V.; Liu, X.; Willander, M.; Nur, O. Efficient Donor Impurities in ZnO Nanorods by Polyethylene Glycol for Enhanced Optical and Glutamate Sensing Properties. *Sensors* **2016**, *16* (2), 222.

Enache, C. S.; Schoonman, J.; Van De Krol, R. The Photoresponse of Iron- and Carbon-Doped TiO2 (Anatase) Photoelectrodes. *J. Electroceramics* **2004**, *13*, 177–182.

Fang, W. Q.; Wang, X. L.; Zhang, H.; Jia, Y.; Huo, Z.; Li, Z.; Zhao, H.; Yang, H. G.; Yao, X. Manipulating Solar Absorption and Electron Transport Properties of Rutile TiO2 Photocatalysts via Highly N-Type F-Doping. *J. Mater. Chem. A* **2014**, *2* (10), 3513–3520.

Fichou, D.; Pouliquen, J.; Kossanyi, J.; Jakani, M.; Campet, G.; Claverie, J. Extension of the Photoresponse of Semiconducting Zinc Oxide Electrodes by 3d-Impurities Absorbing in the Visible Region of the Solar Spectrum. *J. Electroanal. Chem.* **1985**, *188* (1–2), 167–187.

Finklea, H. O. The Preparation of Ti02 Electrodes with Minimum Mott-Schottky Frequency Dispersion. *J. Electrochem. Soc.* **1982**, *129* (9), 2003–2008.

Finklea, H. O.; Murray, R. W. Chemically Modified Electrodes. 12. Effects of Silanization on Titanium Dioxide Electrodes. *J. Phys. Chem.* **1979**, *83* (3), 353–358.

Frade, T.; Siopa, D.; Martins, A. F.; Carreira, J. F. C.; Rodrigues, J.; Sedrine, N. Ben; Correia, M. R.; Monteiro, T.; Tena-Zaera, R.; Gomes, A. Optoelectronic Characterization of ZnO Nanorod Arrays Obtained by Pulse Electrodeposition. *J. Electrochem. Soc.* **2018**, *165* (13), D595–D603.

Fraoucene, H.; Hatem, D.; Vacandio, F.; Pasquinelli, M. TiO2 Nanotubes with Nanograss Structure: The Effect of the Anodizing Voltage on the Formation Mechanism and Structure Properties. *J. Electron. Mater.* **2019**, *48* (4), 2046–2054.

Fu, X.; Wang, J.; Huang, D.; Meng, S.; Zhang, Z.; Li, L.; Miao, T.; Chen, S. Trace Amount of SnO2-Decorated ZnSn(OH)6 as Highly Efficient Photocatalyst for Decomposition of Gaseous Benzene: Synthesis, Photocatalytic Activity, and the Unrevealed Synergistic Effect between ZnSn(OH)6 and SnO2. *ACS Catal.* **2016**, *6* (2), 957–968.

Fujishima, A.; Honda, K. Electrochemical Photolysis of Water at a Semiconductor Electrode. *Nature* **1972**, *238*, 37–38. https://doi.org/10.1038/238038a0.

Game, O.; Singh, U.; Gupta, A. A.; Suryawanshi, A.; Banpurkar, A.; Ogale, S. Concurrent Synthetic Control of Dopant (Nitrogen) and Defect Complexes to Realize Broadband (UV-650 Nm) Absorption in ZnO Nanorods for Superior Photo-Electrochemical Performance. *J. Mater. Chem.* **2012**, *22* (33), 17302–17310.

Gan, W.; Zhang, J.; Niu, H.; Bao, L.; Hao, H.; Yan, Y.; Wu, K.; Fu, X. Fabrication of Ag/AgBr/TiO2 Composites with Enhanced Solar-Light Photocatalytic Properties. *Colloids Surfaces A Physicochem. Eng. Asp.* **2019**, *583*, 123968.

Ge, H.; Tian, H.; Zhou, Y.; Wu, S.; Liu, D.; Fu, X.; Song, X. M.; Shi, X.; Wang, X.; Li, N. Influence of Surface States on the Evaluation of the Flat Band Potential of TiO2. *ACS Appl. Mater. Interfaces* **2014**, *6* (4), 2401–2406.

Gelderman, K.; Lee, L.; Donne, S. W. Flat-Band Potential of a Semiconductor: Using the Mott-Schottky Equation. *J. Chem. Educ.* **2007**, *84* (4), 685–688.

Gervasi, C. A.; Folquer, M. E.; Vallejo, A. E.; Alvarez, P. E. Electron Transfer across Anodic Films Formed on Tin in Carbonate-Bicarbonate Buffer Solution. *Electrochim. Acta* **2005**, *50* (5), 1113–1119.

Ghobadi, A.; Ghobadi, T. G. U.; Karadas, F.; Ozbay, E. Angstrom Thick ZnO Passivation Layer to Improve the Photoelectrochemical Water Splitting Performance of a TiO2 Nanowire Photoanode: The Role of Deposition Temperature. *Sci. Rep.* **2018**, *8*, 16322.

Ginley, D. S.; Knotek, M. L. Hydrogen in TiO2 Photoanodes. *J. Electrochem. Soc.* **1979**, *126* (12), 2163–2166.

Giorgi, L.; Salernitano, E.; Dikonimos Makris, T.; Giorgi, R.; Leoni, E.; Grilli, M. L.; Lisi, N. Titania Nanotubes Self-Assembled by Electrochemical Anodization: Semiconducting and Electrochemical Properties. *Thin Solid Films* **2016**, *601*, 28–34.

Goossens, A. Intensity-Modulated Photocurrent Spectroscopy of Thin Anodic Films on Titanium. *Surf. Sci.* **1996**, *365* (3), 662–671.

Gu, W.; Lu, F.; Wang, C.; Kuga, S.; Wu, L.; Huang, Y.; Wu, M. Face-to-Face Interfacial Assembly of Ultrathin g-C3N4 and Anatase TiO2 Nanosheets for Enhanced Solar Photocatalytic Activity. *ACS Appl. Mater. Interfaces* **2017**, *9* (34), 28674–28684.

Gubbala, S.; Chakrapani, V.; Kumar, V.; Sunkara, M. K. Band-Edge Engineered Hybrid Structures for Dye-Sensitized Solar Cells Based on SnO2 Nanowires. *Adv. Funct. Mater.* **2008**, *18* (16), 2411–2418.

Guerrero-Araque, D.; Ramírez-Ortega, D.; Acevedo-Peña, P.; Tzompantzi, F.; Calderón, H. A.; Gómez, R. Interfacial Charge-Transfer Process across ZrO2-TiO2 Heterojunction and Its Impact on Photocatalytic Activity. *J. Photochem. Photobiol. A Chem.* **2017**, *335*, 276–286.

Guerrero-Araque, D.; Ramírez-Ortega, D.; Gómez, R.; Acevedo-Peña, P. Rapid Breakdown Anodization to Obtain Nanostructured TiO2 Powders for Photocatalytic Hydrogen Generation. *J. Mater. Sci. Mater. Electron.* **2017**, *28* (13), 9859–9866.

Gulino, D. A.; Faulkner, L. R.; Drickamer, H. G. High Pressure Photoelectric Studies of Semiconductor-Electrolyte Systems. *J. Appl. Phys.* **1983**, *54* (5), 2483–2488.

Gun, Y.; Song, G. Y.; Quy, V. H. V.; Heo, J.; Lee, H.; Ahn, K. S.; Kang, S. H. Joint Effects of Photoactive TiO2 and Fluoride-Doping on SnO2 Inverse Opal Nanoarchitecture for Solar Water Splitting. *ACS Appl. Mater. Interfaces* **2015**, *7* (36), 20292–20303.

Guo, Q.; Wu, J.; Yang, Y.; Liu, X.; Lan, Z.; Lin, J.; Huang, M.; Wei, Y.; Dong, J.; Jia, J.; Huang, Y. High-Performance and Hysteresis-Free Perovskite Solar Cells Based on Rare-Earth-Doped SnO 2 Mesoporous Scaffold. *Research* **2019**, *2019*, 4049793.

Gupta, M.; Sharma, V.; Shrivastava, J.; Solanki, A.; Singh, A. P.; Satsangi, V. R.; Dass, S.; Shrivastav, R. Preparation and Characterization of Nanostructured ZnO Thin Films for Photoelectrochemical Splitting of Water. *Bull. Mater. Sci.* **2009**, *32* (1), 23–30.

Gutierrez, C.; Salvador, P. Bandgap at the N-TiO2/Electrolyte Interface. *J. Electroanal. Chem.* **1982**, *138* (2), 457–463.

Gutiérrez, D. J. R.; Mathews, N. R.; Martínez, S. S. Photocatalytic Activity Enhancement of TiO2 Thin Films with Silver Doping under Visible Light. *J. Photochem. Photobiol. A Chem.* **2013**, *262*, 57–63.

Güy, N.; Özacar, M. Ag/Ag2CrO4 Nanoparticles Modified on ZnO Nanorods as an Efficient Plasmonic Photocatalyst under Visible Light. *J. Photochem. Photobiol. A Chem.* **2019**, *370*, 1–11.

Hahn, R.; Schmidt-Stein, F.; Sahnen, J.; Thiemann, S.; Song, Y.; Kunze, J.; Lehto, V. P.; Schmuki, P. Semimetallic TiO2 Nanotubes. *Angew. Chemie - Int. Ed.* **2009**, *48* (39), 7236–7239.

Haisch, C.; Günnemann, C.; Melchers, S.; Fleisch, M.; Schneider, J.; Emeline, A. V.; Bahnemann, D. W. Irreversible Surface Changes upon N-Type Doping – A Photoelectrochemical Study on Rutile Single Crystals. *Electrochim. Acta* **2018**, *280*, 278–289.

Hall, D. E.; Wildes, P. D.; Lichtin, N. N. Electrodic Phenomena at the Anode of the Totally Illuminated, Thin Layer Iron-Thionine Photogalvanic Cell. *J. Electrochem. Soc.* **1978**, *125* (9), 1365–1371.

Hamann, T. W.; Gstrein, F.; Brunschwig, B. S.; Lewis, N. S. Measurement of the Dependence of Interfacial Charge-Transfer Rate Constants on the Reorganization Energy of Redox Species at n-ZnO/H2O Interfaces. *J. Am. Chem. Soc.* **2005**, *127* (40), 13949–13954.

Hamann, T. W.; Gstrein, F.; Brunschwig, B. S.; Lewis, N. S. Measurement of the Driving Force Dependence of Interfacial Charge-Transfer Rate Constants in Response to PH Changes at n-ZnO/H2O Interfaces. *Chem. Phys.* **2006**, *326* (1), 15–23.

Hamnett, A.; Dare-Edwards, M. P.; Wright, R. D.; Seddon, K. R.; Goodenough, J. B. Photosensitization of Titanium(IV) Oxide with Tris(2,2′-Bipyridine)Ruthenium(II) Chloride. Surface States of Titanium(IV) Oxide. *J. Phys. Chem.* **1979**, *83* (25), 3280–3290.

Hamrouni, A.; Moussa, N.; Di Paola, A.; Palmisano, L.; Houas, A.; Parrino, F. Photocatalytic Activity of Binary and Ternary SnO2-ZnO-ZnWO4 Nanocomposites. *J. Photochem. Photobiol. A Chem.* **2015**, *309*, 47–54.

Hamrouni, A.; Moussa, N.; Parrino, F.; Di Paola, A.; Houas, A.; Palmisano, L. Sol-Gel Synthesis and Photocatalytic Activity of ZnO-SnO2 Nanocomposites. *J. Mol. Catal. A Chem.* **2014**, *390*, 133–141.

Han, Z.; Luo, M.; Chen, L.; Chen, J.; Li, C. A Photoelectrochemical Immunosensor for Detection of α-Fetoprotein Based on Au-ZnO Flower-Rod Heterostructures. *Appl. Surf. Sci.* **2017**, *402*, 429–435.

Handley, L. J.; Bard, A. J. Semiconductor Electrodes XXIII. The Determination of Flatband Potentials from Differential Stress Measurements with Attached Piezoelectric Detectors. *J. Electrochem. Soc.* **1980**, *127* (2), 338–343.

Hardee, K. L.; Bard, A. J. Semiconductor Electrodes X. Photoelectrochemical Behavior of Several Polycrystalline Metal Oxide Electrodes in Aqueous Solutions. *J. Electrochem. Soc.* **1975**, *124* (2), 215–224.

Hattori, A.; Tokihisa, Y.; Tada, H.; Tohge, N.; Ito, S.; Hongo, K.; Shiratsuchi, R.; Nogami, G. Patterning Effect of a Sol-Gel TiO2 Overlayer on the Photocatalytic Activity of a TiO2/SnO2 Bilayer-Type Photocatalyst. *J. Sol-Gel Sci. Technol.* **2001**, *22*, 53–61.

He, R.; Gu, X.; Zhao, Y.; Qiang, Y. Enhanced Visible-Light Photoelectrochemical Activity of TiO2 Nanorod Arrays Decorated by Sb2S3 Particles. *J. Mater. Sci. Mater. Electron.* **2018**, *29* (7), 5293–5298.

He, R.; Gu, X.; Zhao, Y.; Qiang, Y. Surface Modification of TiO2 Nanorod Arrays with Ag3PO4 @ PANI Nanoparticles for Enhancing Photoelectrochemical Performance. *Int. J. Nanomanuf.* **2019**, *15* (1–2), 158–169.

Heikkilä, M.; Puukilainen, E.; Ritala, M.; Leskelä, M. Effect of Thickness of ALD Grown TiO2 Films on Photoelectrocatalysis. *J. Photochem. Photobiol. A Chem.* **2009**, *204*, 200–208.

Hengerer, R.; Kavan, L.; Krtil, P.; Grätzel, M. Orientation Dependence of Charge-Transfer Processes on TiO2 (Anatase) Single Crystals. *J. Electrochem. Soc.* **2000**, *147* (4), 1467–1472.

Henni, A.; Karar, A. The Effects of Bath Temperature on the Zinc Oxide Properties Prepared by Electrochemical Deposition. *Mater. Biomater. Sci.* **2018**, *1*, 1–5.

Henni, A.; Merrouche, A.; Telli, L.; Karar, A.; Ezema, F. I.; Haffar, H. Optical, Structural, and Photoelectrochemical Properties of Nanostructured Ln-Doped ZnO via Electrodepositing Method. *J. Solid State Electrochem.* **2016**, *20* (8), 2135–2142.

Henni, A.; Merrouche, A.; Telli, L.; Walter, S.; Azizi, A.; Fenineche, N. Effect of H2O2 Concentration on Electrochemical Growth and Properties of Vertically Oriented ZnO Nanorods Electrodeposited from Chloride Solutions. *Mater. Sci. Semicond. Process.* **2015**, *40*, 585–590.

Hepel, T.; Hepel, M.; Osteryoung, R. A. Thermodynamic and Photoelectrochemical Behavior of the N-TiO2 Electrode in Fluoride-Containing Solutions. *J. Electrochem. Soc.* **1982**, *129* (9), 2132–2141.

Hezam, A.; Namratha, K.; Drmosh, Q. A.; Ponnamma, D.; Nagi Saeed, A. M.; Ganesh, V.; Neppolian, B.; Byrappa, K. Direct Z-Scheme Cs2O-Bi2O3-ZnO Heterostructures for Photocatalytic Overall Water Splitting. *J. Mater. Chem. A* **2018**, *6* (43), 21379–21388.

Hirano, T.; Kozuka, H. Photoanodic Properties of ZnO Thin Films Prepared from Zinc Acetate Solutions Containing Cobalt Acetate and Polyvinylpyrrolidone. *J. Mater. Sci.* **2003**, *38* (20), 4203–4210.

Hope, G. A.; Bard, A. J. Platinum/Titanium Dioxide (Rutile) Interface. Formation of Ohmic and Rectifying Junctions. *J. Phys. Chem.* **1983**, *87* (11), 1979–1984.

Houlihan, J. F.; Armitage, D. B.; Hoovler, T.; Bonaquist, D.; Madacsi, D. P.; Mulay, L. N. Doped Polycrystalline TiO2 Electrodes for the Photo-Assisted Electrolysis of Water. *Mater. Res. Bull.* **1978**, *13* (11), 1205–1212.

Hsu, Y. F.; Xi, Y. Y.; Djurišić, A. B.; Chan, W. K. ZnO Nanorods for Solar Cells: Hydrothermal Growth versus Vapor Deposition. *Appl. Phys. Lett.* **2008**, *92* (13), 133507.

Hsu, Y. K.; Chen, Y. C.; Lin, Y. G. Novel ZnO/Fe2O3 Core-Shell Nanowires for Photoelectrochemical Water Splitting. *ACS Appl. Mater. Interfaces* **2015**, *7* (25), 14157–14162.

Hsu, Y. K.; Lin, C. M. Enhanced Photoelectrochemical Properties of Ternary Zn1-XCuxO Nanorods with Tunable Band Gaps for Solar Water Splitting. *Electrochim. Acta* **2012**, *74*, 73–77.

Hu, S.; Shaner, M. R.; Beardslee, J. A.; Lichterman, M.; Brunschwig, B. S.; Lewis, N. S. Amorphous TiO2Coatings Stabilize Si, GaAs, and GaP Photoanodes for Efficient Water Oxidation. *Science* **2014**, *344* (6187), 1005–1009.

Huang, C. ying; Guo, R. tang; Pan, W. guo; Tang, J. ying; Zhou, W. guo; Liu, X. yu; Qin, H.; Jia, P. yao. One-Dimension TiO2 Nanostructures with Enhanced Activity for CO2 Photocatalytic Reduction. *Appl. Surf. Sci.* **2019**, *464*, 534–543.

Huang, H.; Li, D.; Lin, Q.; Shao, Y.; Chen, W.; Hu, Y.; Chen, Y.; Fu, X. Efficient Photocatalytic Activity of PZT/TiO2 Heterojunction under Visible Light Irradiation. *J. Phys. Chem. C* **2009**, *113* (32), 14264–14269.

Huang, H.; Li, D.; Lin, Q.; Zhang, W.; Shao, Y.; Chen, Y.; Sun, M.; Fu, X. Efficient Degradation of Benzene over LaVO4/TiO2 Nanocrystalline Heterojunction Photocatalyst under Visible Light Irradiation. *Environ. Sci. Technol.* **2009**, *43* (11), 4164–4168.

Huang, M. C.; Wang, T.; Wu, B. J.; Lin, J. C.; Wu, C. C. Anodized ZnO Nanostructures for Photoelectrochemical Water Splitting. *Appl. Surf. Sci.* **2016**, *360*, 442–450.

Huang, X.; Song, J.; Wang, L.; Gu, X.; Zhao, Y.; Qiang, Y. Photoelectrochemical Properties of ZnO/BiVO4 Nanorod Arrays Prepared through a Facile Spin-Coating Deposition Route. *Mater. Sci. Semicond. Process.* **2019**, *97*, 106–111.

Hyde, M.; Saterlay, A. J.; Wilkins, S. J.; Foord, J. S.; Compton, R. G.; Marken, F. Deposition and Characterisation of a Porous Sn(IV) Semiconductor Nanofilm on Boron-Doped Diamond. *J. Solid State Electrochem.* **2002**, *6* (3), 183–187.

Imahori, H.; Hayashi, S.; Umeyama, T.; Eu, S.; Oguro, A.; Kang, S.; Matano, Y.; Shishido, T.; Ngamsinlapasathian, S.; Yoshikawa, S. Comparison of Electrode Structures and Photovoltaic Properties of Porphyrin-Sensitized Solar Cells with TiO2 and Nb, Ge, Zr-Added TiO2 Composite Electrodes. *Langmuir* **2006**, *22* (26), 11405–11411.

Imanishi, A.; Okamura, T.; Ohashi, N.; Nakamura, R.; Nakato, Y. Mechanism of Water Photooxidation Reaction at Atomically Flat TiO 2 (Rutile) (110) and (100) Surfaces: Dependence on Solution PH. *J. Am. Chem. Soc.* **2007**, *129* (37), 11569–11578.

Inukai, J.; Ito, K.; Itaya, K. In Situ Electrochemical Scanning Tunneling Microscopy of Zinc-Terminated ZnO(0001) Single Crystal Electrode in Solution. *Electrochemistry* **1999**, *67* (12), 1126–1128.

Iqbal, M.; Wang, Y.; Hu, H.; He, M.; Hassan Shah, A.; Lin, L.; Li, P.; Shao, K.; Reda Woldu, A.; He, T. Cu2O-Tipped ZnO Nanorods with Enhanced Photoelectrochemical Performance for CO2 Photoreduction. *Appl. Surf. Sci.* **2018**, *443*, 209–216.

Iqbal, M.; Wang, Y.; Hu, H.; He, M.; Shah, A. H.; Li, P.; Lin, L.; Woldu, A. R.; He, T. Interfacial Charge Kinetics of ZnO/ZnTe Heterostructured Nanorod Arrays for CO2 Photoreduction. *Electrochim. Acta* **2018**, *272*, 203–211.

Irshad, A.; Munichandraiah, N. Photochemical Deposition of Co-Ac Catalyst on ZnO Nanorods for Solar Water Oxidation. *J. Electrochem. Soc.* **2015**, *162* (4), H235–H243.

Itaya, K.; Tomita, E. Scanning Tunneling Microscopy of Semiconductor (n-ZnO)/Liquid Interfaces Under Potentiostatic Conditions. *Surf. Sci. Lett.* **1989**, *219*, L515–L520.

Jana, S. K.; Majumder, T.; Banerjee, S. Enhanced Photoelectrochemical Property of Gold Nanoparticle Sensitized TiO2 Nanotube: A Crucial Investigation at Electrode-Electrolyte Interface. *J. Electroanal. Chem.* **2014**, *727*, 99–103.

Jeong, K.; Deshmukh, P. R.; Park, J.; Sohn, Y.; Shin, W. G. ZnO-TiO2 Core-Shell Nanowires: A Sustainable Photoanode for Enhanced Photoelectrochemical Water Splitting. *ACS Sustain. Chem. Eng.* **2018**, *6* (5), 6518–6526.

Jiang, X. H.; Xing, Q. J.; Luo, X. B.; Li, F.; Zou, J. P.; Liu, S. S.; Li, X.; Wang, X. K. Simultaneous Photoreduction of Uranium(VI) and Photooxidation of Arsenic(III) in Aqueous Solution over g-C3N4/TiO2 Heterostructured Catalysts under Simulated Sunlight Irradiation. *Appl. Catal. B Environ.* **2018**, *228*, 29–38.

Julião, J. F.; Decker, F.; Abramovich, M. Photoelectrolysis of Water with Natural Mineral TiO2 Rutile Electrodes. *J. Electrochem. Soc.* **1980**, *127* (10), 2264–2268.

Kandiel, T. A.; Ahmed, A. Y.; Bahnemann, D. TiO2(B)/Anatase Heterostructure Nanofibers Decorated with Anatase Nanoparticles as Efficient Photocatalysts for Methanol Oxidation. *J. Mol. Catal. A Chem.* **2016**, *425*, 55–60.

Kandiel, T. A.; Feldhoff, A.; Robben, L.; Dillert, R.; Bahnemann, D. W. Tailored Titanium Dioxide Nanomaterials: Anatase Nanoparticles and Brookite Nanorods as Highly Active Photocatalysts. *Chem. Mater.* **2010**, *22* (6), 2050–2060.

Kaneko, M.; Ueno, H.; Nemoto, J. Schottky Junction/Ohmic Contact Behavior of a Nanoporous TiO2 Thin Film Photoanode in Contact with Redox Electrolyte Solutions. *Beilstein J. Nanotechnol.* **2011**, *2* (1), 127–134.

Kang, D.; Lee, D.; Choi, K. S. Electrochemical Synthesis of Highly Oriented, Transparent, and Pinhole-Free ZnO and Al-Doped ZnO Films and Their Use in Heterojunction Solar Cells. *Langmuir* **2016**, *32* (41), 10459–10466.

Kang, S. H.; Kim, J. Y.; Kim, Y.; Kim, H. S.; Sung, Y. E. Surface Modification of Stretched TiO2 Nanotubes for Solid-State Dye-Sensitized Solar Cells. *J. Phys. Chem. C* **2007**, *111* (26), 9614–9623.

Kant, R.; Dwivedi, C.; Pathak, S.; Dutta, V. Fabrication of ZnO Nanostructures Using Al Doped ZnO (AZO) Templates for Application in Photoelectrochemical Water Splitting. *Appl. Surf. Sci.* **2018**, *447*, 200–212.

Kapusta, S.; Hackerman, N. Capacitive Studies of the Semiconducting Properties of Passive Tin Electrodes. *Electrochim. Acta* **1980**, *25* (7), 949–955.

Kar, P.; Zhang, Y.; Farsinezhad, S.; Mohammadpour, A.; Wiltshire, B. D.; Sharma, H.; Shankar, K. Rutile Phase N- and p-Type Anodic Titania Nanotube Arrays with Square-Shaped Pore Morphologies. *Chem. Commun.* **2015**, *51* (37), 7816–7819.

Karmakar, K.; Sarkar, A.; Mandal, K.; Khan, G. G. Nano-Engineering of p-n CuFeO2-ZnO Heterojunction Photoanode with Improved Light Absorption and Charge Collection for Photoelectrochemical Water Oxidation. *Nanotechnology* **2017**, *28* (32), 325401.

Karmakar, K.; Sarkar, A.; Mandal, K.; Khan, G. G. Stable and Enhanced Visible-Light Water Electrolysis Using C, N, and S Surface Functionalized ZnO Nanorod Photoanodes: Engineering the Absorption and Electronic Structure. *ACS Sustain. Chem. Eng.* **2016**, *4* (10), 5693–5702.

Katić, J.; Metikoš-Huković, M.; Šarić, I.; Petravić, M. Semiconducting Properties of the Oxide Films Formed on Tin: Capacitive and XPS Studies. *J. Electrochem. Soc.* **2016**, *163* (5), C221–C227.

Kaur, G.; Divya; Khan, S. A.; Satsangi, V. R.; Dass, S.; Shrivastav, R. Expanded Light-Absorption and Efficient Charge-Separation: Bilayered Thin Film Nano-Hetero-Structures, CuO/Cu–ZnO, Make Efficient Photoanode in Photoelectrochemical Water Splitting. *J. Appl. Electrochem.* **2020**, *50* (8), 887–906.

Kavan, L.; Grätzel, M. Highly Efficient Semiconducting TiO2 Photoelectrodes Prepared by Aerosol Pyrolysis. *Electrochim. Acta* **1995**, *40* (5), 643–652.

Kavan, L.; Grätzel, M.; Gilbert, S. E.; Klemenz, C.; Scheel, H. J. Electrochemical and Photoelectrochemical Investigation of Single-Crystal Anatase. *J. Am. Chem. Soc.* **1996**, *118* (28), 6716–6723.

Kavan, L.; O'Regan, B.; Kay, A.; Grätzel, M. Preparation of TiO2 (Anatase) Films on Electrodes by Anodic Oxidative Hydrolysis of TiCl3. *J. Electroanal. Chem.* **1993**, *346*, 291–307.

Kavan, L.; Steier, L.; Gratzel, M. Ultrathin Buffer Layers of SnO2 by Atomic Layer Deposition: Perfect Blocking Function and Thermal Stability. *J. Phys. Chem. C* **2017**, *121* (1), 342–350.

Kavan, L.; Zukalova, M.; Vik, O.; Havlicek, D. Sol-Gel Titanium Dioxide Blocking Layers for Dye-Sensitized Solar Cells: Electrochemical Characterization. *ChemPhysChem* **2014**, *15* (6), 1056–1061.

Khan, S. U. M. Stability and Photoresponse of Nanocrystalline N-TiO2 and n-TiO2/Mn2O3 Thin Film Electrodes during Water Splitting Reactions. *J. Electrochem. Soc.* **1998**, *145* (1), 89.

Khelladi, M. R.; Mentar, L.; Beniaiche, A.; Makhloufi, L.; Azizi, A. A Study on Electrodeposited Zinc Oxide Nanostructures. *J. Mater. Sci. Mater. Electron.* **2013**, *24* (1), 153–159.

Kim, H. S.; Kang, S. H. Effect of Hydrogen Treatment on Anatase TiO2 Nanotube Arrays for Photoelectrochemical Water Splitting. Bull. *Korean Chem. Soc.* **2013**, *34* (7), 2067–2072.

Kim, H. S.; Nguyen, D. T.; Shin, E. C.; Lee, J. S.; Lee, S. K.; Ahn, K. S.; Kang, S. H. Bifunctional Doping Effect on the TiO2 Nanowires for Photoelectrochemical Water Splitting. *Electrochim. Acta* **2013**, *114*, 159–164.

Kim, J. K.; Bae, S.; Kim, W.; Jeong, M. J.; Lee, S. H.; Lee, C. L.; Choi, W. K.; Hwang, J. Y.; Park, J. H.; Son, D. I. Nano Carbon Conformal Coating Strategy for Enhanced Photoelectrochemical Responses and Long-Term Stability of ZnO Quantum Dots. *Nano Energy* **2015**, *13*, 258–266.

Kim, M. H.; Kwon, Y. U. Semiconducting Divalent Metal Oxides as Blocking Layer Material for SnO2-Based Dye-Sensitized Solar Cells. *J. Phys. Chem. C* **2011**, *115* (46), 23120–23125.

King, L. A.; Yang, Q.; Grossett, M. L.; Galazka, Z.; Uecker, R.; Parkinson, B. A. Photosensitization of Natural and Synthetic SnO2 Single Crystals with Dyes and Quantum Dots. *J. Phys. Chem. C* **2016**, *120* (29), 15735–15742.

Kinoshita, K.; Madou, M. J. Electrochemical Measurements on Pt, Ir, and Ti Oxides as PH Probes. *J. Electrochem. Soc.* **1984**, *131* (5), 1089–1094.

Kobayashi, K.; Aikawa, Y.; Sukigara, M. Surface States at Semiconductor-Liquid Junction. *J. Appl. Phys.* **1983**, *54* (5), 2526–2532.

Kobayashi, K.; Aikawa, Y.; Sukigara, M. Surface States of N-Type TiO2 Electrode in Aqueous Solution. *Chem. Lett.* **1981**, *10* (5), 679–680.

Kobayashi, K.; Aikawa, Y.; Sukigara, M. Tunnel Electrode I. Electron Transfer Process at Highly Doped SnO2 Electrode with Ce4+ in High Overvoltage Region. *Bull. Chem. Soc. Jpn.* **1982**, *55* (9), 2820–2826.

Kohl, P. A.; Bard, A. J. Semiconductor Electrodes. 13. Characterization and Behavior of n-Type ZnO, CdS, and GaP Electrodes in Acetonitrile Solutions. *J. Am. Chem. Soc.* **1977**, *99* (23), 7531–7539.

Kong, D.-S.; Lu, W.-H.; Feng, Y.-Y.; Yu, Z.-Y.; Wu, J.-X.; Fan, W.-J.; Liu, H.-Y. Studying on the Point-Defect-Conductive Property of the Semiconducting Anodic Oxide Films on Titanium. *J. Electrochem. Soc.* **2009**, *156* (1), C39–C44.

Kötz, R.; Stucki, S.; Carcer, B. Electrochemical Waste Water Treatment Using High Overvoltage Anodes. Part I: Physical and Electrochemical Properties of SnO2 Anodes. *J. Appl. Electrochem.* **1991**, *21* (1), 14–20.

Krbal, M.; Sopha, H.; Pohl, D.; Benes, L.; Damm, C.; Rellinghaus, B.; Kupčík, J.; Bezdička, P.; Šubrt, J.; Macak, J. M. Self-Organized TiO2 Nanotubes Grown on Ti Substrates with Different Crystallographic Preferential Orientations: Local Structure of TiO2 Nanotubes vs. Photo-Electrochemical Response. *Electrochim. Acta* **2018**, *264*, 393–399.

Krysova, H.; Zlamalova, M.; Tarabkova, H.; Jirkovsky, J.; Frank, O.; Kohout, M.; Kavan, L. Rutile TiO2 Thin Film Electrodes with Excellent Blocking Function and Optical Transparency. *Electrochim. Acta* **2019**, *321*, 134685.

Kumar, B. N. ZnO and ZnO / PbS Heterojunction Photo Electrochemical Cells. *Int. J. Res. Eng. Technol.* **2015**, *4* (7), 464–467.

Kwon, S. W.; Ma, M.; Jeong, M. J.; Zhang, K.; Kim, S. J.; Park, J. H. Solution Processable Formation of a Few Nanometer Thick-Disordered Overlayer on the Surface of Open-Ended TiO2 Nanotubes. *Chem. Commun.* **2016**, *52* (95), 13807–13810.

Lahmar, H.; Azizi, A.; Schmerber, G.; Dinia, A. Effect of the Thickness of the ZnO Buffer Layer on the Properties of Electrodeposited P-Cu2O/n-ZnO/n-AZO Heterojunctions. *RSC Adv.* **2016**, *6* (73), 68663–68674.

Lahmar, H.; Rekhila, G.; Trari, M.; Bessekhouad, Y. HCrO4- Reduction on the Novel Heterosystem La2CuO4/SnO2 Under Solar Light. *Environ. Prog. Sustain. Energy* **2015**, *34* (3), 744–750.

Lahmar, H.; Setifi, F.; Azizi, A.; Schmerber, G.; Dinia, A. On the Electrochemical Synthesis and Characterization of P-Cu2O/n-ZnO Heterojunction. *J. Alloys Compd.* **2017**, *718*, 36–45.

Lamouchi, A.; Slimi, B.; Ben Assaker, I.; Gannouni, M.; Chtourou, R. Correlation between SSM Substrate Effect and Physical Properties of ZnO Nanowires Electrodeposited with or without Seed Layer for Enhanced Photoelectrochemical Applications. *Eur. Phys. J. Plus* **2016**, *131* (6), 201.

Lantz, J. M.; Baba, R.; Corn, R. M. Optical Second Harmonic Generation as a Probe of Electrostatic Fields and Flatband Potential at Single-Crystal TiO2 Electrodes. *J. Phys. Chem.* **1993**, *97* (29), 7392–7395.

Lee, T. H.; Ryu, H.; Lee, W. J. Photoelectrochemical Properties of Iron (III)-Doped TiO2 Nanorods. *Ceram. Int.* **2015**, *41* (6), 7582–7589.

Li, D.; Jiang, Z.; Xia, Q.; Zhang, Z.; Yao, Z. Efficient Homogeneous and Isomorphic Blocking Layer – Skeleton Rutile TiO2 Electron Transfer Structure for Quantum Dot Sensitized Solar Cells. *Results Phys.* **2018**, *11*, 1015–1021.

Li, H.; Cheng, C.; Li, X.; Liu, J.; Guan, C.; Tay, Y. Y.; Fan, H. J. Composition-Graded ZnxCd1-XSe@ZnO Core-Shell Nanowire Array Electrodes for Photoelectrochemical Hydrogen Generation. *J. Phys. Chem. C* **2012**, *116* (5), 3802–3807.

Li, J.; Cui, H.; Song, X.; Wei, N.; Tian, J. The High Surface Energy of NiO {110} Facets Incorporated into TiO 2 Hollow Microspheres by Etching Ti Plate for Enhanced Photocatalytic and Photoelectrochemical Activity. *Appl. Surf. Sci.* **2017**, *396*, 1539–1545.

Li, L.; Yan, J.; Wang, T.; Zhao, Z. J.; Zhang, J.; Gong, J.; Guan, N. Sub-10 Nm Rutile Titanium Dioxide Nanoparticles for Efficient Visible-Light-Driven Photocatalytic Hydrogen Production. *Nat. Commun.* **2015**, *6*, 5881.

Li, W.; Hua, F.; Yue, J.; Li, J. Ag@AgCl Plasmon-Induced Sensitized ZnO Particle for High-Efficiency Photocatalytic Property under Visible Light. *Appl. Surf. Sci.* **2013**, *285*, 490–497.

Li, X.; Wang, D. T.; Chen, J. F.; Tao, X. (I2)n-Encapsulated and C-Encapsulated TiO2 Films: Enhanced Photoelectrochemical and Visible-Light Photoelectrocatalytic Properties. *Electrochim. Acta* **2012**, *80*, 126–132.

Li, X.; Yu, Q.; Yu, C.; Huang, Y.; Li, R.; Wang, J.; Guo, F.; Zhang, Y.; Gao, S.; Zhao, L. Zinc-Doped SnO2 Nanocrystals as Photoanode Materials for Highly Efficient Dye-Sensitized Solar Cells. *J. Mater. Chem. A* **2015**, *3* (15), 8076–8082.

Li, Y.; Cao, C.; Xie, X.; Zhang, L.; Lin, S. Enhanced Photoelectrochemical Performance of TiO2 Nanotube Arrays with Coexisted Pt Nanoparticles and Co-Pi Cocatalysts. *Appl. Surf. Sci.* **2018**, *436*, 337–344.

Li, Y.; Guo, Y.; Li, Y.; Zhou, X. Fabrication of Cd-Doped TiO2 Nanorod Arrays and Photovoltaic Property in Perovskite Solar Cell. *Electrochim. Acta* **2016**, *200* (3), 29–36.

Li, Y.; Tian, X.; Wang, Y.; Yang, Q.; Diao, Y.; Zhang, B.; Yang, D. In Situ Construction of a MgSn(OH)6 Perovskite/SnO2 Type-II Heterojunction: A Highly Efficient Photocatalyst towards Photodegradation of Tetracycline. *Nanomaterials* **2020**, *10* (1), 53.

Li, Z.; Jia, M.; Abraham, B.; Blake, J. C.; Bodine, D.; Newberg, J. T.; Gundlach, L. Synthesis and Characterization of ZnO/CuO Vertically Aligned Hierarchical Tree-like Nanostructure. *Langmuir* **2018**, *34* (3), 961–969.

Li, Z.; Zhou, Y.; Yu, T.; Liu, J.; Zou, Z. Unique Zn-Doped SnO2 Nano-Echinus with Excellent Electron Transport and Light Harvesting Properties as Photoanode Materials for High Performance Dye-Sensitized Solar Cell. *CrystEngComm* **2012**, *14* (20), 6462–6468.

Liang, D.; Huang, Y.; Wu, F.; Luo, J.; Yi, X.; Wang, J.; Qiu, X. In Situ Synthesis of G-C3N4/TiO2 with {001} and {101} Facets Coexposed for Water Remediation. *Appl. Surf. Sci.* **2019**, *487*, 322–334.

Liang, J.; Tan, H.; Liu, M.; Liu, B.; Wang, N.; Zhang, Q.; Zhao, Y.; Smets, A. H. M.; Zeman, M.; Zhang, X. A Thin-Film Silicon Based Photocathode with a Hydrogen Doped TiO2 Protection Layer for Solar Hydrogen Evolution. *J. Mater. Chem. A* **2016**, *4* (43), 16841–16848.

Liang, Y.; Novet, T.; Thorne, J. E.; Parkinson, B. A. Photosensitization of ZnO Single Crystal Electrodes with PbS Quantum Dots. *Phys. Status Solidi Appl. Mater. Sci.* **2014**, *211* (9), 1954–1959.

Lichterman, M. F.; Hu, S.; Richter, M. H.; Crumlin, E. J.; Axnanda, S.; Favaro, M.; Drisdell, W.; Hussain, Z.; Mayer, T.; Brunschwig, B. S.; Lewis, N. S.; Liu, Z.; Lewerenz, H.-J. Direct Observation of the Energetics at a Semiconductor / Liquid Junction by Operando X-Ray Photoelectron Spectroscopy. *Energy Environ. Sci.* **2015**, *No. 8*, 2409–2416.

Lin, B.; Xu, B.; Zhou, Y.; Zhu, B.; Chen, Y.; Gao, B. Heterostructured SnO2-Pillared Co-Doped Tantalotungstate with High Photocatalytic Activity under Visible-Light Irradiation. *Mater. Chem. Phys.* **2013**, *142*, 651–658.

Lin, H.; Rumaiz, A. K.; Schulz, M.; Wang, D.; Rock, R.; Huang, C. P.; Shah, S. I. Photocatalytic Activity of Pulsed Laser Deposited TiO2 Thin Films. *Mater. Sci. Eng. B Solid-State Mater. Adv. Technol.* **2008**, *151* (2), 133–139.

Lin, Y.; Kapadia, R.; Yang, J.; Zheng, M.; Chen, K.; Hettick, M.; Yin, X.; Battaglia, C.; Sharp, I. D.; Ager, J. W.; Javey, A. Role of TiO2 Surface Passivation on Improving the Performance of P-InP Photocathodes. *J. Phys. Chem. C* **2015**, *119* (5), 2308–2313.

Lisowska-Oleksiak, A.; Szybowska, K.; Jasulaitiené, V. Preparation and Characterisation of Visible Light Responsive Iodine Doped TiO2 Electrodes. *Electrochim. Acta* **2010**, *55* (20), 5881–5885.

Liu, E.; Xue, P.; Jia, J.; Zhang, X.; Ji, Z.; Fan, J.; Hu, X. CdSe Modified TiO2 Nanotube Arrays with Ag Nanoparticles as Electron Transfer Channel and Plasmonic Photosensitizer for Enhanced Photoelectrochemical Water Splitting. *J. Phys. D. Appl. Phys.* **2018**, *51* (30), 305106.

Liu, G.; Li, Z.; Shi, J.; Sun, K.; Ji, Y.; Wang, Z.; Qiu, Y.; Liu, Y.; Wang, Z.; Hu, P. A. Black Reduced Porous SnO2 Nanosheets for CO2 Electroreduction with High Formate Selectivity and Low Overpotential. *Appl. Catal. B Environ.* **2020**, *260*, 118134.

Liu, H.; Ma, X.; Chen, Z.; Li, Q.; Lin, Z.; Liu, H.; Zhao, L.; Chu, S. Controllable Synthesis of [11−2−2] Faceted InN Nanopyramids on ZnO for Photoelectrochemical Water Splitting. *Small* **2018**, *14* (17), 1703623.

Liu, J.; Duan, Y.; Zhou, X.; Lin, Y. Influence of VB Group Doped TiO 2 on Photovoltaic Performance of Dye-Sensitized Solar Cells. *Appl. Surf. Sci.* **2013**, *277*, 231–236.

Liu, J.; Yang, H.; Tan, W.; Zhou, X.; Lin, Y. Photovoltaic Performance Improvement of Dye-Sensitized Solar Cells Based on Tantalum-Doped TiO2 Thin Films. *Electrochim. Acta* **2010**, *56* (1), 396–400.

Liu, L. X.; Fu, J.; Jiang, L. P.; Zhang, J. R.; Zhu, W.; Lin, Y. Highly Efficient Photoelectrochemical Reduction of CO2 at Low Applied Voltage Using 3D Co-Pi/BiVO4/SnO2 Nanosheet Array Photoanodes. *ACS Appl. Mater. Interfaces* **2019**, *11* (29), 26024–26031.

Liu, L.; Shu, S.; Zhang, G.; Liu, S. Highly Selective Sensing of C2H6O, HCHO, and C3H6O Gases by Controlling SnO2 Nanoparticle Vacancies. *ACS Appl. Nano Mater.* **2018**, *1* (1), 31–37.

Liu, Q. P. Analysis on Dye-Sensitized Solar Cells Based on Fe-Doped TiO2 by Intensity-Modulated Photocurrent Spectroscopy and Mott-Schottky. *Chinese Chem. Lett.* **2014**, *25* (6), 953–956.

Liu, Q. Photovoltaic Performance Improvement of Dye-Sensitized Solar Cells Based on Mg-Doped TiO2 Thin Films. *Electrochim. Acta* **2014**, *129*, 459–462.

Liu, Q.; Zhou, Y.; Duan, Y.; Lin, Y. Zinc-Doping in TiO2 Films to Enhance Photovoltaic Performance of Dye-Sensitized Solar Cells. *Appl. Mech. Mater.* **2011**, *66–68*, 224–228.

Liu, Q.; Zhou, Y.; Duan, Y.; Wang, M.; Lin, Y. Improved Photovoltaic Performance of Dye-Sensitized Solar Cells (DSSCs) by Zn + Mg Co-Doped TiO2 Electrode. *Electrochim. Acta* **2013**, *95* (3), 48–53.

Long, X.; Li, F.; Gao, L.; Hu, Y.; Hu, H.; Jin, J.; Ma, J. Heterojunction and Oxygen Vacancy Modification of ZnO Nanorod Array Photoanode for Enhanced Photoelectrochemical Water Splitting. *ChemSusChem* **2018**, *11* (23), 4094–4101.

Lu, W.; Jin, Y.; Wang, G.; Chen, D.; Li, J. Enhanced Photoelectrochemical Method for Linear DNA Hybridization Detection Using Au-Nanopaticle Labeled DNA as Probe onto Titanium Dioxide Electrode. *Biosens. Bioelectron.* **2008**, *23* (10), 1534–1539.

Lu, Y.; Choi, D.; Nelson, J.; Yang, O.-B.; Parkinson, B. A. Adsorption, Desorption, and Sensitization of Low-Index Anatase and Rutile Surfaces by the Ruthenium Complex Dye N3. *J. Electrochem. Soc.* **2006**, *153* (8), E131–E137.

Lv, Y.; Cai, B.; Ma, Q.; Wang, Z.; Liu, J.; Zhang, W. H. Highly Crystalline Nb-Doped TiO2 Nanospindles as Superior Electron Transporting Materials for High-Performance Planar Structured Perovskite Solar Cells. *RSC Adv.* **2018**, *8* (37), 20982–20989.

Lv, Y.; Li, Y.; Sun, H.; Guo, Y.; Li, Y.; Tan, J.; Zhou, X. Yttrium-Doped TiO2 Nanorod Arrays and Application in Perovskite Solar Cells for Enhanced Photocurrent Density. *Thin Solid Films* **2018**, *651*, 117–123.

Lynch, R. P.; Ghicov, A.; Schmuki, P. A Photo-Electrochemical Investigation of Self-Organized TiO2 Nanotubes. *J. Electrochem. Soc.* **2010**, *157* (3), G76–G84.

Ma, B.; Yang, J.; Han, H.; Wang, J.; Zhang, X.; Li, C. Enhancement of Photocatalytic Water Oxidation Activity on IrOx-ZnO/Zn2-XGeE4-x-3yN2y Catalyst with the Solid Solution Phase Junction. *J. Phys. Chem. C* **2010**, *114* (29), 12818–12822.

Ma, J.; Tan, X.; Jiang, F.; Yu, T. Graphitic C3N4 Nanosheet-Sensitized Brookite TiO2 to Achieve Photocatalytic Hydrogen Evolution under Visible Light. *Catal. Sci. Technol.* **2017**, *7* (15), 3275–3282.

Macyk, W.; Burgeth, G.; Kisch, H. Photoelectrochemical Properties of Platinum(IV) Chloride Surface Modified TiO2. *Photochem. Photobiol. Sci.* **2003**, *2* (3), 322–328.

Magnan, H.; Stanescu, D.; Rioult, M.; Fonda, E.; Barbier, A. Epitaxial TiO2 Thin Film Photoanodes: Influence of Crystallographic Structure and Substrate Nature. *J. Phys. Chem. C* **2019**, *123* (9), 5240–5248.

Majumder, T.; Hmar, J. J. L.; Debnath, K.; Gogurla, N.; Roy, J. N.; Ray, S. K.; Mondal, S. P. Photoelectrochemical and Photosensing Behaviors of Hydrothermally Grown ZnO Nanorods. *J. Appl. Phys.* **2014**, *116* (3), 034311.

Makarova, M. V.; MacOunová, K.; Krtil, P. The Effect of Cationic Disorder on the Optical and Electrochemical Behavior of Nanocrystalline ZnO Preparedfrom Peroxide Precursors. *J. Solid State Electrochem.* **2006**, *10* (5), 320–328.

Malik, H.; Barrera, K.; Mohanty, S.; Carlson, K. Enhancing Electrochemical Properties of TiO2 Nanotubes via Engineered Defect Laden Crystal Structures. *Mater. Lett.* **2020**, *273*, 127956.

Malizia, M.; Seger, B.; Chorkendorff, I.; Vesborg, P. C. K. Formation of a P-n Heterojunction on GaP Photocathodes for H2 Production Providing an Open-Circuit Voltage of 710 MV. *J. Mater. Chem. A* **2014**, *2* (19), 6847–6853.

Mancilla, F. J.; Rojas, S. F.; Gualdrón-Reyes, A. F.; Carreño-Lizcano, M. I.; Duarte, L. J.; Niño-Gómez, M. E. Improving the Photoelectrocatalytic Performance of Boron-Modified TiO2/Ti Sol-Gel-Based Electrodes for Glycerol Oxidation under Visible Illumination. *RSC Adv.* **2016**, *6* (52), 46668–46677.

Mandal, H.; Shyamal, S.; Hajra, P.; Samanta, B.; Fageria, P.; Pande, S.; Bhattacharya, C. Improved Photoelectrochemical Water Oxidation Using Wurtzite ZnO Semiconductors Synthesized through Simple Chemical Bath Reaction. *Electrochim. Acta* **2014**, *141*, 294–301.

Marlinda, A. R.; Yusoff, N.; Pandikumar, A.; Huang, N. M.; Akbarzadeh, O.; Sagadevan, S.; Wahab, Y. A.; Johan, M. R. Tailoring Morphological Characteristics of Zinc Oxide Using a One-Step Hydrothermal Method for Photoelectrochemical Water Splitting Application. *Int. J. Hydrogen Energy* **2019**, *44* (33), 17535–17543.

Martínez-Vargas, B. L.; Cruz-Ramírez, M.; Díaz-Real, J. A.; Rodríguez-López, J. L.; Bacame-Valenzuela, F. J.; Ortega-Borges, R.; Reyes-Vidal, Y.; Ortiz-Frade, L. Synthesis and Characterization of N-ZnO/p-MnO Nanocomposites for the Photocatalytic Degradation of Anthracene. *J. Photochem. Photobiol. A Chem.* **2019**, *369*, 85–96.

Matsumura, M.; Nomura, Y.; Tsubomura, H. Effect of Etching on Intrinsic and Dye-Sensitized Photocurrents in Zinc Oxide Electrodes. *Bull. Chem. Soc. Jpn.* **1979**, *52* (6), 1559–1562.

Mavroides, J. G.; Tchernev, D. I.; Kafalas, J. A.; Kolesar, D. F. Photoelectrolysis of Water in Cells with TiO2 Anodes. *Mater. Res. Bull.* **1975**, *10* (10), 1023–1030.

McCann, J. F.; Pezy, J. The Measurement of the Flatband Potentials of N-Type and p-Type Semiconductors by Rectified Alternating Photocurrent Voltammetry. *J. Electrochem. Soc.* **1981**, *128* (8), 1735–1740.

McDonnell, K. A.; English, N. J.; Stallard, C. P.; Rahman, M.; Dowling, D. P. Fabrication of Nano-Structured TiO2 Coatings Using a Microblast Deposition Technique. *Appl. Surf. Sci.* **2013**, *275*, 316–323.

Memming, R.; Möllers, F. Studies of the Rearrangement-Energy in Electrode Kinetics at SnO2-Electrodes. *Berichte der Bunsengesellschaft/Physical Chem. Chem. Phys.* **1972**, *76* (6), 475–481.

Mentar, L.; Baka, O.; Khelladi, M. R.; Azizi, A.; Velumani, S.; Schmerber, G.; Dinia, A. Effect of Nitrate Concentration on the Electrochemical Growth and Properties of ZnO Nanostructures. *J. Mater. Sci. Mater. Electron.* **2015**, *26* (2), 1217–1224.

Mentar, L.; Lahmar, H.; Khelladi, M. R.; Azizi, A. The Effect of Bath Temperature on the Electrodeposition of Zinc Oxide Nanostructures via Nitrates Solution. *Semicond. Sci. Technol.* **2014**, *4* (1), 41–45.

Metikoš-Huković, M.; Omanović, S.; Jukić, A. Impedance Spectroscopy of Semiconducting Films on Tin Electrodes. *Electrochim. Acta* **1999**, *45* (6), 977–986.

Metikos-Hukovic, M.; Seruga, M.; Ferina, S. In Situ Investigation of Duplex Semiconducting Films on Tin. *Berichte der Bunsengesellschaft/Physical Chem. Chem. Phys.* **1992**, *96* (6), 799–805.

Mieritz, D. G.; Renaud, A.; Seo, D. K. Unusual Changes in Electronic Band-Edge Energies of the Nanostructured Transparent n-Type Semiconductor Zr-Doped Anatase TiO2 (Ti1-XZrxO2; X < 0.3). *Inorg. Chem.* **2016**, *55* (13), 6574–6585.

Miki, T.; Yanagi, H. Scanning Probe Microscopic Characterization of Surface-Modified n-TiO2 Single-Crystal Electrodes. *Langmuir* **1998**, *14* (12), 3405–3410.

Mikula, M.; Blecha, J.; Ceppan, M. Photoelectrochemical Properties of Anodic TiO2 Layers Prepared by Various Current Densities. *J. Electrochem. Soc.* **1992**, *139* (12), 3470–3474.

Miyake, M.; Yoneyama, H.; Tamura, H. Two Step Oxidation Reactions of Alcohols on an Illuminated Rutile Electrode. *Chem. Lett.* **1976**, *5* (6), 635–640.

Moina, C. A.; Varela, F. E.; Hernández, L. F.; Ybarra, G. O.; Vilche, J. R. Semiconductor Properties of Passive Oxide Layers on Binary Tin + Indium Alloys. *J. Electroanal. Chem.* **1997**, *427*, 189–197.

Möllers, F.; Memming, R. Electrochemical Studies of Semiconducting SnO2-Electrodes. *Berichte der Bunsengesellschaft/Physical Chem. Chem. Phys.* **1972**, *76* (6), 469–475.

Möllers, F.; Tolle, H. J.; Memming, R. On the Origin of the Photocatalytic Deposition of Noble Metals on TiO2. *J. Electrochem. Soc.* **1974**, *121* (9), 1160–1167.

Momeni, M. M.; Ghayeb, Y.; Ezati, F. Fabrication, Characterization and Photoelectrochemical Activity of Tungsten-Copper Co-Sensitized TiO 2 Nanotube Composite Photoanodes. *J. Colloid Interface Sci.* **2018**, *514*, 70–82.

Moniz, S. J. A.; Tang, J. Charge Transfer and Photocatalytic Activity in CuO/TiO2 Nanoparticle Heterojunctions Synthesised through a Rapid, One-Pot, Microwave Solvothermal Route. *ChemCatChem* **2015**, *7* (11), 1659–1667.

Moniz, S. J. A.; Zhu, J.; Tang, J. 1D Co-Pi Modified BiVO4/ZnO Junction Cascade for Efficient Photoelectrochemical Water Cleavage. *Adv. Energy Mater.* **2014**, *4* (10), 1301590.

Munirathinam, B.; Neelakantan, L. Role of Crystallinity on the Nanomechanical and Electrochemical Properties of TiO2 Nanotubes. *J. Electroanal. Chem.* **2016**, *770*, 73–83.

Munirathinam, B.; Neelakantan, L. Titania Nanotubes from Weak Organic Acid Electrolyte: Fabrication, Characterization and Oxide Film Properties. *Mater. Sci. Eng. C* **2015**, *49*, 567–578.

Muñoz, A. G. Semiconducting Properties of Self-Organized TiO2 Nanotubes. *Electrochim. Acta* **2007**, *52* (12), 4167–4176.

Muñoz, A. G.; Chen, Q.; Schmuki, P. Interfacial Properties of Self-Organized TiO 2 Nanotubes Studied by Impedance Spectroscopy. *J. Solid State Electrochem.* **2007**, *11* (8), 1077–1084.

Murashkina, A. A.; Rudakova, A. V.; Ryabchuk, V. K.; Nikitin, K. V.; Mikhailov, R. V.; Emeline, A. V.; Bahnemann, D. W. Influence of the Dopant Concentration on the Photoelectrochemical Behavior of Al-Doped TiO2. *J. Phys. Chem. C* **2018**, *122* (14), 7975–7981.

Naatz, H.; Hoffmann, R.; Hartwig, A.; La Mantia, F.; Pokhrel, S.; Mädler, L. Determination of the Flat Band Potential of Nanoparticles in Porous Electrodes by Blocking the Substrate-Electrolyte Contact. *J. Phys. Chem. C* **2018**, *122* (5), 2796–2805.

Nakamura, R.; Ohashi, N.; Imanishi, A.; Osawa, T.; Matsumoto, Y.; Koinuma, H.; Nakato, Y. Crystal-Face Dependences of Surface Band Edges and Hole Reactivity, Revealed by Preparation of Essentially Atomically Smooth and Stable (110) and (100) n-TiO2 (Rutile) Surfaces. *J. Phys. Chem. B* **2005**, *109* (5), 1648–1651.

Naldoni, A.; Montini, T.; Malara, F.; Mróz, M. M.; Beltram, A.; Virgili, T.; Boldrini, C. L.; Marelli, M.; Romero-Ocaña, I.; Delgado, J. J.; Dal Santo, V.; Fornasiero, P. Hot Electron Collection on Brookite Nanorods Lateral Facets for Plasmon-Enhanced Water Oxidation. *ACS Catal.* **2017**, *7* (2), 1270–1278.

Naphade, R. A.; Tathavadekar, M.; Jog, J. P.; Agarkar, S.; Ogale, S. Plasmonic Light Harvesting of Dye Sensitized Solar Cells by Au-Nanoparticle Loaded TiO2 Nanofibers. *J. Mater. Chem. A* **2014**, *2* (4), 975–984.

Nebel, R.; Macounová, K. M.; Tarábková, H.; Kavan, L.; Krtil, P. Selectivity of Photoelectrochemical Water Splitting on TiO2 Anatase Single Crystals. *J. Phys. Chem. C* **2019**, *123* (17), 10857–10867.

Ning, X.; Huang, J.; Li, L.; Gu, Y.; Jia, S.; Qiu, R.; Li, S.; Kim, B. H. Homostructured Rutile TiO2 Nanotree Arrays Thin Film Electrodes with Nitrogen Doping for Enhanced Photoelectrochemical Performance. *J. Mater. Sci. Mater. Electron.* **2019**, *30* (17), 16030–16040.

Ning, X.; Huang, J.; Li, S.; Li, L.; Gu, Y.; Li, X.; Kim, B. H. Influence of Nanobranched Growth on Photoelectrochemical Performance of TiO 2 Nanotree Arrays Films. *Mater. Sci. Semicond. Process.* **2019**, *94*, 156–163.

Niu, X.; Yan, W.; Shao, C.; Zhao, H.; Yang, J. Hydrothermal Synthesis of Mo-C Co-Doped TiO2 and Coupled with Fluorine-Doped Tin Oxide (FTO) for High-Efficiency Photodegradation of Methylene Blue and Tetracycline: Effect of Donor-Acceptor Passivated Co-Doping. *Appl. Surf. Sci.* **2019**, *466*, 882–892.

Nobuyoshi, K.; Hirotoshi, Y. Effects of Ion Implantation on the Photoelectrochemical Properties of TiO2. *Nucl. Inst. Methods Phys. Res. B* **1991**, *59–60* (2), 1236–1239.

Nosaka, Y.; Sasaki, H.; Norimatsu, K.; Miyama, H. Effect of Surface Compound Formation on the Photo-Induced Reaction at Polycrystalline TiO2 Semicunductor Electrodes. *Chem. Phys. Lett.* **1984**, *105* (4), 456–458.

Oekermann, T.; Karuppuchamy, S.; Yoshida, T.; Schlettwein, D.; Wöhrle, D.; Minoura, H. Electrochemical Self-Assembly of ZnO/SO3EtPTCDI Hybrid Photoelectrodes. *J. Electrochem. Soc.* **2004**, *151* (1), C62–C68.

Pan, Q.; Li, A.; Zhang, Y.; Yang, Y.; Cheng, C. Rational Design of 3D Hierarchical Ternary SnO2/TiO2/BiVO4 Arrays Photoanode toward Efficient Photoelectrochemical Performance. *Adv. Sci.* **2020**, *7* (3), 1902235.

Paracchino, A.; Mathews, N.; Hisatomi, T.; Stefik, M.; Tilley, S. D.; Grätzel, M. Ultrathin Films on Copper(i) Oxide Water Splitting Photocathodes: A Study on Performance and Stability. *Energy Environ. Sci.* **2012**, *5*, 8673–8681.

Parthasarathy, M.; Ramgir, N. S.; Sathe, B. R.; Mulla, I. S.; Pillai, V. K. Surface-State-Mediated Electron Transfer at Nanostructured ZnO Multipod/Electrolyte Interfaces. *J. Phys. Chem. C* **2007**, *111* (35), 13092–13102.

Patil, S. S.; Tarwal, N. L.; Yadav, H. M.; Korade, S. D.; Bhat, T. S.; Teli, A. M.; Karanjkar, M. M.; Kim, J. H.; Patil, P. S. Photoelectrochemical Performance of Dye and Semiconductor Sensitization on 1-D Hollow Hexagonal ZnO Rods: A Comparative Study. *J. Solid State Electrochem.* **2018**, *22* (10), 3015–3024.

Pawar, R. C.; Shaikh, J. S.; Babar, A. A.; Dhere, P. M.; Patil, P. S. Aqueous Chemical Growth of ZnO Disks, Rods, Spindles and Flowers: PH Dependency and Photoelectrochemical Properties. *Sol. Energy* **2011**, *85* (5), 1119–1127.

Peighambardoust, N. S.; Khameneh Asl, S.; Mohammadpour, R.; Asl, S. K. Band-Gap Narrowing and Electrochemical Properties in N-Doped and Reduced Anodic TiO2 Nanotube Arrays. *Electrochim. Acta* **2018**, *270*, 245–255.

Pelouchova, H.; Janda, P.; Weber, J.; Kavan, L. Charge Transfer Reductive Doping of Single Crystal TiO2 Anatase. *J. Electroanal. Chem.* **2004**, *566* (1), 73–83.

Peng, T.; Wen, Y.; Wang, C.; Wang, Y.; Zhang, G.; Zhang, Y.; Dionysiou, D. D. Preparation of SnO2/Conjugated Polyvinyl Alcohol Derivative Nanohybrid with Good Performance in Visible Light-Induced Photocatalytic Reduction of Cr(VI). *Mater. Sci. Semicond. Process.* **2019**, *102*, 104586.

Petit, J. P.; Alonso Vante, N.; Chartier, P. Light Modulation Induced Electrical Resonance (LMIER) Application to the Determination of the Flatband Potential. *J. Electroanal. Chem.* **1983**, *157* (1), 145–149.

Piña-Pérez, Y.; Aguilar-Martínez, O.; Acevedo-Peña, P.; Santolalla-Vargas, C. E.; Oros-Ruíz, S.; Galindo-Hernández, F.; Gómez, R.; Tzompantzi, F. Novel ZnS-ZnO Composite Synthesized by the Solvothermal Method through the Partial Sulfidation of ZnO for H2 Production without Sacrificial Agent. *Appl. Catal. B Environ.* **2018**, *230*, 125–134.

Poznyak, S. K.; Sviridov, V. V.; Kulak, A. I.; Samtsov, M. P. Photoluminescence and Electroluminescence at the TiO2-Electrolyte Interface. *J. Electroanal. Chem.* **1992**, *340*, 73–97.

Pradhan, D.; Mohapatra, S. K.; Tymen, S.; Misra, M.; Leung, K. T. Morphology-Controlled ZnO Nanomaterials for Enhanced Photoelectrochemical Performance. *Mater. Express* **2011**, *1* (1), 59–67.

Prasad, M.; Sharma, V.; Aher, R.; Rokade, A.; Ilaiyaraja, P.; Sudakar, C.; Jadkar, S. Synergistic Effect of Ag Plasmon-and Reduced Graphene Oxide-Embedded ZnO Nanorod-Based Photoanodes for Enhanced Photoelectrochemical Activity. *J. Mater. Sci.* **2017**, *52* (23), 13572–13585.

Prasad, M.; Sharma, V.; Rokade, A.; Ilaiyaraja, P.; Chandran, S.; Jadkar, S. Enhanced Photosplitting of Water Using Ultrathin Cobalt Sulfide Nanoflakes-Sensitized Zinc Oxide Nanorods Array. *Ionics (Kiel).* **2017**, *23* (12), 3401–3408.

Preethi, L. K.; Mathews, T. Electrochemical Tuning of Heterojunctions in TiO2 Nanotubes for Efficient Solar Water Splitting. *Catal. Sci. Technol.* **2019**, *9* (19), 5425–5432.

Pruethiarenun, K.; Isobe, T.; Matsushita, S.; Ye, J.; Nakajima, A. Comparative Study of Photoinduced Wettability Conversion between [PW12O40]3-/Brookite and [SiW12O40]4-/Brookite Hybrid Films. *Mater. Chem. Phys.* **2014**, *144* (3), 327–334.

Pu, P.; Cachet, H.; Ngaboyamahina, E.; Sutter, E. M. M. Relation between Morphology and Conductivity in TiO2 Nanotube Arrays: An Electrochemical Impedance Spectrometric Investigation. *J. Solid State Electrochem.* **2013**, *17* (3), 817–828.

Qamar, M. T.; Aslam, M.; Rehan, Z. A.; Soomro, M. T.; Ahmad, I.; Ishaq, M.; Ismail, I. M. I.; Fornasiero, P.; Hameed, A. MoO3 Altered ZnO: A Suitable Choice for the Photocatalytic Removal of Chloro-Acetic Acids in Natural Sunlight Exposure. *Chem. Eng. J.* **2017**, *330*, 322–336.

Qamar, M. T.; Aslam, M.; Rehan, Z. A.; Soomro, M. T.; Basahi, J. M.; Ismail, I. M. I.; Almeelbi, T.; Hameed, A. The Influence of P-Type Mn3O4 Nanostructures on the Photocatalytic Activity of ZnO for the Removal of Bromo and Chlorophenol in Natural Sunlight Exposure. *Appl. Catal. B Environ.* **2017**, *201*, 105–118.

Qiu, Q.; Li, S.; Jiang, J.; Wang, D.; Lin, Y.; Xie, T. Improved Electron Transfer between TiO2 and FTO Interface by N-Doped Anatase TiO2 Nanowires and Its Applications in Quantum Dot-Sensitized Solar Cells. *J. Phys. Chem. C* **2017**, *121* (39), 21560–21570.

Radecka, M. TiO2 for Photoelectrolytic Decomposition of Water. *Thin Solid Films* **2004**, *451–452*, 98–104.

Radecka, M.; Brudnik, A.; Kulinowski, K.; Kot, A.; Leszczyński, J.; Kanak, J.; Zakrzewska, K. Titanium Dioxide Thin Films with Controlled Stoichiometry for Photoelectrochemical Systems. *J. Electron. Mater.* **2019**, *48* (9), 5481–5490.

Radecka, M.; Rekas, M.; Trenczek-Zajac, A.; Zakrzewska, K. Importance of the Band Gap Energy and Flat Band Potential for Application of Modified TiO2 Photoanodes in Water Photolysis. *J. Power Sources* **2008**, *181* (1), 46–55.

Radecka, M.; Wierzbicka, M.; Rekas, M. Photoelectrochemical Cell Studied by Impedance Spectroscopy. *Phys. B Condens. Matter* **2004**, *351* (1–2), 121–128.

Radecka, M.; Wnuk, A.; Trenczek-Zajac, A.; Schneider, K.; Zakrzewska, K. TiO2/SnO2 Nanotubes for Hydrogen Generation by Photoelectrochemical Water Splitting. *Int. J. Hydrogen Energy* **2015**, *40* (1), 841–851.

Radecka, M.; Zakrzewska, K.; Wierzbicka, M.; Gorzkowska, A.; Komornicki, S. Study of the TiO2-Cr2O3 System for Photoelectrolytic Decomposition of Water. *Solid State Ionics* **2003**, *157* (1–4), 379–386.

Ramasamy, E.; Lee, J. Ordered Mesoporous Zn-Doped SnO2 Synthesized by Exotemplating for Efficient Dye-Sensitized Solar Cells. *Energy Environ. Sci.* **2011**, *4* (7), 2529–2536.

Rambabu, Y.; Jaiswal, M.; Roy, S. C. Enhanced Photo-Electrochemical Performance of Reduced Graphene-Oxide Wrapped TiO2 Multi-Leg Nanotubes. *J. Electrochem. Soc.* **2016**, *163* (8), H652–H656.

Rambabu, Y.; Jaiswal, M.; Roy, S. C. Probing the Charge Recombination in RGO Decorated Mixed Phase (Anatase-Rutile) TiO2 Multi-Leg Nanotubes. *AIP Adv.* **2016**, *6* (11), 115010.

Ramírez-Ortega, D.; Acevedo-Peña, P.; Tzompantzi, F.; Arroyo, R.; González, F.; González, I. Energetic States in SnO2–TiO2 Structures and Their Impact on Interfacial Charge Transfer Process. *J. Mater. Sci.* **2017**, *52*, 260–275.

Ramírez-Ortega, D.; Meléndez, A. M.; Acevedo-Peña, P.; González, I.; Arroyo, R. Semiconducting Properties of ZnO/TiO2 Composites by Electrochemical Measurements and Their Relationship with Photocatalytic Activity. *Electrochim. Acta* **2014**, *140*, 541–549.

Rasouli, F.; Rouhollahi, A.; Ghahramanifard, F. Fabrication of Silver Nanoparticles Decorated Zinc Oxide Nanotubes by Electrodeposition Technique for Photoelectrochemical Water Splitting. *Mater. Sci. Semicond. Process.* **2019**, *93*, 371–378.

Rasouli, F.; Rouhollahi, A.; Ghahramanifard, F. Gradient Doping of Copper in ZnO Nanorod Photoanode by Electrodeposition for Enhanced Charge Separation in Photoelectrochemical Water Splitting. *Superlattices Microstruct.* **2019**, *125*, 177–189.

Raval, D.; Jani, M.; Chaliyawala, H.; Joshi, A.; Mukhopadhyay, I.; Ray, A. Solar to Chemical Energy Conversion Using Titania Nanorod Photoanodes Augmented by Size Distribution of Plasmonic Au-Nanoparticle. *Mater. Chem. Phys.* **2019**, *231*, 322–334.

Rayhana, B.; Mustapha, B.; Redha, K. M.; Halla, L.; Amor, A. A Study on Electrodeposited of ZnO/ZnS Heterostructures. *J. Dispers. Sci. Technol.* **2019**, *40* (5), 668–678.

Redmond, G.; O'Keeffe, A.; Burgess, C.; MacHale, C.; Fitzmaurice, D. Spectroscopic Determination of the Flatband Potential of Transparent Nanocrystalline ZnO Films. *J. Phys. Chem.* **1993**, *97* (42), 11081–11086.

Reichman, B. Photovoltage Response to Temperature Change at Oxide Semiconductor Electrodes. *J. Electrochem. Soc.* **1981**, *128* (12), 2601–2603.

Ren, X.; Sangle, A.; Zhang, S.; Yuan, S.; Zhao, Y.; Shi, L.; Hoye, R. L. Z.; Cho, S.; Li, D.; Macmanus-Driscoll, J. L. Photoelectrochemical Water Splitting Strongly Enhanced in Fast-Grown ZnO Nanotree and Nanocluster Structures. *J. Mater. Chem. A* **2016**, *4* (26), 10203–10211.

Resasco, J.; Zhang, H.; Kornienko, N.; Becknell, N.; Lee, H.; Guo, J.; Briseno, A. L.; Yang, P. TiO2/BiVO4 Nanowire Heterostructure Photoanodes Based on Type II Band Alignment. *ACS Cent. Sci.* **2016**, *2* (2), 80–88.

Rokade, A.; Rondiya, S.; Date, A.; Sharma, V.; Prasad, M.; Pathan, H.; Jadkar, S. Electrochemical Synthesis of Core-Shell ZnO/CdS Nanostructure for Photocatalytic Water Splitting Application. *Energy Procedia* **2017**, *110*, 121–127.

Rokade, A.; Rondiya, S.; Sharma, V.; Prasad, M.; Pathan, H.; Jadkar, S. Electrochemical Synthesis of 1D ZnO Nanoarchitectures and Their Role in Efficient Photoelectrochemical Splitting of Water. *J. Solid State Electrochem.* **2017**, *21* (9), 2639–2648.

Roose, B.; Johansen, C. M.; Dupraz, K.; Jaouen, T.; Aebi, P.; Steiner, U.; Abate, A. A Ga-Doped SnO2 Mesoporous Contact for UV Stable Highly Efficient Perovskite Solar Cells. *J. Mater. Chem. A* **2018**, *6* (4), 1850–1857.

Sadhu, S.; Poddar, P. Growth of Oriented Single Crystalline La-Doped TiO2 Nanorod Arrays Electrode and Investigation of Optoelectronic Properties for Enhanced Photoelectrochemical Activity. *RSC Adv.* **2013**, *3* (26), 10363–10369.

Sadhu, S.; Poddar, P. Template-Free Fabrication of Highly-Oriented Single-Crystalline 1D-Rutile TiO2-MWCNT Composite for Enhanced Photoelectrochemical Activity. *J. Phys. Chem. C* **2014**, *118* (33), 19363–19373.

Sakai, N.; Fujishima, A.; Watanabe, T.; Hashimoto, K. Enhancement of the Photoinduced Hydrophilic Conversion Rate of TiO2 Film Electrode Surfaces by Anodic Polarization. *J. Phys. Chem. B* **2001**, *105* (15), 3023–3026.

Salah, N.; Hameed, A.; Aslam, M.; Babkair, S. S.; Bahabri, F. S. Photocatalytic Activity of V Doped ZnO Nanoparticles Thin Films for the Removal of 2-Chlorophenol from the Aquatic Environment under Natural Sunlight Exposure. *J. Environ. Manage.* **2016**, *177*, 53–64.

Salvador, P. Hole Diffusion Length in N-TiO2 Single Crystals and Sintered Electrodes: Photoelectrochemical Determination and Comparative Analysis. *J. Appl. Phys.* **1984**, *55* (8), 2977–2985.

Salvador, P. Influence of pH on the Potential Dependence of the Efficiency of Water Photo-Oxidation at n-TiO2 Electrodes. *J. Electrochem. Soc.* **1981**, *128* (9), 1895-1900.

Salvador, P. Kinetic Approach to the Photocurrent Transients in Water Photoelectrolysis at N-TiO2 Electrodes. 1. Analysis of the Ratio of the Instantaneous to Steady-State Photocurrent. *J. Phys. Chem.* **1985**, *89* (18), 3863–3869.

Salvador, P.; González, M. L. G.; Muñoz, F. Catalytic Role of Lattice Defects in the Photoassisted Oxidation of Water at (001) n-TiO2 Rutile. *J. Phys. Chem.* **1992**, *96* (25), 10349–10353.

Sambur, J. B.; Chen, P. Distinguishing Direct and Indirect Photoelectrocatalytic Oxidation Mechanisms Using Quantitative Single-Molecule Reaction Imaging and Photocurrent Measurements. *J. Phys. Chem. C* **2016**, *120* (37), 20668–20675.

Sambur, J. B.; Chen, T. Y.; Choudhary, E.; Chen, G.; Nissen, E. J.; Thomas, E. M.; Zou, N.; Chen, P. Sub-Particle Reaction and Photocurrent Mapping to Optimize Catalyst-Modified Photoanodes. *Nature* **2016**, *530* (7588), 77–80.

Samir, M.; Salama, M.; Allam, N. K. Sub-100 Nm TiO2 Tubular Architectures for Efficient Solar Energy Conversion. *J. Mater. Chem. A* **2016**, *4* (24), 9375–9380.

Sang, L.; Tan, H.; Zhang, X.; Wu, Y.; Ma, C.; Burda, C. Effect of Quantum Dot Deposition on the Interfacial Flatband Potential, Depletion Layer in TiO 2 Nanotube Electrodes, and Resulting H 2 Generation Rates. *J. Phys. Chem. C* **2012**, *116* (35), 18633–18640.

Sangiorgi, A.; Bendoni, R.; Sangiorgi, N.; Sanson, A.; Ballarin, B. Optimized TiO2 Blocking Layer for Dye-Sensitized Solar Cells. *Ceram. Int.* **2014**, *40* (7), 10727–10735.

Savva, A.; Smith, K.; Lawson, M.; Croft, S.; Weltner, A.; Jones, C.; Bull, H.; Simmonds, P.; Li, L.; Xiong, H. Defect Generation in TiO2 Nanotube Anodes via Heat Treatment in Various Atmospheres for Lithium-Ion Batteries. *Phys. Chem. Chem. Phys.* **2018**, *20* (35), 22537–225546.

Schoenmakers, G. H.; Vanmaekelbergh, D.; Kelly, J. J. Study of Charge Carrier Dynamics at Illuminated ZnO Photoanodes. *J. Phys. Chem.* **1996**, *100* (8), 3215–3220.

Schultze, J. W.; Elfenthal, L.; Leitner, K. Modification of Oxide Films by Ion Implantation: TiO2-Films Modified by Ti+ and O+ as Example. *Electrochim. Acta* **1988**, *33* (7), 911–925.

Schultze, J. W.; Stimming, U.; Weise, J. Capacity and Photocurrent Measurements at Passive Titanium Electrodes. *Berichte der Bunsengesellschaft/Physical Chem. Chem. Phys.* **1982**, *86* (4), 276–282.

Selloum, D.; Henni, A.; Karar, A.; Tabchouche, A.; Harfouche, N.; Bacha, O.; Tingry, S.; Rosei, F. Effects of Fe Concentration on Properties of ZnO Nanostructures and Their Application to Photocurrent Generation. *Solid State Sci.* **2019**, *92*, 76–80.

Septina, W.; Prabhakar, R. R.; Wick, R.; Moehl, T.; Tilley, S. D. Stabilized Solar Hydrogen Production with CuO/CdS Heterojunction Thin Film Photocathodes. *Chem. Mater.* **2017**, *29* (4), 1735–1743.

Šeruga, M.; Metikoš-Huković, M. Passivation of Tin in Citrate Buffer Solutions. *J. Electroanal. Chem.* **1992**, *334*, 223–240.

Shaikh, S. F.; Mane, R. S.; Hwang, Y. J.; Joo, O. S. Calcium Carbonate Electronic-Insulating Layers Improve the Charge Collection Efficiency of Tin Oxide Photoelectrodes in Dye-Sensitized Solar Cells. *Electrochim. Acta* **2015**, *167*, 379–387.

Shaikh, S. F.; Mane, R. S.; Joo, O. S. La2O3-Encapsulated SnO2 Nanocrystallite-Based Photoanodes for Enhanced DSSCs Performance. *Dalt. Trans.* **2015**, *44* (7), 3075–3081.

Shaikh, S. F.; Mane, R. S.; Joo, O. S. Mass Scale Sugar-Mediated Green Synthesis and DSSCs Application of Tin Oxide Nanostructured Photoanode: Effect of Zinc Sulphide Layering on Charge Collection Efficiency. *Electrochim. Acta* **2014**, *147*, 408–417.

Shaikh, S. F.; Mane, R. S.; Joo, O. S. Spraying Distance and Titanium Chloride Surface Treatment Effects on DSSC Performance of Electrosprayed SnO2 Photoanodes. *RSC Adv.* **2014**, *4* (68), 35919–35927.

Shang, Q.; Huang, X.; Tan, X.; Yu, T. High Activity Ti3+-Modified Brookite TiO2/Graphene Nanocomposites with Specific Facets Exposed for Water Splitting. *Ind. Eng. Chem. Res.* **2017**, *56* (32), 9098–9106.

Sharma, S.; Singh, S.; Khare, N. Enhanced Photosensitization of Zinc Oxide Nanorods Using Polyaniline for Efficient Photocatalytic and Photoelectrochemical Water Splitting. *Int. J. Hydrogen Energy* **2016**, *41* (46), 21088–21098.

Shaw, K.; Christensen, P.; Hamnett, A. Photoelectrochemical Oxidation of Organics on Single-Crystal TiO2: An in Situ FTIR Study. *Electrochim. Acta* **1996**, *41* (5), 719–728.

Shi, Q.; Li, Z.; Chen, L.; Zhang, X.; Han, W.; Xie, M.; Yang, J.; Jing, L. Synthesis of SPR Au/BiVO4 Quantum Dot/Rutile-TiO2 Nanorod Array Composites as Efficient Visible-Light Photocatalysts to Convert CO2 and Mechanism Insight. *Appl. Catal. B Environ.* **2019**, *244*, 641–649.

Shukla, P. K.; Karn, R. K.; Singh, A. K.; Srivastava, O. N. Studies on PV Assisted PEC Solar Cells for Hydrogen Production through Photoelectrolysis of Water. *Int. J. Hydrogen Energy* **2002**, *27* (2), 135–141.

Siavash Moakhar, R.; Jalali, M.; Kushwaha, A.; Kia Liang Goh, G.; Riahi-Noori, N.; Dolati, A.; Ghorbani, M. AuPd Bimetallic Nanoparticle Decorated TiO2 Rutile Nanorod Arrays for Enhanced Photoelectrochemical Water Splitting. *J. Appl. Electrochem.* **2018**, *48* (9), 995–1007.

Sieber, B.; Liu, H.; Piret, G.; Laureyns, J.; Roussel, P.; Gelloz, B.; Szunerits, S.; Boukherroub, R. Synthesis and Luminescence Properties of (N-Doped) ZnO Nanostructures from a Dimethylformamide Aqueous Solution. *J. Phys. Chem. C* **2009**, *113* (31), 13643–13650.

Silva, D. D.; Sánchez-Montes, I.; Hammer, P.; Aquino, J. M. On the Supercapacitor Performance of Microwave Heat Treated Self Organized TiO2 Nanotubes: Influence of the Cathodic Pre-Treatment, Water Aging, and Thermal Oxide. *Electrochim. Acta* **2017**, *245*, 165–172.

Silva, I. M. P.; Byzynski, G.; Ribeiro, C.; Longo, E. Different Dye Degradation Mechanisms for ZnO and ZnO Doped with N (ZnO:N). *J. Mol. Catal. A Chem.* **2016**, *417*, 89–100.

Sima, M.; Vasile, E.; Sima, A. Investigation of the Photoelectrochemical Behavior of Nanocarbon/Mesoporous TiO2 Films. *Dig. J. Nanomater. Biostructures* **2019**, *14* (4), 935–941.

Singh, A. P.; Kodan, N.; Mehta, B. R. Enhancing the Photoelectrochemical Properties of Titanium Dioxide by Thermal Treatment in Oxygen Deficient Environment. *Appl. Surf. Sci.* **2016**, *372*, 63–69.

Singh, A. P.; Kumari, S.; Shrivastav, R.; Dass, S.; Satsangi, V. R. Iron Doped Nanostructured TiO2 for Photoelectrochemical Generation of Hydrogen. *Int. J. Hydrogen Energy* **2008**, *33* (20), 5363–5368.

Singh, A. P.; Kumari, S.; Tripathi, A.; Singh, F.; Gaskell, K. J.; Shrivastav, R.; Dass, S.; Ehrman, S. H.; Satsangi, V. R. Improved Photoelectrochemical Response of Titanium Dioxide Irradiated with 120 MeV Ag9+ Ions. *J. Phys. Chem. C* **2010**, *114*, 622–626.

Siripala, W.; Tomkiewicz, M. Surface Recombination at N-TiO2 Electrodes in Photoelectrolytic Solar Cells. *J. Electrochem. Soc.* **1983**, *130* (5), 1062–1067.

Sitler, S. J.; Raja, K. S.; Karmiol, Z.; Chidambaram, D. Photoelectrochemical Characterization of Dual-Layered Anodic TiO2 Nanotubes with Honeycomb Morphology. *J. Phys. D. Appl. Phys.* **2017**, *50* (3), 035502.

Siuzdak, K.; Szkoda, M.; Sawczak, M.; Lisowska-Oleksiak, A.; Karczewski, J.; Ryl, J. Enhanced Photoelectrochemical and Photocatalytic Performance of Iodine-Doped Titania Nanotube Arrays. *RSC Adv.* **2015**, *5*, 50379–50391.

Song, J.; Zheng, M.; Yuan, X.; Li, Q.; Wang, F.; Ma, L.; You, Y.; Liu, S.; Liu, P.; Jiang, D.; Ma, L.; Shen, W. Electrochemically Induced Ti3+ Self-Doping of TiO2 Nanotube Arrays for Improved Photoelectrochemical Water Splitting. *J. Mater. Sci.* **2017**, *52* (12), 6976–6986.

Song, R.; Zhou, W.; Luo, B.; Jing, D. Highly Efficient Photocatalytic H2 Evolution Using TiO2 Nanoparticles Integrated with Electrocatalytic Metal Phosphides as Cocatalysts. *Appl. Surf. Sci.* **2017**, *416*, 957–964.

Song, X. M.; Yuan, C.; Wang, Y.; Wang, B.; Mao, H.; Wu, S.; Zhang, Y. ZnO/CuO Photoelectrode with n-p Heterogeneous Structure for Photoelectrocatalytic Oxidation of Formaldehyde. *Appl. Surf. Sci.* **2018**, *455*, 181–186.

Song, Y.; Roy, P.; Paramasivam, I.; Schmuki, P. Voltage-Induced Payload Release and Wettability Control on TiO2 and TiO2 Nanotubes. *Angew. Chemie* **2010**, *122* (2), 361–364.

Sopha, H.; Krbal, M.; Ng, S.; Prikryl, J.; Zazpe, R.; Yam, F. K.; Macak, J. M. Highly Efficient Photoelectrochemical and Photocatalytic Anodic TiO2 Nanotube Layers with Additional TiO2 Coating. *Appl. Mater. Today* **2017**, *9*, 104–110.

Sopha, H.; Mirza, I.; Turčičova, H.; Pavlinak, D.; Michalicka, J.; Krbal, M.; Rodriguez-Pereira, J.; Hromadko, L.; Novák, O.; Mužík, J.; Smrž, M.; Kolibalova, E.; Goodfriend, N.; Bulgakova, N. M.; Mocek, T.; Macak, J. M. Laser-Induced Crystallization of Anodic TiO2nanotube Layers. *RSC Adv.* **2020**, *10* (37), 22137–22145.

Spadavecchia, F.; Cappelletti, G.; Ardizzone, S.; Ceotto, M.; Falciola, L. Electronic Structure of Pure and N-Doped TiO2 Nanocrystals by Electrochemical Experiments and First Principles Calculations. *J. Phys. Chem. C* **2011**, *115* (14), 6381–6391.

Spagnol, V.; Sutter, E.; Debiemme-Chouvy, C.; Cachet, H.; Baroux, B. EIS Study of Photo-Induced Modifications of Nano-Columnar TiO2 Films. *Electrochim. Acta* **2009**, *54* (4), 1228–1232.

Steinmiller, E. M. P.; Choi, K. S. Photochemical Deposition of Cobalt-Based Oxygen Evolving Catalyst on a Semiconductor Photoanode for Solar Oxygen Production. *Proc. Natl. Acad. Sci. U. S. A.* **2009**, *106* (49), 20633–20636.

Su, T.; Yang, Y.; Shi, Y.; Zhang, X.; Jiang, Y.; Fan, R.; Cao, W. 40% Enhanced Photocurrent of Dye Sensitized Solar Cells Using Lotus-Shaped H2-Treated Anatase TiO2 with {0 0 1} Dominated Facets. *Chem. Eng. J.* **2017**, *316*, 534–543.

Subbarao, S. N.; Yun, Y. H.; Kershaw, R.; Dwight, K.; Wold, A. Comparison of the Photoelectric Properties of the System TiO2-x with the System TiO2-XFx. *Mater. Res. Bull.* **1978**, *13*, 1461–1467.

Sui, M. rong; Han, C. ping; Gu, X. quan; Wang, Y.; Tang, L.; Tang, H. Photoelectrochemical Characteristics of TiO2 Nanorod Arrays Grown on Fluorine Doped Tin Oxide Substrates by the Facile Seeding Layer Assisted Hydrothermal Method. *Optoelectron. Lett.* **2016**, *12* (3), 161–165.

Sun, H.; Yang, Z.; Pu, Y.; Dou, W.; Wang, C.; Wang, W.; Hao, X.; Chen, S.; Shao, Q.; Dong, M.; Wu, S.; Ding, T.; Guo, Z. Zinc Oxide/Vanadium Pentoxide Heterostructures with Enhanced Day-Night Antibacterial Activities. *J. Colloid Interface Sci.* **2019**, *547*, 40–49.

Sun, M.; Chen, G.; Zhang, Y.; Wei, Q.; Ma, Z.; Du, B. Efficient Degradation of Azo Dyes over Sb2S3/TiO2 Heterojunction under Visible Light Irradiation. *Ind. Eng. Chem. Res.* **2012**, *51* (7), 2897–2903.

Sun, M.; Zhao, Q.; Du, C.; Liu, Z. Enhanced Visible Light Photocatalytic Activity in BiOCl/SnO2: Heterojunction of Two Wide Band-Gap Semiconductors. *RSC Adv.* **2015**, *5* (29), 22740–22752.

Sun, Y.; Gu, X.; Zhao, Y.; Wang, L.; Qiang, Y. Temperature-Dependent Photoluminescence Analysis of ZnO Nanowire Array Annealed in Air. *Superlattices Microstruct.* **2018**, *117*, 520–526.

Suryavanshi, R. D.; Mohite, S. V.; Bagade, A. A.; Shaikh, S. K.; Thorat, J. B.; Rajpure, K. Y. Nanocrystalline Immobilised ZnO Photocatalyst for Degradation of Benzoic Acid and Methyl Blue Dye. *Mater. Res. Bull.* **2018**, *101*, 324–333.

Syrek, K.; Sennik-Kubiec, A.; Rodríguez-López, J.; Rutkowska, M.; Żmudzki, P.; Hnida-Gut, K. E.; Grudzień, J.; Chmielarz, L.; Sulka, G. D. Reactive and Morphological Trends on Porous Anodic TiO2 Substrates Obtained at Different Annealing Temperatures. *Int. J. Hydrogen Energy* **2020**, *45* (7), 4376–4389.

Tada, H.; Hattori, A.; Tokihisa, Y.; Imai, K.; Tohge, N.; Ito, S. A Patterned-TiO2/SnO2 Bilayer Type Photocatalyst. *J. Phys. Chem. B* **2000**, *104* (19), 4586–4587.

Takata, S.; Hachiya, A.; Matsumoto, Y. Non-Linear Electric Field Response of Permittivity of Atomically Smooth TiO2(Rutile) Single Crystals Studied by an Electrochemical Approach. *J. Ceram. Soc. Japan* **2012**, *120* (9), 366–369.

Talapin, D. V.; Sviridov, D. V.; Kulak, A. I. Harmonic Analysis of the Electrical Response of an N-TiO2/Electrolyte Circuit to Periodic Laser Pulses. *J. Electroanal. Chem.* **2000**, *489* (1), 28–37.

Tanaka, S. I.; Fukushima, Y.; Nakamura, I.; Tanaki, T.; Jerkiewicz, G. Preparation and Characterization of Microporous Layers on Titanium by Anodization in Sulfuric Acid with and without Hydrogen Charging. *ACS Appl. Mater. Interfaces* **2013**, *5* (8), 3340–3347.

Tang, Y.; Traveerungroj, P.; Tan, H. L.; Wang, P.; Amal, R.; Ng, Y. H. Scaffolding an Ultrathin CdS Layer on ZnO Nanorods Array Using Pulsed Electrodeposition for Improved Photocharge Transport under Visible Light Illumination. *J. Mater. Chem. A* **2015**, *3* (38), 19582–19587.

Tay, Q.; Liu, X.; Tang, Y.; Jiang, Z.; Sum, T. C.; Chen, Z. Enhanced Photocatalytic Hydrogen Production with Synergistic Two-Phase Anatase/Brookite TiO2 Nanostructures. *J. Phys. Chem. C* **2013**, *117* (29), 14973–14982.

Teh, J. J.; Ting, S. L.; Leong, K. C.; Li, J.; Chen, P. Gallium-Doped Tin Oxide Nano-Cuboids for Improved Dye Sensitized Solar Cell. *ACS Appl. Mater. Interfaces* **2013**, *5* (21), 11377–11382.

Tezcan, F.; Mahmood, A.; Kardaş, G. Optimizing Copper Oxide Layer on Zinc Oxide via Two-Step Electrodeposition for Better Photocatalytic Performance in Photoelectrochemical Cells. *Appl. Surf. Sci.* **2019**, *479*, 1110–1117.

Tilley, S. D.; Schreier, M.; Azevedo, J.; Stefik, M.; Graetzel, M. Ruthenium Oxide Hydrogen Evolution Catalysis on Composite Cuprous Oxide Water-Splitting Photocathodes. *Adv. Funct. Mater.* **2014**, *24* (3), 303–311.

Toe, C. Y.; Tan, H. L.; Boyer, C.; Rawal, A.; Thickett, S. C.; Scott, J.; Amal, R.; Ng, Y. H. Photo-Driven Synthesis of Polymer-Coated Platinized ZnO Nanoparticles with Enhanced Photoelectrochemical Charge Transportation. *J. Mater. Chem. A* **2017**, *5* (9), 4568–4575.

Tomkiewicz, M. Relaxation Spectrum Analysis of Semiconductor-Electrolyte Interface-TiO2. *J. Electrochem. Soc.* **1979**, *126* (12), 2220–2225.

Tomkiewicz, M. The Potential Distribution at the TiO2 Aqueous Electrolyte Interface. *J. Electrochem. Soc.* **1979**, *126* (9), 1505–1510.

Tsuji, E.; Fukui, K. I.; Imanishi, A. Influence of Surface Roughening of Rutile Single-Crystalline TiO 2 on Photocatalytic Activity for Oxygen Photoevolution from Water in Acidic and Alkaline Solutions. *J. Phys. Chem. C* **2014**, *118* (10), 5406–5413.

Türkyılmaz, Ş. Ş.; Güy, N.; Özacar, M. Photocatalytic Efficiencies of Ni, Mn, Fe and Ag Doped ZnO Nanostructures Synthesized by Hydrothermal Method: The Synergistic/Antagonistic Effect between ZnO and Metals. *J. Photochem. Photobiol. A Chem.* **2017**, *341*, 39–50.

Uchiyama, H.; Nagao, R.; Kozuka, H. Photoelectrochemical Properties of ZnO–SnO2 Films Prepared by Sol–Gel Method. *J. Alloys Compd.* **2013**, *554*, 122–126.

Uosaki, K.; Yoneda, R.; Kita, H. Effect of Platinization on the Electrochemical Behavior of the TiO2 Electrode in Aqueous Solutions. *J. Phys. Chem.* **1985**, *89* (19), 4042–4046.

Vakulenko, A. M.; Kogan, Y. L. Effectiveness and Stability of Polycrystalline Electrodes Based on Titanium Dioxide in the Reaction of Photoelectrochemical Oxidation of Water. *Sol. Energy Mater.* **1980**, *3*, 357–366.

van de Krol, R.; Goossens, A. Structure and Properties of Anatase TiO2 Thin Films Made by Reactive Electron Beam Evaporation. *J. Vac. Sci. Technol. A Vacuum, Surfaces, Film.* **2003**, *21* (1), 76–83.

van de Krol, R.; Goossens, A.; Schoonman, J. Mott-Schottky Analysis of Nanometer-Scale Thin-Film Anatase TiO2. *J. Electrochem. Soc.* **1997**, *144*, 1723–1727.

Van De Krol, R.; Goossens, A.; Schoonman, J. Spatial Extent of Lithium Intercalation in Anatase TiO2. *J. Phys. Chem. B* **1999**, *103* (34), 7151–7159.

Vanalakar, S. A.; Mali, S. S.; Pawar, R. C.; Dalavi, D. S.; Mohalkar, A. V.; Deshamukh, H. P.; Patil, P. S. Farming of ZnO Nanorod-Arrays via Aqueous Chemical Route for Photoelectrochemical Solar Cell Application. *Ceram. Int.* **2012**, *38* (8), 6461–6467.

Vilche, J. R.; Jüttner, K.; Lorenz, W. J.; Kautek, W.; Paatsch, W.; Dean, M. H.; Stimming, U. Semiconductor Properties of Passive Films on Zn, ZnCo, and ZnNi Substrates. *J. Electrochem. Soc.* **1989**, *136* (12), 3773–3779.

Wahl, A.; Ulmann, M.; Carroy, A.; Jermann, B.; Dolata, M.; Kedzierzawski, P.; Chatelain, C.; Monnier, A.; Augustynski, J. Photoelectrochemical Studies Pertaining to the Activity of TiO2 towards Photodegradation of Organic Compounds. *J. Electroanal. Chem.* **1995**, *396*, 41–51.

Wan, G.; Li, P.; Xiang, X.; Zhou, J.; Huang, N. Responsive Surface Charge Transfer Doping Effect of Reductive Bio-Molecules (Glucose, Fucoidan, and Heparin) Contacting on Semiconducting Titanium Oxide Films. *J. Mater. Sci.* **2013**, *48* (11), 4109–4116.

Wang, C. T.; Ro, S. H.; Jao, C. S.; Tsai, M. K.; Yang, S. Y. ZnO Xerogel Powders for Photovoltaic Applications. *J. Non. Cryst. Solids* **2010**, *356* (18–19), 873–878.

Wang, C.; Zhang, X.; Wei, Y.; Kong, L.; Chang, F.; Zheng, H.; Wu, L.; Zhi, J.; Liu, Y. Correlation between Band Alignment and Enhanced Photocatalysis: A Case Study with Anatase/TiO2(B) Nanotube Heterojunction. *Dalt. Trans.* **2015**, *44* (29), 13331–13339.

Wang, D.; Zhang, X.; Sun, P.; Lu, S.; Wang, L.; Wang, C.; Liu, Y. Photoelectrochemical Water Splitting with Rutile TiO2 Nanowires Array: Synergistic Effect of Hydrogen Treatment and Surface Modification with Anatase Nanoparticles. *Electrochim. Acta* **2014**, *130*, 290–295.

Wang, F.; Kubala, N. G.; Wolden, C. A. Photoelectrochemical Performance of Anatase TiO2 Thin Films Deposited by Self-Limiting Growth Techniques. *J. Electrochem. Soc.* **2010**, *157* (7), D432–D436.

Wang, G.; Wang, Q.; Lu, W.; Li, J. Photoelectrochemical Study on Charge Transfer Properties of TiO 2-B Nanowires with an Application as Humidity Sensors. *J. Phys. Chem. B* **2006**, *110* (43), 22029–22034.

Wang, H. B.; Ma, F.; Sun, Y. S.; Zhou, L.; Zeng, D. J.; Qin, Y.; Xu, Y. K.; Chen, Y. N.; Xu, K. W.; Ma, D. Y. Band Bending and Valence Band Shifting of Sub-Monolayer TiO2 Functionalized SnO2 Nanowires. *J. Mater. Sci. Mater. Electron.* **2020**, *31*, 637–643.

Wang, H. Y.; Chen, J.; Hy, S.; Yu, L.; Xu, Z.; Liu, B. High-Surface-Area Mesoporous TiO2 Microspheres via One-Step Nanoparticle Self-Assembly for Enhanced Lithium-Ion Storage. *Nanoscale* **2014**, *6* (24), 14926–14931.

Wang, J.; Su, F. Y.; Zhang, W. De. Preparation and Enhanced Visible Light Photoelectrochemical Activity of G-C3N4/ZnO Nanotube Arrays. *J. Solid State Electrochem.* **2014**, *18* (10), 2921–2929.

Wang, J.; Zhang, W.-D. Modification of TiO2 Nanorod Arrays by Graphite-like C3N4 with High Visible Light Photoelectrochemical Activity. *Electrochim. Acta* **2012**, *71*, 10–16.

Wang, L.; Gu, X.; Zhao, Y.; Qiang, Y. Enhanced Photoelectrochemical Properties of ZnO Nanowire Arrays Annealed in Air. *J. Mater. Sci. Mater. Electron.* **2018**, *29* (5), 4058–4064.

Wang, L.; Wang, Y.; Schmuki, P.; Kment, S.; Zboril, R. Nanostar Morphology of Plasmonic Particles Strongly Enhances Photoelectrochemical Water Splitting of TiO2 Nanorods with Superior Incident Photon-to-Current Conversion Efficiency in Visible/near-Infrared Region. *Electrochim. Acta* **2018**, *260*, 212–220.

Wang, M.; Bai, S.; Chen, A.; Duan, Y.; Liu, Q.; Li, D.; Lin, Y. Improved Photovoltaic Performance of Dye-Sensitized Solar Cells by Sb-Doped TiO 2 Photoanode. *Electrochim. Acta* **2012**, *77*, 54–59.

Wang, M.; Ren, F.; Cai, G.; Liu, Y.; Shen, S.; Guo, L. Activating ZnO Nanorod Photoanodes in Visible Light by Cu Ion Implantation. *Nano Res.* **2014**, *7* (3), 353–364.

Wang, N.; Liu, M.; Tan, H.; Liang, J.; Zhang, Q.; Wei, C.; Zhao, Y.; Sargent, E. H.; Zhang, X. Compound Homojunction:Heterojunction Reduces Bulk and Interface Recombination in ZnO Photoanodes for Water Splitting. *Small* **2017**, *13* (10), 1603527.

Wang, R.; Shen, J.; Sun, K.; Tang, H.; Liu, Q. Enhancement in Photocatalytic Activity of CO2 Reduction to CH4 by 0D/2D Au/TiO2 Plasmon Heterojunction. *Appl. Surf. Sci.* **2019**, *493*, 1142–1149.

Wang, W.; Chen, J.; Luo, J.; Zhang, Y.; Gao, L.; Liu, Y.; Sun, J. Effects of Low Pressure Plasma Treatments on DSSCs Based on Rutile TiO 2 Array Photoanodes. *Appl. Surf. Sci.* **2015**, *324*, 143–151.

Wang, Y. L.; Guo, M.; Zhang, M.; Wang, X. D. Hydrothermal Preparation and Photoelectrochemical Performance of Size-Controlled SnO2 Nanorod Arrays. *CrystEngComm* **2010**, *12* (12), 4024–4027.

Wang, Y.; Zou, Y.; Shang, Q.; Tan, X.; Yu, T.; Huang, X.; Shi, W.; Xie, Y.; Yan, G.; Wang, X. Quasi-Spherical Brookite TiO2 Nanostructures Synthesized Using Solvothermal Method in the Presence of Oxalic Acid. *Trans. Tianjin Univ.* **2018**, *24* (4), 326–339.

Ward, M. D.; White, J. R.; Bard, A. J. Electrochemical Investigation of the Energetics of Particulate Titanium Dioxide Photocatalysts . The Methyl Viologen-Acetate System. *J. Am. Chem. Soc.* **1983**, *105*, 27–31.

Watanabe, T.; Fujishima, A.; Honda, K. Potential Variation at the Semiconductor-Electrolyte Interface Through a Change in PH of the Solution. *Chem. Lett.* **1974**, *3* (8), 897–900.

Weber, M. F. Effect of Hydrogen on the Dielectric and Photoelectrochemical Properties of Sputtered TiO2 Films. *J. Electrochem. Soc.* **1982**, *129* (9), 2022–2028.

Wilson, J. R.; Park, S.-M. Dependence of Flatband Potentials of N-TiO2 on Electrolytes and Electrolyte Concentrations. *J. Electrochem. Soc.* **1981**, *128* (11), 2369–2370.

Wilson, R. H. Observation and Analysis of Surface States on TiO2 Electrodes in Aqueous Electrolytes. *J. Electrochem. Soc.* **1980**, *127* (1), 228–234.

Wilson, R. H.; Harris, L. A.; Gerstner, M. E. Characterized Semiconductor Electrodes I. Effect of Processing Variables on the Photoelectrochemicl Properties of Single Crystal TiO2 (Rutile). *J. Electrochem. Soc.* **1979**, *126* (5), 844–850.

Wodka, D.; Socha, R. P.; Bielanska, E.; Elzbieciak-Wodka, M.; Nowak, P.; Warszynski, P. Photocatalytic Activity of Titanium Dioxide Modified by Fe2O3 Nanoparticles. *Appl. Surf. Sci.* **2014**, *319* (1), 173–180.

Wolcott, A.; Smith, W. A.; Kuykendall, T. R.; Zhao, Y.; Zhang, J. Z. Photoelectrochemical Study of Nanostructured ZnO Thin Films for Hydrogen Generation from Water Splitting. *Adv. Funct. Mater.* **2009**, *19* (12), 1849–1856.

Wu, J.; Zhu, K.; Guo, Y. F.; Xu, H.; Yan, W. Temperature Controlled Fabrication of TiO2 Nanotube-Based Arrays Electrode and Its Application for Photoelectrocatalytic Degradation of RhB. *Int. J. Electrochem. Sci.* **2020**, *15* (2), 1091–1107.

Wu, S.; Zhao, H. J.; Li, C. F.; Liu, J.; Dong, W.; Zhao, H.; Wang, C.; Liu, Y.; Hu, Z. Y.; Chen, L.; Li, Y.; Su, B. L. Type II Heterojunction in Hierarchically Porous Zinc Oxide/Graphitic Carbon Nitride Microspheres Promoting Photocatalytic Activity. *J. Colloid Interface Sci.* **2019**, *538*, 99–107.

Xiang, P.; Li, X.; Wang, H.; Liu, G.; Shu, T.; Zhou, Z.; Ku, Z.; Rong, Y.; Xu, M.; Liu, L.; Hu, M.; Yang, Y.; Chen, W.; Liu, T.; Zhang, M.; Han, H. Mesoporous Nitrogen-Doped TiO2 Sphere Applied for Quasi-Solid-State Dye-Sensitized Solar Cell. *Nanoscale Res. Lett.* **2011**, *6*, 606.

Xie, L. Q.; Ding, D.; Zhang, M.; Chen, S.; Qiu, Z.; Yan, J. W.; Yang, Z. L.; Chen, M. S.; Mao, B. W.; Tian, Z. Q. Adsorption of Dye Molecules on Single Crystalline Semiconductor Surfaces: An Electrochemical Shell-Isolated Nanoparticle Enhanced Raman Spectroscopy Study. *J. Phys. Chem. C* **2016**, *120* (39), 22500–22507.

Xie, W.; Tang, L.; Ying, M.; Liu, J.; Pan, H.; Du, M. Ag-SnO2 Nano-Heterojunction-Reduced Graphene Oxide by a Stepwise Photocatalyzed Approach and Its Application in Ractopamine Determination. *RSC Adv.* **2017**, *7* (86), 54506–54511.

Xiong, H.; Wu, L.; Liu, Y.; Gao, T.; Li, K.; Long, Y.; Zhang, R.; Zhang, L.; Qiao, Z. A.; Huo, Q.; Ge, X.; Song, S.; Zhang, H. Controllable Synthesis of Mesoporous TiO2 Polymorphs with Tunable Crystal Structure for Enhanced Photocatalytic H2 Production. *Adv. Energy Mater.* **2019**, *9* (31), 1901634.

Xu, J.; Cui, Y.; Han, Y.; Hao, M.; Zhang, X. ZnO-Graphene Composites with High Photocatalytic Activities under Visible Light. *RSC Adv*. **2016**, *6* (99), 96778–96784.

Xu, Q.; Yu, J.; Zhang, J.; Zhang, J.; Liu, G. Cubic Anatase TiO2 Nanocrystals with Enhanced Photocatalytic CO2 Reduction Activity. *Chem. Commun.* **2015**, *51* (37), 7950–7953.

Xu, T.; Zhang, L.; Cheng, H.; Zhu, Y. Significantly Enhanced Photocatalytic Performance of ZnO via Graphene Hybridization and the Mechanism Study. *Appl. Catal. B Environ.* **2011**, *101* (3–4), 382–387.

Xu, Y.; Melia, M. A.; Tsui, L. K.; Fitz-Gerald, J. M.; Zangari, G. Laser-Induced Surface Modification at Anatase TiO2 Nanotube Array Photoanodes for Photoelectrochemical Water Oxidation. *J. Phys. Chem. C* **2017**, *121* (32), 17121–17128.

Yan, J.; Zhang, Y.; Liu, S.; Wu, G.; Li, L.; Guan, N. Facile Synthesis of an Iron Doped Rutile TiO2 Photocatalyst for Enhanced Visible-Light-Driven Water Oxidation. *J. Mater. Chem. A* **2015**, *3* (43), 21434–21438.

Yan, Y.; Lee, J.; Cui, X. Enhanced Photoelectrochemical Properties of Ta-TiO2 Nanotube Arrays Prepared by Magnetron Sputtering. *Vacuum* **2017**, *138*, 30–38.

Yanagi, H.; Chen, S.; Lee, P. A.; Nebesny, K. W.; Armstrong, N. R.; Fujishima, A. Dye-Sensitizing Effect of TiOPc Thin Film on n-TiO2 (001) *Surface. J. Phys. Chem*. **1996**, *100* (13), 5447–5451.

Yang, L.; Huang, J.; Liu, H.; Li, S.; Han, Y.; Qi, G.; Lv, M.; Shang, Y.; Ye, J. SnO2−x/Sb2O3 Composites Synthesized by Mechanical Milling Method with Excellent Photocatalytic Properties for Isopropyl Alcohol Oxidation. *J. Mater. Sci. Mater. Electron.* **2020**, *31* (11), 8564–8577.

Yang, L.; Yang, Y.; Liu, T.; Ma, X.; Lee, S. W.; Wang, Y. Oxygen Vacancies Confined in SnO2 Nanoparticles for Glorious Photocatalytic Activities from the UV, Visible to near-Infrared Region. *New J. Chem.* **2018**, *42* (18), 15253–15262.

Yang, M. H.; Tsai, M. C.; Chang, Y. W.; Chang, Y. C.; Chiu, H. T.; Lee, C. Y. Photodegradation by a Heterogeneous Mixture of Micro-Sized Anatase and Truncated Rhomboid Anatase Hollow Spheres. *ChemCatChem* **2013**, *5* (7), 1871–1876.

Yang, M.; Ding, B.; Lee, J. K. Surface Electrochemical Properties of Niobium-Doped Titanium Dioxide Nanorods and Their Effect on Carrier Collection Efficiency of Dye Sensitized Solar Cells. *J. Power Sources* **2014**, *245*, 301–307.

Yang, T.; Xue, J.; Tan, H.; Xie, A.; Li, S.; Yan, W.; Shen, Y. Highly Ordered ZnO/ZnFe2O4 Inverse Opals with Binder-Free Heterojunction Interfaces for High-Performance Photoelectrochemical Water Splitting. *J. Mater. Chem. A* **2018**, *6* (3), 1210–1218.

Yang, Y.; Liu, G.; Irvine, J. T. S.; Cheng, H. M. Enhanced Photocatalytic H2 Production in Core–Shell Engineered Rutile TiO2. *Adv. Mater.* **2016**, *28*, 5850–5856.

Yang, Y.; Ye, K.; Cao, D.; Gao, P.; Qiu, M.; Liu, L.; Yang, P. Efficient Charge Separation from F- Selective Etching and Doping of Anatase-TiO2{001} for Enhanced Photocatalytic Hydrogen Production. *ACS Appl. Mater. Interfaces* **2018**, *10* (23), 19633–19638.

Yang, Z.; Wang, B.; Cui, H.; An, H.; Pan, Y.; Zhai, J. Synthesis of Crystal-Controlled TiO2 Nanorods by a Hydrothermal Method: Rutile and Brookite as Highly Active Photocatalysts. *J. Phys. Chem. C* **2015**, *119* (29), 16905–16912.

Yang, Z.; Wang, B.; Zhang, J.; Cui, H.; Pan, Y.; An, H.; Zhai, J. Factors Influencing the Photocatalytic Activity of Rutile TiO2 Nanorods with Different Aspect Ratios for Dye Degradation and Cr(VI) Photoreduction. *Phys. Chem. Chem. Phys.* **2015**, *17* (28), 18670–18676.

Yew, R.; Karuturi, S. K.; Liu, J.; Tan, H. H.; Wu, Y.; Jagadish, C. Exploiting Defects in TiO 2 Inverse Opal for Enhanced Photoelectrochemical Water Splitting. *Opt. Express* **2019**, *27* (2), 761–773.

Yilmaz, C.; Unal, U. Effect of Zn(NO3)2 Concentration in Hydrothermal-Electrochemical Deposition on Morphology and Photoelectrochemical Properties of ZnO Nanorods. *Appl. Surf. Sci.* **2016**, *368* (3), 456–463.

Yoko, T.; Hu, L.; Kozuka, H.; Sakka, S. Photoelectrochemical Properties of TiO2 Coating Films Prepared Using Different Solvents by the Sol-Gel Method. *Thin Solid Films* **1996**, *283*, 188–195.

Yoneyama, H.; Sakamoto, H.; Tamura, H. A Photo-Electochemical Cell with Production of Hydrogen and Oxygen by a Cell Reaction. *Electrochim. Acta* **1975**, *20* (5), 341–345.

Yu, L.; He, J.; Huang, C.; Li, M.; Zhang, Y.; Zhou, X.; Zhu, H. Electron Transportation Path Build for Superior Photoelectrochemical Performance of Ag3PO4/TiO2. *RSC Adv.* **2017**, *7* (86), 54485–54490.

Yu, Y. X.; Ouyang, W. X.; Zhang, W. De. Photoelectrochemical Property of the BiOBr-BiOI/ZnO Heterostructures with Tunable Bandgap. *J. Solid State Electrochem.* **2014**, *18* (6), 1743–1750.

Yun, G.; Song, G. Y.; Ahn, B. E.; Lee, S. K.; Heo, J.; Ahn, K. S.; Kang, S. H. Beneficial Surface Passivation of Hydrothermally Grown TiO 2 Nanowires for Solar Water Oxidation. *Appl. Surf. Sci.* **2016**, *366*, 561–566.

Zebbar, N.; Trari, M.; Doulache, M.; Boughelout, A.; Chabane, L. Physical and Photo-Electrochemical Characterizations of ZnO Thin Films Deposited by Ultrasonic Spray Method: Application to HCrO4- Photoreduction. *Appl. Surf. Sci.* **2014**, *292*, 837–842.

Zhang, B.; Wang, Z.; Huang, B.; Zhang, X.; Qin, X.; Li, H.; Dai, Y.; Li, Y. Anisotropic Photoelectrochemical (PEC) Performances of ZnO Single-Crystalline Photoanode: Effect of Internal Electrostatic Fields on the Separation of Photogenerated Charge Carriers during PEC Water Splitting. *Chem. Mater.* **2016**, *28* (18), 6613–6620.

Zhang, H.; Zhang, Q.; Lv, Y.; Yang, C.; Chen, H.; Zhou, X. Upconversion Er-Doped TiO2 Nanorod Arrays for Perovskite Solar Cells and the Performance Improvement. *Mater. Res. Bull.* **2018**, *106*, 346–352.

Zhang, S.; Gu, X.; Zhao, Y.; Qiang, Y. Enhanced Photoelectrochemical Performance of TiO2 Nanorod Arrays by a 500°C Annealing in Air: Insights into the Mechanism. *J. Electron. Mater.* **2016**, *45* (1), 648–653.

Zhang, W.; Guo, H.; Sun, H.; Zeng, R. C. Hydrothermal Synthesis and Photoelectrochemical Performance Enhancement of TiO 2 /Graphene Composite in Photo-Generated Cathodic Protection. *Appl. Surf. Sci.* **2016**, *382*, 128–134.

Zhang, W.; Guo, H.; Sun, H.; Zeng, R. Constructing Ternary Polyaniline-Graphene-TiO2 Hybrids with Enhanced Photoelectrochemical Performance in Photo-Generated Cathodic Protection. *Appl. Surf. Sci.* **2017**, *410*, 547–556.

Zhang, X.; Liu, F.; Huang, Q. L.; Zhou, G.; Wang, Z. S. Dye-Sensitized W-Doped TiO2 Solar Cells with a Tunable Conduction Band and Suppressed Charge Recombination. *J. Phys. Chem. C* **2011**, *115* (25), 12665–12671.

Zhang, Z.; Jiang, X.; Mei, J.; Li, Y.; Han, W.; Xie, M.; Wang, F.; Xie, E. Improved Photoelectrocatalytic Hydrogen Generation through BiVO4 Quantum-Dots Loaded on Nano-Structured SnO2 and Modified with Carbon Quantum-Dots. *Chem. Eng. J.* **2018**, *331*, 48–53.

Zhao, H.; Zalfani, M.; Li, C. F.; Liu, J.; Hu, Z. Y.; Mahdouani, M.; Bourguiga, R.; Li, Y.; Su, B. L. Cascade Electronic Band Structured Zinc Oxide/Bismuth Vanadate/Three-Dimensional Ordered Macroporous Titanium Dioxide Ternary Nanocomposites for Enhanced Visible Light Photocatalysis. *J. Colloid Interface Sci.* **2019**, *539*, 585–597.

Zhao, M.; Xu, H.; Chen, H.; Ouyang, S.; Umezawa, N.; Wang, D.; Ye, J. Photocatalytic Reactivity of {121} and {211} Facets of Brookite TiO2 Crystals. *J. Mater. Chem. A* **2015**, *3* (5), 2331–2337.

Zhao, M.; Xu, H.; Ouyang, S.; Li, D.; Meng, X.; Ye, J. Effect of Band Structure on the Hot-Electron Transfer over Au Photosensitized Brookite TiO2. *Phys. Chem. Chem. Phys.* **2016**, *18* (5), 3409–3412.

Zhao, Y. L.; Barman, A. R.; Dhar, S.; Annadi, A.; Motapothula, M.; Wang, J.; Su, H.; Breese, M.; Venkatesan, T.; Wang, Q. Scaling of Flat Band Potential and Dielectric Constant as a Function of Ta Concentration in Ta-TiO2 Epitaxial Films. *AIP Adv.* **2011**, *1* (2), 022151.

Zhao, Y.; Gu, X.; He, R.; Zhu, L.; Qiang, Y. Influence of Annealing Ambient on the Photoelectric and Photoelectrochemical Properties of TiO2 Nanorod Arrays. *J. Electron. Mater.* **2018**, *47* (9), 5251–5258.

Zhong, H.; Yang, C.; Fan, L.; Fu, Z.; Yang, X.; Wang, X.; Wang, R. Dyadic Promotion of Photocatalytic Aerobic Oxidation: Via the Mott-Schottky Effect Enabled by Nitrogen-Doped Carbon from Imidazolium-Based Ionic Polymers. *Energy Environ. Sci.* **2019**, *12* (1), 418–426.

Zhong, P.; Chen, X.; Niu, B.; Li, C.; Wang, Y.; Xi, H.; Lei, Y.; Wang, Z.; Ma, X. Niobium Doped TiO2 Nanorod Arrays as Efficient Electron Transport Materials in Photovoltaic. *J. Power Sources* **2020**, *450*, 227715.

Zhou, J.; Yin, L.; Li, H.; Liu, Z.; Wang, J.; Duan, K.; Qu, S.; Weng, J.; Feng, B. Heterojunction of SrTiO3/TiO2 Nanotubes with Dominant (001) Facets: Synthesis, Formation Mechanism and Photoelectrochemical Properties. *Mater. Sci. Semicond. Process.* **2015**, *40*, 107–116.

Zhu, H.; Yan, S.; Li, Z.; Zou, Z. Back Electron Transfer at TiO2 Nanotube Photoanodes in the Presence of a H2O2 Hole Scavenger. *ACS Appl. Mater. Interfaces* **2017**, *9* (39), 33887–33895.

Zhu, L.; Li, H.; Liu, Z.; Xia, P.; Xie, Y.; Xiong, D. Synthesis of the 0D/3D CuO/ZnO Heterojunction with Enhanced Photocatalytic Activity. *J. Phys. Chem. C* **2018**, *122* (17), 9531–9539.

Zoppi, R. A.; Trasferetti, B. C.; Davanzo, C. U. Sol-Gel Titanium Dioxide Thin Films on Platinum Substrates: Preparation and Characterization. *J. Electroanal. Chem.* **2003**, *544* (SUPPL.), 47–57.